Sensorless control of an ironless permanent magnet synchronous machine with automatic machine modelling

by

Anton Treurnicht

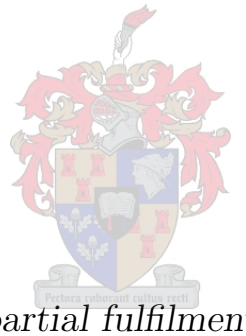

Thesis presented in partial fulfilment of the requirements for the degree of Master of Engineering (Electrical and Electronic) in the Faculty of Engineering at Stellenbosch University

Supervisor: Dr. P.J. Randewijk and Dr. J.M. Strauss

March 2017

Declaration

By submitting this thesis electronically, I declare that the entirety of the work contained therein is my own, original work, that I am the sole author thereof (save to the extent explicitly otherwise stated), that reproduction and publication thereof by Stellenbosch University will not infringe any third party rights and that I have not previously in its entirety or in part submitted it for obtaining any qualification.

Date: March 2017 .....

Abstract

Sensorless control of an ironless permanent magnet synchronous machine with automatic machine modelling

A. Treurnicht

Thesis: MEng (Elect)

March 2017

This project investigates the sensorless control of a new generation ironless non-salient pole permanent-magnet synchronous machine (IDRFPMSM) for wind-turbine generator and electric-vehicle applications. Due to the nature of the ironless non-salient pole permanent-magnet synchronous machine, BEMF sensorless rotor position estimation techniques is mandatory. BEMF position-estimation techniques cannot be used at rotor standstill and low rotational speeds. In applications where efficiency is critical at low speed, a magnetic stray-field position sensor was implemented to provide the rotor position below the minimum estimator speed, by measuring the magnetic stray-fields behind the Halbach permanent-magnet array. To provide the sensorless position estimator and the control system with accurate machine parameters, an open-loop parameter estimation technique is introduced for estimating all five machine parameters at system power-on. This is augmented during closed-loop operation by updating the parameters with an online parameter estimator. A demonstrator was built to show that the combination of all of the closed-loop elements can be integrated with the IDRFPMSM machine. The results also show that the IDRFPMSM can be used in both sensorless generator and sensorless motor applications.

Uittreksel

Sensorlose beheer van 'n ysterlose permanentemagneet-sinchroonmasjien met outomatiese parameter afskatting

(Sensorless control of an ironless permanent magnet synchronous machine with automatic machine modelling)

A. Treurnicht

Tesis: MIng (Elekt)

Maart 2017

Hierdie projek ondersoek die sensorlose beheer van 'n nuwe geslag ysterlose permanentemagneet-sinchroonmasjien met 'n ongesplete pool vir gebruik by windopwekkers en elektriese voertuie. As gevolg van die eienskappe van hierdie ysterlose ongespletepoolmasjien kan net tru-EMK-metodes gebruik word om die rotorposisie sensorloos te bepaal. Hierdie tru-EMK-metodes kan nie die rotorposisie by rotorstilstand en lae rotasiespoed akkuraat afskat nie. By toepassings waar effektiwiteit by lae spoed baie belangrik is, is 'n rotorposisiesensor by lae spoed gebruik wat die rotorposisie afskat deur die magnetiese spreivelde agter die Halbach- permanentemagneetstruktuur te ontleed. Die beheerstelsel en die posisieafskatter vereis akkurate stelselparameters. 'n Ooplusparameteridentifikasiealgoritme is gebruik om al vyf stelselparameters af te skat sodra die stelsel aangeskakel word. 'n Gesloteluskombinasie van al die elemente te demonstreer. Die gedokumenteerde resultate bewys dat hierdie masjien saam met die stelselelemente in sensorlose motor sowel as opwekkertoepassings gebruik kan word.

Acknowledgements

I would like to thank the Centre for Renewable and Sustainable Energy Studies (CRSES) for the bursary without which this thesis would not have been possible. I would also like to thank my supervisors, Dr P.J. Randewijk and Dr J.M. Strauss, for their guidance and support towards the fulfilment of this project. Then I would like to thank the University of Stellenbosch for the opportunity to study towards a Master's degree and the use of their facilities. Lastly I would like to thank my parents for their support during my years of study.

Contents

List of Figures

List of Tables

Nomenclature

Constants

g	$9.81\,\mathrm{m/s^2}$

Variables

n	Normal direction to surface
M	Magnetisation vector
e_a	Generated BEMF in phase A
e_b	Generated BEMF in phase B
e_c	Generated BEMF in phase C
i_a	Phase A current
i_b	Phase B current
i_c	Phase B current
V_α	Alpha-axis voltage component
V_β	Beta-axis voltage component
i_α	Alpha-axis current component
i_β	Beta-axis current component
V_q	Quadrature-axis voltage component

V_d	Direct-axis voltage component
i_q	Quadrature-axis current component
i_d	Direct-axis current component
J	Moment of inertia
B_f	Friction coefficient
K_e	BEMF constant
λ_m	Rotor flux magnitude
P	Pole-pairs
R	Phase resistance
L	Phase inductance
L_d	Direct-axis inductance
L_q	Quadrature-axis inductance
T_m	Generated mechanical torque
α_e $(\ddot{\theta}_e)$	Electrical angular acceleration
α_m	Mechanical angular acceleration
ω_e $(\dot{\theta}_e)$	Electrical angular velocity
ω_m	Mechanical angular velocity
θ_e	Electrical angular position
θ_m	Mechanical angular position
m_2	Mass of added weight m_2 in kilogram
l	Length in meter

F_t	Tangential force
ω_n	Natural angular frequency
ζ	Damping ratio
σ	Real component of second-order complex pole
ω_d	Imaginary component of second-order complex pole
t	Time in seconds
k	Gain term
V_{ref}	Reference voltage
T_{ref}	Reference time
V_P	PWM period
D_A	Phase A PWM duty-cycle
D_B	Phase B PWM duty-cycle
D_C	Phase C PWM duty-cycle
K_P	Proportional gain
K_I	Integral gain
K_a	Current-loop gain term
K_b	Current-loop inflection-point location
K_c	Speed-loop gain term
K_d	Speed-loop inflection-point location
s	Laplace operator

Abbreviations

BEMF	Back electromotive force
PMSM	Permanent magnet synchronous machine
BLDC	Brushless direct current (machine)
BLAC	Brushless alternating current (machine)
SVPWM	Space vector pulse-width modulation
PWM	Pulse-width modulation
ADC	Analogue to digital converter
FEM	Finite element method
MSFRP-sensor	Magnetic stray field rotor position sensor
MSF	Magnetic stray field
IDRFPMSM	Ironless double-rotor radial flux permanent magnet synchronous machine
PM	Permanent magnet
LCR meter	Test equipment used to measure inductance, capacitance and resistance
MOSFET	Metal oxide semiconductor field-effect transistor
PCB	Printed circuit board
EMC	Electromagnetic compatibility
RF	Radio frequency
Q-factor	Quality factor
rms	Root mean square

avg	Average

Chapter 1

Introduction

1.1 Introduction

For decades synchronous machines had been extensively used in grid-tied applications. The high efficiency of synchronous machines made it popular for both generator and motor applications. Later on the rotor field-windings were replaced with permanent magnets. Permanent-magnet synchronous machines (PMSM) have the same high efficiency than conventional synchronous machines, but with less maintenance due to the removal of the field winding slip rings. Recent advances in electronic commutation allowed the use of PMSM in a wide variety of applications from rotor stand-still over the entire range of operation of the machine.

1.2 Problem statement

This project investigates the sensorless control of a new generation ironless non-salient pole permanent-magnet synchronous machine for electric vehicle and wind-turbine applications. The stator field has to be kept perpendicular to the rotor at all times to achieve maximum driving efficiency. This requires accurate rotor-position measurements.

Different sensorless rotor-position estimation techniques and control topologies are investigated. As the machine investigated in this project is ironless, only back-electromotive force (BEMF) estimation techniques can be used. BEMF estimation techniques are only effective when a measurable BEMF signal, requiring sufficient rotor speed, is available. BEMF rotor-position estimation techniques are ideal for wind-turbine application as wind turbines are always used above a minimum speed range. Electric vehicle application requires accurate rotor-position measurements from standstill over the full range of oper-

ation. As BEMF rotor-position estimation techniques cannot be used in the low-speed range, and no other sensorless-position estimation methods could be used with this machine, a position sensor needs to be implemented in the low-speed range should efficiency at low speed be a constricting factor. In industrial applications shaft-mounted position sensors are extensively used to measure rotor position when control around zero speed is required. The mechanical construction of some out-runner machines makes the use of shaft-mounted sensors particularly difficult.

1.3 Project overview

Chapter 2 presents a new type of rotor-position sensor which uses the magnetic stray fields on the outside of a Halbach permanent-magnet rotor array to calculate rotor position. Two measurement tracks at different distances behind the Halbach permanent-magnet array are identified and analysed through simulation. The advantages and drawbacks of both measurement locations are discussed and the simulated results are supported by measured results.

Sensorless-position estimation techniques require accurate machine parameters to estimate rotor position. The parameters of the ironless machine used in this project were originally unknown. The parameters of many machines are also not specified by machine manufacturers. There are many parameter-estimation techniques available in the literature for estimating one or two unknown parameters at a time. None of these methods can identify the complete model of an entirely unknown machine during open-loop operation. Chapter 3 presents an open-loop parameter estimation method used to identify the machine parameters at initial start-up. A closed-loop parameter estimation method is then used to update the machine model to its changing environment.

Chapter 4 discusses the two inverter versions that were developed during this project. The first inverter version was developed to show proof of concept and identify errors. In the second inverter version noise and ringing problems were eliminated. Good component choices and clever circuit design enabled fast switching times with minimal ringing overshoot and as a result a maximum inverter efficiency of 98.77 %.

Chapter 5 discusses the system integration and presents the closed-loop measurement results followed by a conclusion in Chapter 6.

1.4 Theoretical Background

Different driving topologies and sensorless rotor-position estimation techniques exist. All of these have different application specific advantages and drawbacks.

PMSM can be divided into brushless-AC (BLAC) and brushless-DC (BLDC) machines [1]. BLAC machines have sinusoidal BEMF waveforms, whereas BLDC machines have trapezoidal BEMF waveforms. When driving a PMSM, the highest efficiency is achieved by ensuring the stator-field lead or stator-field lags the rotor field by 90° electrical in a motor or generator application respectively [2].

One method used to control the angle of the stator magnetic field of a BLAC machine is vector control. With vector control, the voltages applied to the three motor terminals are pulse-width modulated in such a way as to create a smooth rotating stator-flux (space) vector, hence also referred to as Space Vector PWM. This allows the stator field to be kept perpendicular to the rotor, thereby ensuring maximum inverter efficiency.

Another method implemented in controlling the stator magnetic flux vector of BLDC machines is trapezoidal control. In trapezoidal control the machine is driven by only two of its three terminals, leaving the third terminal floating. The stator-flux vector can therefore be in only one of six possible electrical angle locations, 60° electrical apart. This therefore means that the angle between stator flux vector and the rotor alternates between 60° and 120° electrical, depending on rotor position. As a result the driving efficiency of trapezoidal control is lower than that of vector control. Trapezoidal control is particularly popular in applications with limited microcontroller processing capability.

All of these methods require knowledge of rotor position. Rotor position is generally measured with shaft-mounted rotary position sensors. The mechanical construction and application of some machines prevent shaft-mounted sensors from being used, e.g. in out-runner motors. Over the years many sensorless rotor-position measurement techniques have been developed, all having their own limitations and drawbacks. Eliminating rotor-position sensors has the advantage of increasing the robustness and reliability of the machine application and decreasing cost.

Sensorless rotor-position estimation techniques can be categorised under system-state-estimator techniques, BEMF-techniques and invasive techniques (inductance variation technique and core hysteresis technique) [3].

1.4.1 Rotor-position estimation techniques used with vector control

One of the established methods of sensorless vector control uses a system-state-estimator to calculate the BEMF voltage with the help of an accurate machine model. Qiu et al. [4] implemented an extended Kalman filter estimator to determine rotor position. According to Qiu, one of the drawbacks of this method is that, especially in industrial applications, a detailed machine model is not always available.

Kim et al. [5] formulated a method to sensorlessly calculate the rotor position by extracting the permanent-magnet rotor flux linkage from an accurate machine model. The applied terminal voltages and measured phase currents were used to determine the system state. This method is not BEMF dependent, and therefore enabled Kim to measure the rotor position at very low speeds. Kim explained that conventional sensorless rotor-position methods are limited to a specific speed range and most sensorless methods are only usable at speeds greater that 10 % of the rated speed of the machine. The method Kim presented can be implemented at speeds from 1.5 % of the rated speed to high speeds. However, it should be noted that this method also requires an accurate machine model.

1.4.2 BEMF rotor-position estimation techniques with trapezoidal control

When controlling BLDC machines, sensorless trapezoidal control is an attractive way to reduce cost and increase reliability. In trapezoidal control the machine is driven between two of its three phase terminals leaving the third phase terminal floating, as shown in Figure 1.1.

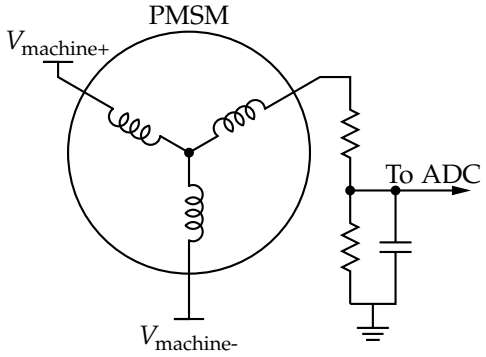

Figure 1.1: Trapezoidal-control wiring diagram

As there is no current flowing in this floating third phase, the voltage drop between the neutral point and the floating phase terminal is purely the induced BEMF of the spinning

rotor. The BEMF measured at any floating phase terminal is dependent on the phase shift related to that phase terminal, the rotor position and rotor speed [6]. It is therefore possible to extract the rotor position and speed information from the induced BEMF. These BEMF rotor-position measurement techniques can be categorised under BEMF zero-crossing detection, BEMF integration, stator third-harmonic component analysis and free-wheeling diode-conduction detection [6].

With BEMF zero-crossing detection the voltage on the unexcited phase is frequently checked for a zero-crossing point where the BEMF on that phase transitions from positive to negative or vice versa [6]. The BEMF on the unexcited phase is calculated by subtracting the neutral-point voltage from the unexcited terminal voltage. Voltage spikes can occur due to commutation or free-wheeling diode conduction leading to false zero-crossing measurements [7]. Measurement timing with this method is therefore quite critical.

Damodharan et al. [7] proposed a method of detecting the BEMF zero crossings from the line-to-line terminal voltages. Damodharan explained that the advantage of this method is that it eliminates the need for a neutral or virtual neutral point. This elegant method uses the flat BEMF property of BLDC machines to extract a scaled and inverted version of the undriven phase BEMF from the line-to-line terminal voltages.

Darba et al. [6] presented a method of detecting rotor position by using the BEMF amplitude instead of the zero crossings. Darba concluded that this method provided better performance during transients and more accurate commutation at high rotational speeds. Darba did however not specify the performance results of this method at low rotational speeds.

1.4.3 Invasive techniques

There are two types of invasive techniques that can both be used to detect rotor position at standstill [3]. The first technique uses the rotor-position dependency of the inductance of a salient-pole PMSM to determine rotor position. The second method analysis the rotor-position dependent change in phase self-inductance caused by B-H stator iron characteristics

Mizutani et al. [8] developed an algorithm that uses the inductance of a salient-pole PMSM to measure rotor position. The phase inductance was measured by injecting periodic current pulses. Since the inductance of a salient-pole machine is rotor-position dependent, the rotor position can be calculated from the measured phase inductance.

Mizutani explained that BEMF measurement techniques do not work well in the low speed range since developed BEMF is speed dependent. Inductance methods work well in the low-speed range and at standstill, but do not work well in the high-speed range due to the magnitude of the developed BEMF voltage.

Scaglione et al. [9] introduced a method called first-pulse technique. Scaglione explained that the phase self-inductance and phase resistance of a non-salient PMSM is also rotor-position dependent due to the B-H stator iron characteristics. These rotor-position dependent variations are quite small. The phase self-inductance magnitude was measured by using pulse injection.

It should be noted that both of these invasive techniques require knowledge of the machine model to work correctly and that these methods can only be used in a limited speed range [8], [9]. Unfortunately, because the machine under investigation is a non-salient, ironless machine, none of these techniques are applicable due to the lack of saliency and absence of any iron in the stator or rotor of the machine.

The one thing the various sensorless control or regulation methods used have in common is that they all require an accurate mathematical machine model.

1.4.4 Comparison between BLAC and BLDC machines

Miyamasu et al. [1] conducted a study in which the efficiency of a BLAC and a BLDC machine was evaluated. In this study vector control (BLAC-drive) and trapezoidal control (BLDC-drive) were used to drive both BLAC and BLDC machines. In the test where the BLAC machine was driven by trapezoidal control, the efficiency is about up to 1.7 % lower than the test where the BLAC machine was driven by vector control. The case study in [1] therefore proves that a BLAC machine can be driven with trapezoidal control but will result in a reduced efficiency.

1.5 Thesis outline

Chapter 2 introduces a sensor which uses the magnetic stray field behind the Halbach permanent-magnet array to calculate rotor position. In Chapter 3 the parameter-estimation technique is discussed that identifies the machine parameters before closed-loop sensorless operation can be implemented. Chapter 4 presents the inverter developed to drive the machine. The closed-loop system implementation is discussed in Chapter 5. The closed-loop system results are then discussed in Chapter 6 and a conclusion is drawn

in Chapter 7.

Chapter 2

Rotor-position measurement with Magnetic Stray Fields

2.1 Introduction

Vector control of synchronous machines requires accurate rotor-position measurements. In commercial applications, rotor position is generally measured with shaft-mounted position sensors such as Hall sensors. Due to the mechanical construction of some machines, shaft-mounted sensors cannot always be used. This chapter introduces an alternative technique that uses the magnetic stray fields behind a Halbach permanent magnet array to determine rotor position. This technique has been implemented on commercial permanent magnet synchronous machines in the past (machines with radial and parallel-magnetised rotor arrays). This is, however, the first time that this technique is implemented on a machine with a Halbach permanent magnet array.

2.2 Chapter outline

The literature study section in 2.3 discusses research related to magnetic stray-field position estimation and distinguishes between different magnet arrays. The magnetic stray fields surrounding a double-rotor Halbach permanent magnet array are investigated through simulation in 2.4. The optimal sensor placement positions are discussed. Different measurement techniques and hardware implementations are introduced in 2.5 and 2.6. Lastly the measured results are compared with the simulated results in 2.7 and a conclusion is drawn in 2.8.

2.3 Literature related to Magnetic Stray Field rotor-position measurement

2.3.1 Background

Permanent magnet synchronous machines (PMSM) became very popular due to their high efficiency, high-power density, etc. [10]. Vector control requires an accurate knowledge of rotor position [11]. In most commercial systems, rotor position is measured using shaft-mounted rotary position sensors e.g. Hall sensors. The mechanical construction of some of these machines prohibits the placement of shaft-mounted position sensors. To overcome this problem, an alternative approach was therefore studied to measure the rotor angle by analysing the magnetic stray field behind the permanent magnet rotor array.

Kim et al. [11] used two linear Hall sensors to measure the rotor permanent magnet edge field of a BLAC PMSM in the axial direction. The measured edge fields were used to estimate the position of the rotor. Kim mentioned the presence of a third harmonic non-linearity component but could not explain its cause. An algorithm was, however, developed to correct the measurement error. This method produced good measurement accuracy.

Sergeant et al. [12] used three digital Hall sensors to measure the magnetic stray fields at specific locations on the outside of an out-runner BLDC PMSM. Due to the radial magnetisation of the rotor's permanent magnet array, the magnetic stray fields on the outside of the rotor can be used to generate an angle-dependant pulse train similar to that generated by conventional axle-mounted Hall sensors. Sergeant claimed that good results were recorded with three sensors placed at a 3 mm distance behind the outer shell of the rotor. It was noted that the stator current caused a measurable phase shift that is directly proportional to the current magnitude.

2.3.2 Rotor magnet magnetisation

Most commercially manufactured PMSM make use of radial or parallel magnetised rotor magnet arrays for BLDC and BLAC machines respectively [13]. Kim et al. [11] conducted his study on a BLAC machine with a parallel-magnetised magnet array whereas Sergeant et al. [12] conducted his study on a BLDC machine with a radial-magnetised permanent magnet array. The difference between the radial or parallel-magnetised magnets is shown in Figure 2.1 where vector n indicates the normal direction to the surface and M indicates

the magnetisation vector [13]. The radial magnetisation is along the radius while parallel magnetisation is parallel to the edge of the magnet [13].

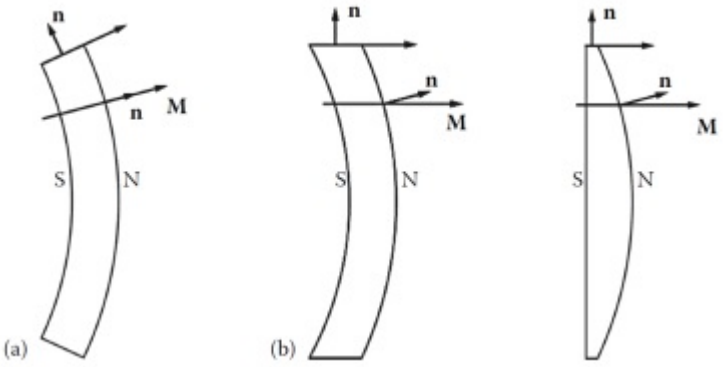

Figure 2.1: Magnetisation of magnets: (a) Radial magnetisation and (b) parallel magnetisation [13]

Figure 2.2 shows a top-view diagram of a radial magnet array in air and its field lines [13]. Please note the polarisation direction of the magnets in the array.

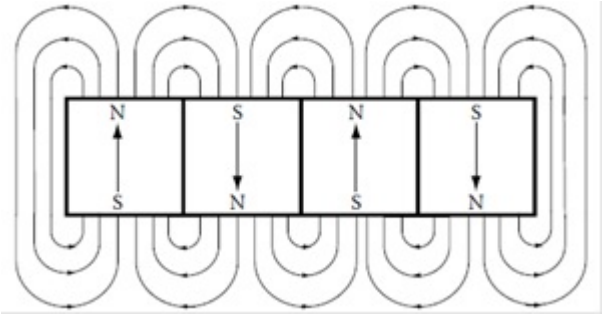

Figure 2.2: Radial magnet array in air [13]

The difference in air-gap flux density versus rotor position of these two topologies is shown in a FEM simulation performed by [13] in Figure 2.3. As shown in Figure 2.3, the radial-magnetised array produces a rectangular air-gap flux density distribution, whereas the parallel-magnetised array produces a sinusoidal air-gap flux density distribution [13].

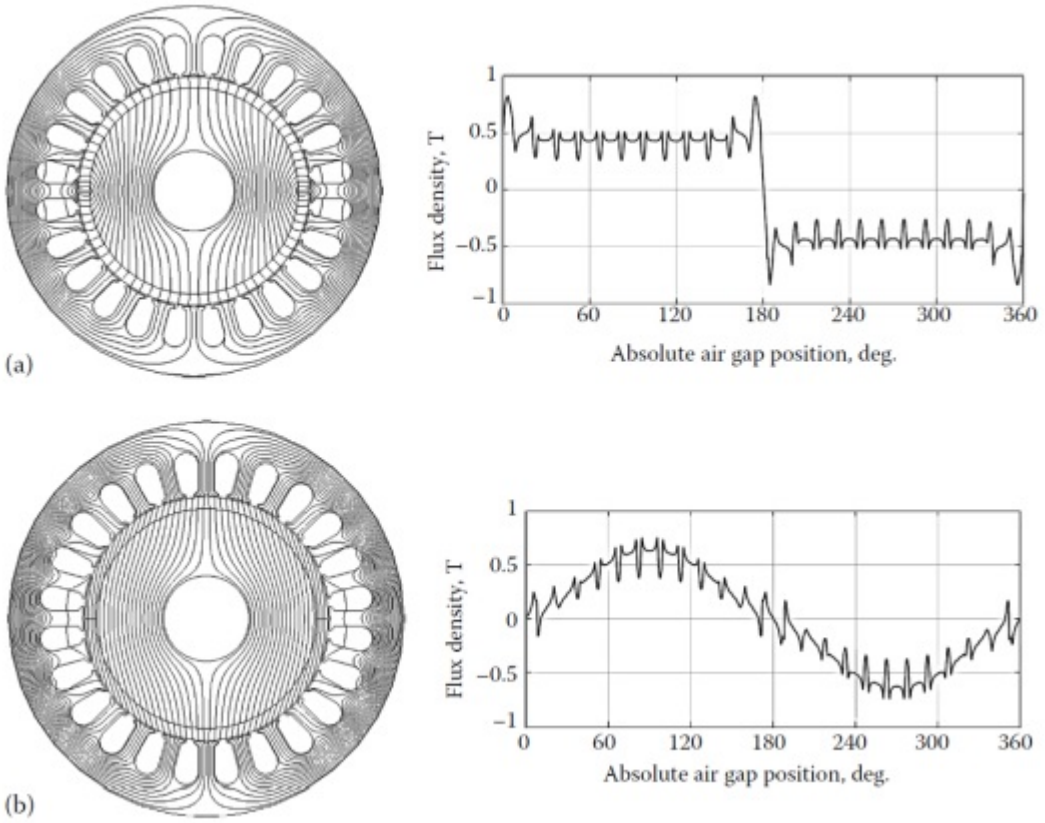

Figure 2.3: Air-gap flux density distribution versus rotor position of: (a) radial-magnetised PMSM and (b) parallel-magnetised PMSM [13]

The downside of these topologies is that a magnet-backplate and\or iron yoke needs to be added to shorten the flux path through air. These iron structures in turn cause cogging torque, core losses and additional weight.

The Halbach permanent magnet array is constructed by combining a radial and an azimuthal magnet array in the structure presented in Figure 2.4 [13]. As shown in Figure 2.4, most of the flux lines are on one side of the magnet array, therefore no iron back-plate is needed. Please note the magnet directions in the Halbach array in Figure 2.4.

Figure 2.5 shows the air-gap flux density distribution versus rotor position of an inside-Halbach permanent magnet array machine [13]. As shown in Figure 2.5, the air-gap flux density distribution is sinusoidal.

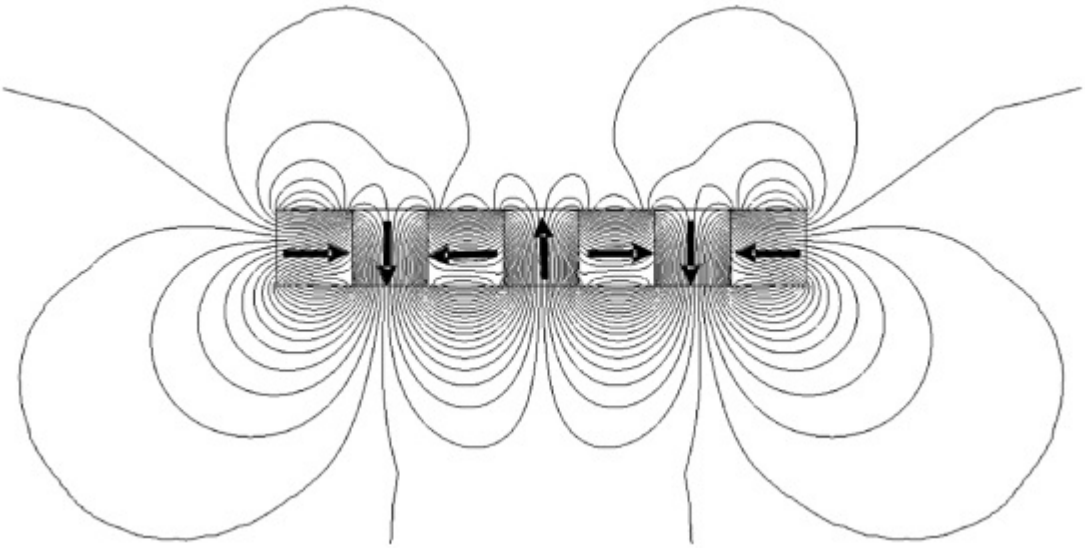

Figure 2.4: Flux lines of a seven-element Halbach permanent magnet array [13]

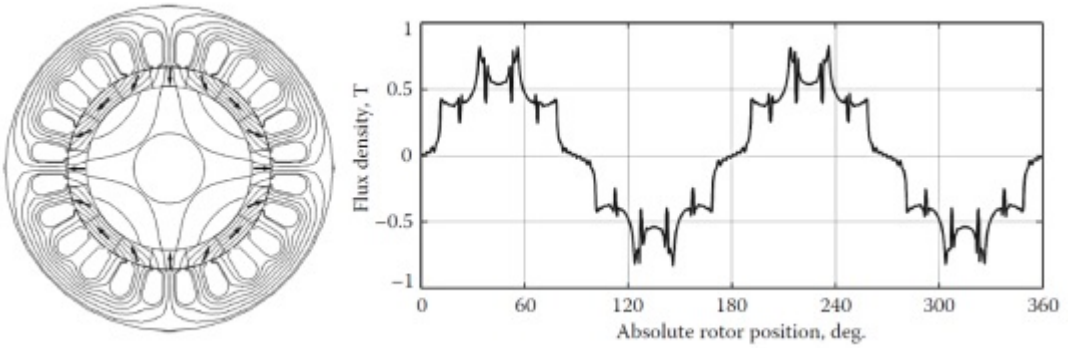

Figure 2.5: Inside-Halbach permanent magnet array machine's air-gap flux density distribution versus rotor position [13]

2.4 Method of implementing Magnetic Stray Field Rotor Position Sensor

2.4.1 The double-rotor radial flux permanent magnet synchronous machine

Between 2013 and 2015, three ironless double-rotor radial flux permanent magnet synchronous machines (IDRFPMSM), one with aluminium body and two with carbon fibre bodies were developed by the University of Stellenbosch as shown in [14] and [15]. Figure 2.6 shows a picture of the third IDRFPMSM. The outside rotor of the second IDRFPMSM edition is also used in this study due to its thinner magnet mounting wall.

Figure 2.6: IDRFPM synchronous machine

The mechanical construction of these machines prevents commercial absolute-position sensors from being mounted on their rotor shafts. A custom sensor is therefore developed to measure rotor position. These machines have no iron structure. The magnetic flux rather flows through the Halbach permanent magnet array. Since the carbon fibre is non-magnetic, the magnetic stray field behind the Halbach permanent magnet array is unaffected by the machine body. It should be possible to use the magnetic stray fields on the outside of the permanent magnet Halbach array rotor to determine rotor position.

2.4.2 Modified Ansys Maxwell IDRFPMSM magnetic field simulation

In 2015 Oosthuizen et al. [15] compiled an Ansys Maxwell simulation of the IDRFPMSM. Oosthuizen's simulation was modified for this investigation to show the magnetic stray field (MSF) lines and flux density behind the Halbach permanent magnet array. Figure 2.7 shows the field lines and flux density for one electrical rotation.

Figure 2.8 shows the magnetic stray field direction on the 2.5 mm sensor path behind the Halbach permanent magnet array for one electrical rotation.

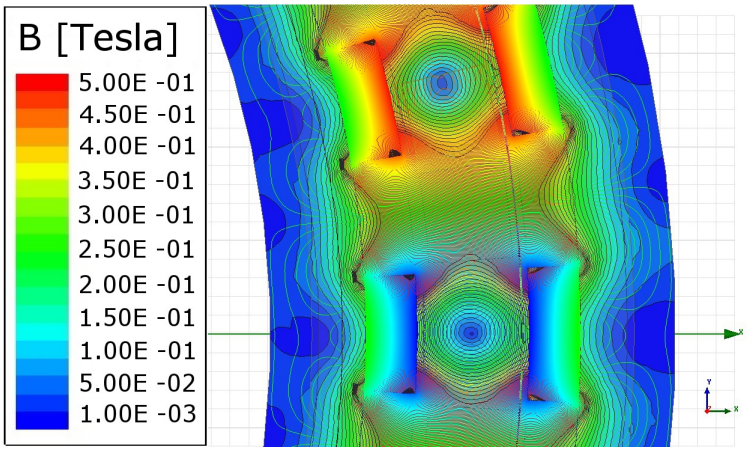

Figure 2.7: IDRFPMSM field lines and flux density for one electrical rotation

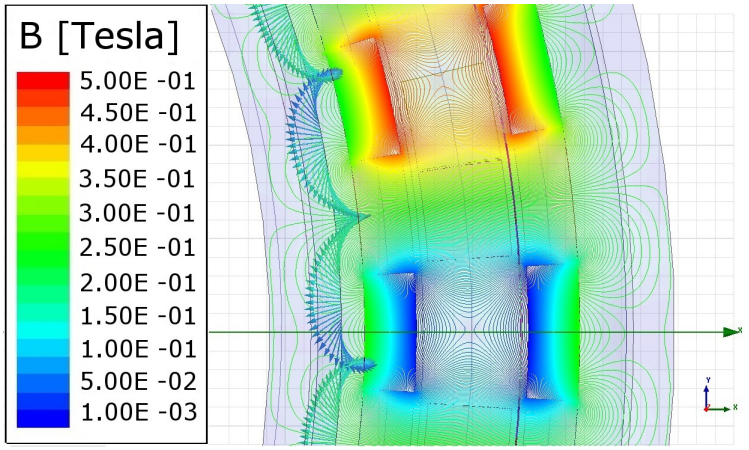

Figure 2.8: IDRFPMSM magnetic stray-field direction on a 2.5 mm sensor path behind Halbach array

The green and red graphs in Figure 2.9 show the azimuth and radial MSF components on the 2.5 mm path for one electrical rotation. These components in turn are used to calculate the MSF angle and magnitude shown by the blue and purple graphs respectively.

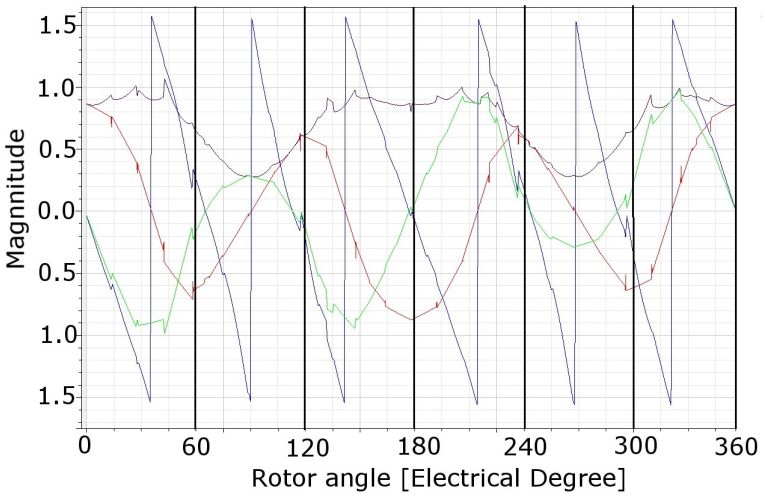

Figure 2.9: MSF components on 2.5 mm sensor track

Due to lack of freedom in the Ansys Maxwell environment it was decided to rather do an additional simulation with a MATLAB script. The Ansys Maxwell simulation does, however, provide reference.

2.4.3 MATLAB script simulation

A Matlab simulation script is written to analyse the magnetic fields surrounding the Halbach permanent magnet array. This simulation starts by calculating the magnetic field around a single permanent magnet. The magnetic field around the Halbach permanent magnet array is then assembled by means of superposition.

Simulation of the magnetic field around a single magnet

Figure 2.10 shows the simulated magnetic field density (coloured contours), magnetic field direction (black arrows) and the magnetic field lines (red stream lines) surrounding a single permanent magnet.

Constructing a Halbach permanent magnet array

The simulated magnetic field data of the single-magnet is rotated at 0°, 90°, 180° and 270° angles. The multi-element Halbach permanent magnet array is constructed with the rotated magnets by means of superposition to form a linear machine rotor as shown in Figure 2.11. The magnetic field of the Halbach permanent magnet array found at the round rotor of the IDRFPMSM is the same as that of a linear machine with an infinite amount of Halbach permanent magnet array elements. To simplify the simulation, a

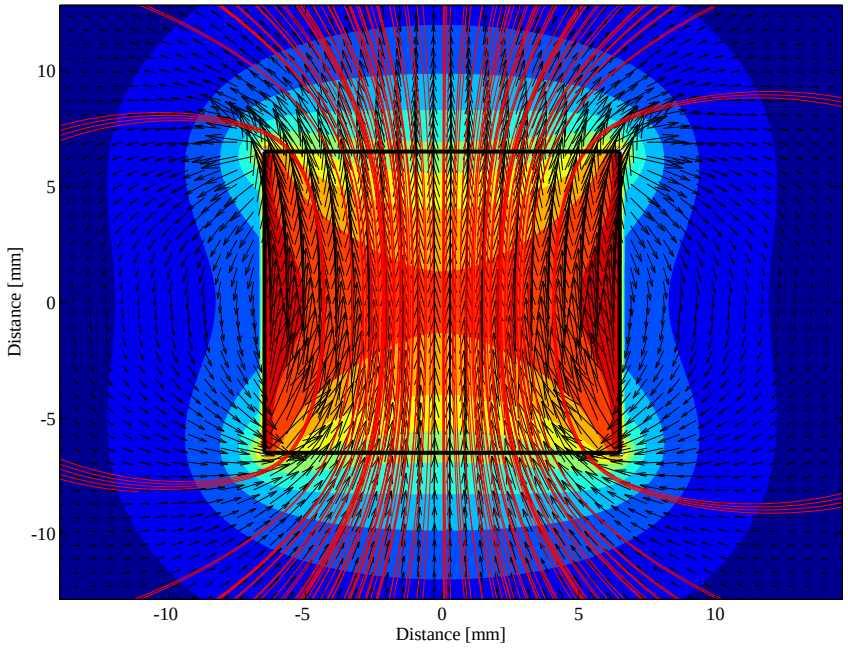

Figure 2.10: Simulated magnetic field around a single permanent magnet

linear machine configuration with multiple Halbach permanent magnet array assemblies is used instead of a round rotor configuration. Since the magnetic stray fields of the Halbach permanent magnet array at the ends of the linear machine rotor tend to deform into the open space (as shown in Figure 2.4), only the simulated magnetic stray fields at the centre Halbach permanent magnet array is used.

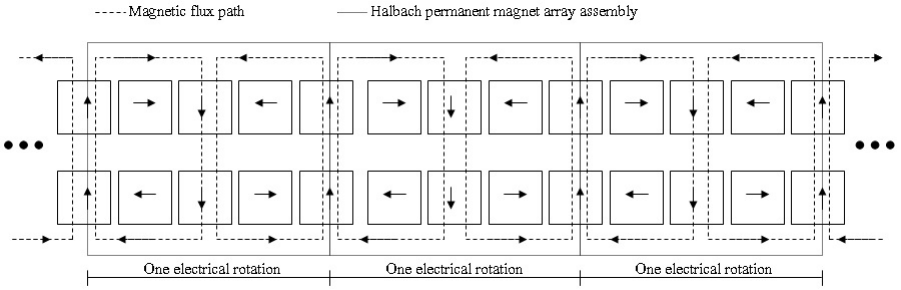

Figure 2.11: Linear machine double-rotor Halbach permanent magnet array assembly

Figure 2.12 shows the simulated field around the double-rotor linear Halbach permanent magnet array for one electrical rotation in the centre of the machine. In this simulation the magnetic field density (coloured contours), magnetic field direction (black arrows) and the magnetic field lines (red stream lines) are indicated.

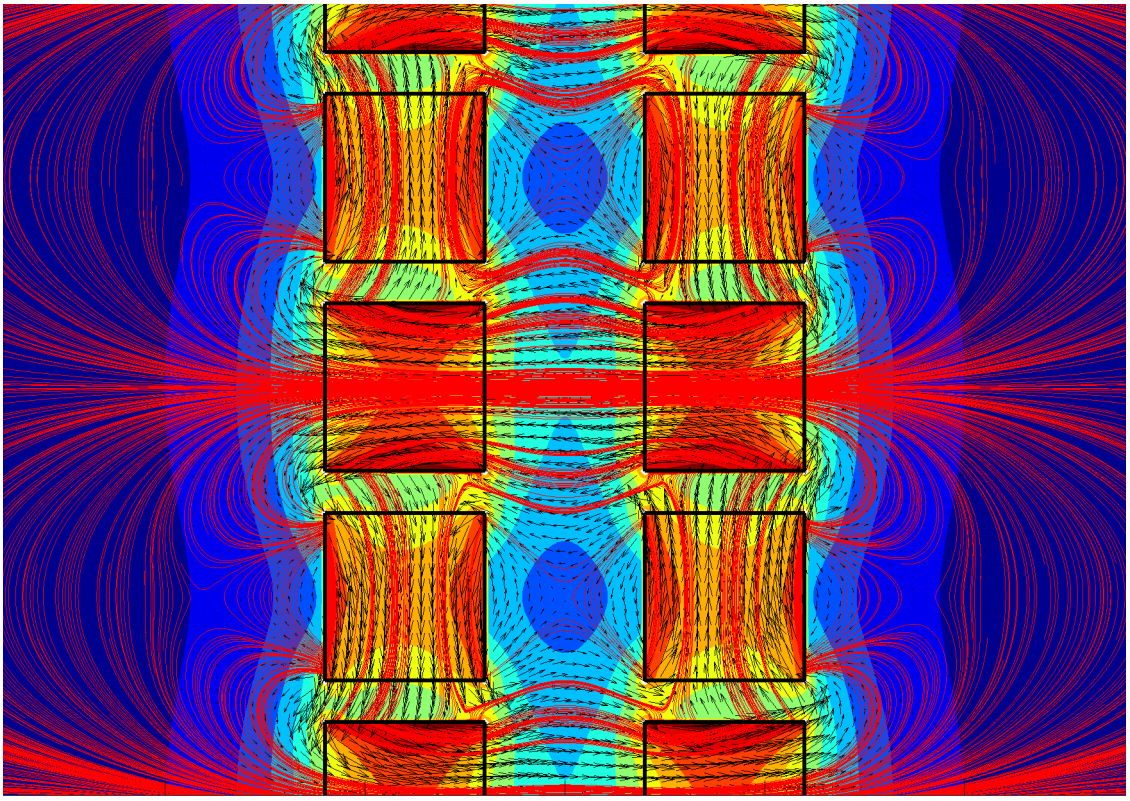

Figure 2.12: Simulated magnetic field around double-rotor Halbach permanent magnet array assembly for one electrical rotation

Figure 2.13 shows the simulated magnetic stray field (MSF) behind the Halbach permanent magnet array assembly for one electrical rotation. In this simulation the close-field region is found between 0 mm and 5 mm, intermediate-field region found between 5 mm and 10 mm and the far-field region is found above 10 mm behind the permanent magnet Halbach array.

Figure 2.14, 2.15 and 2.16 shows the simulated MSF angle at increasing distances behind Halbach permanent magnet array assembly for one electrical rotation. The three graphs in Figure 2.14 fall in the close-field region. It should be noted that the magnetic stray-field angle completes three rotations for every electrical angle rotation in the close-field region. The non-linearities present at these three graphs are at a maximum at a distance of 0.5 mm behind the Halbach array. As the distance behind the magnet array increases, the magnetic stray field angle becomes more linear till a distance of 2.5 mm is reached. If the distance is further increased, the MSF angle again become more non-linear till the 5 mm point is reached. This behaviour can be expected just by looking at the shape of the field lines in Figure 2.13 at certain distances behind the magnet array.

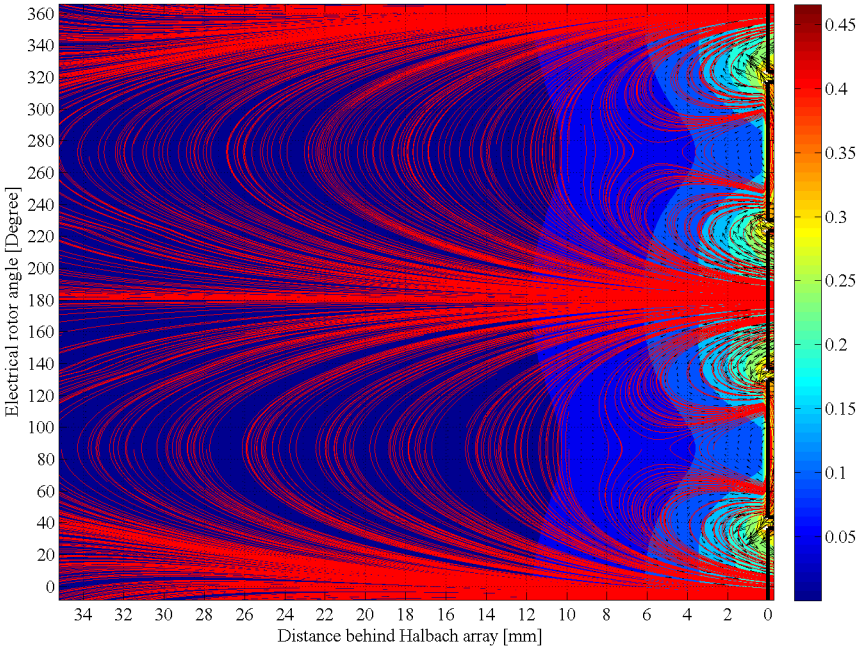

Figure 2.13: Simulated magnetic stray-field behind Halbach permanent magnet array assembly for one electrical rotation

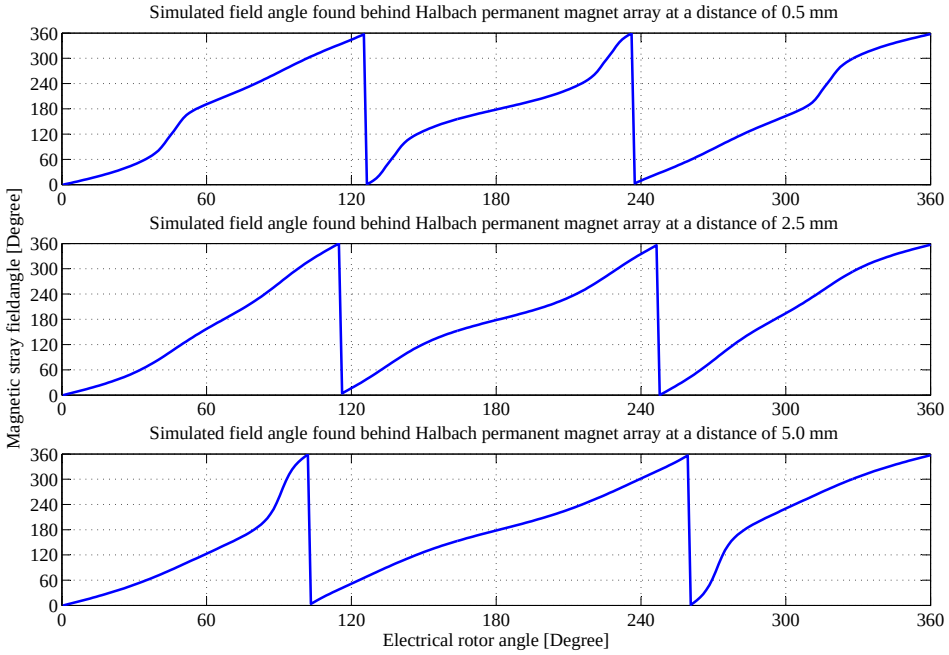

Figure 2.14: Simulated magnetic stray close-field angle at increasing distances behind Halbach permanent magnet array assembly for one electrical rotation

Should the distance behind the magnet array be further increased beyond the 5 mm point, the MSF angle transitions from three MSF rotations per electrical rotation to one MSF rotation per electrical rotation at 10 mm. This transition is clearly illustrated by the three graphs in Figure 2.15.

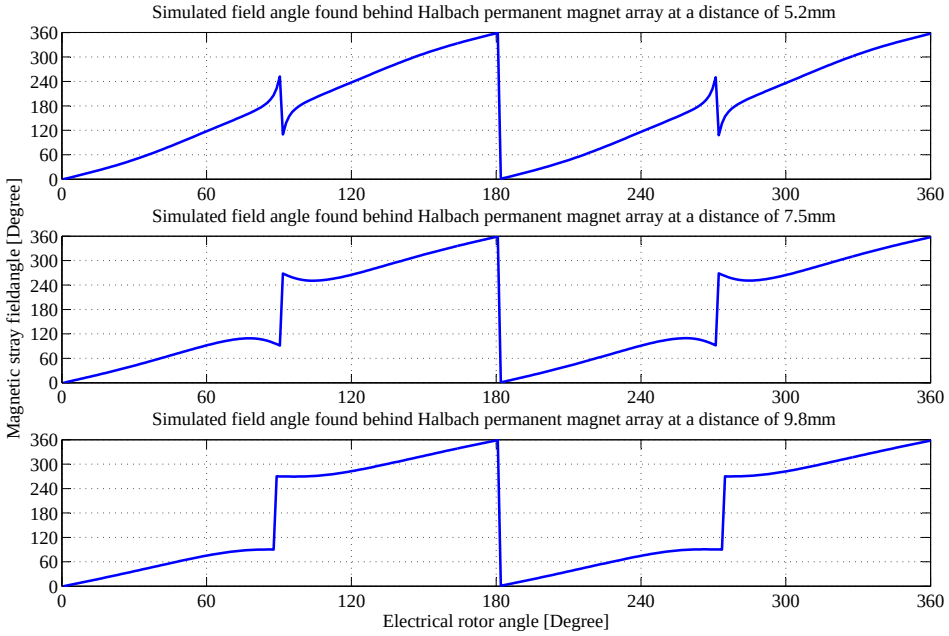

Figure 2.15: Simulated magnetic stray intermediate field angle at increasing distances behind Halbach permanent magnet array assembly for one electrical rotation

Beyond the 10 mm point the MSF angle completes one MSF rotation per electrical rotation in the far-field region as shown in Figure 2.16. In this region the MSF angle non-linearity is at a maximum at a distance of 10 mm. The MSF angle graph becomes linear as the distance is increased to 15.6 mm. Above 20 mm, however, the MSF angle-period shortens as shown in Figure 2.16.

By analysing the MSF-angle graphs in Figure 2.14, 2.15 and 2.16 it becomes clear that the ideal sensor placement locations that would produce the most linear MSF-angle measurements would be at a distance of 2.5 mm in the close-field region and 15.6 mm in the far-field region behind the Halbach permanent magnet array. It should be mentioned, however, that these ideal sensor placement distances are directly related to y-axis magnet size (length of the Halbach array) and spacing between magnets. Should these measurements change, the ideal sensor placement location will change accordingly.

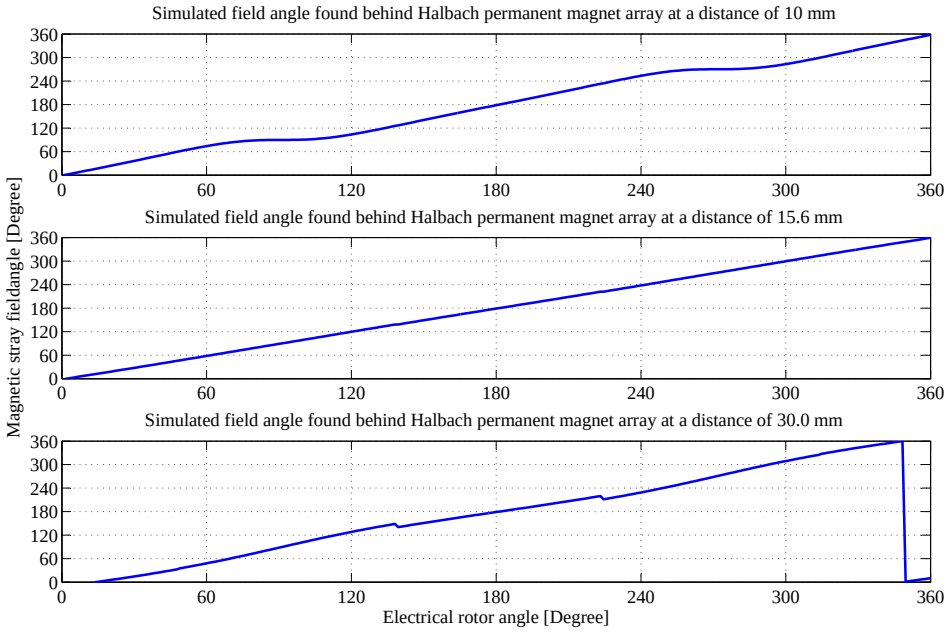

Figure 2.16: Simulated magnetic stray far-field angle at increasing distances behind Halbach permanent magnet array assembly for one electrical rotation

2.4.4 MSF measurement method and sensor placement

The technique presented by Sergeant in [12] focuses specifically on rotor-position measurement with the magnetic stray close-fields of a parallel-magnetised permanent magnet array rotor found in BLDC motors. In [12] the author constructed a three-element Hall-effect rotor position sensor by positioning three digital Hall sensors at 120° electrical angles around the outside rotor facing the radial axis. This method provides a sixty electrical-degree resolution, which is sufficient for BLDC motor control (trapezoidal control), but not accurate enough for vector control.

Kim et al. [11] positioned two linear Hall sensors 90° electrical out of phase at the rotor edge of a BLAC machine. Kim used the magnetic stray close-fields at the magnet edge of a radial magnetised permanent magnet array rotor to measure rotor position.

The magnetic stray close-field angles of the permanent magnet arrays used by Kim and Sergeant complete a single MSF-rotation for every electrical rotation. The implementation investigated in this study, however, is rotor-position measurement for an IDRFPMSM from magnetic stray fields of a Halbach permanent magnet array rotor. Since this Halbach magnet array is different from the radial-magnetised and parallel-magnetised permanent magnet arrays used in [12] and [11], the magnetic stray field is significantly different as

well.

Rotor position from close-field measurement

The close- and far-field sensor placement positions are discussed separately. Let's start with the magnetic stray close-field measurements. Since the magnetic stray close-field angle completes three rotations for every electrical angle rotation, more information is needed to identify the region of operation at initial start-up. The problem at hand is at which of the three MSF rotation regions the sensor initially starts measuring when the power is switched on. A possible solution could be to use the MSF relative magnitude measurements at different positions on the same 2.5 mm sensor track. Figure 2.17 shows the simulated MSF vector angle and magnitude for one electrical angle rotation at a distance of 2.5 mm behind the Halbach permanent magnet array. Figure 2.17 shows that the sinusoidal shaped MSF vector magnitude has minimums or dips at 90° and 270° electrical angles.

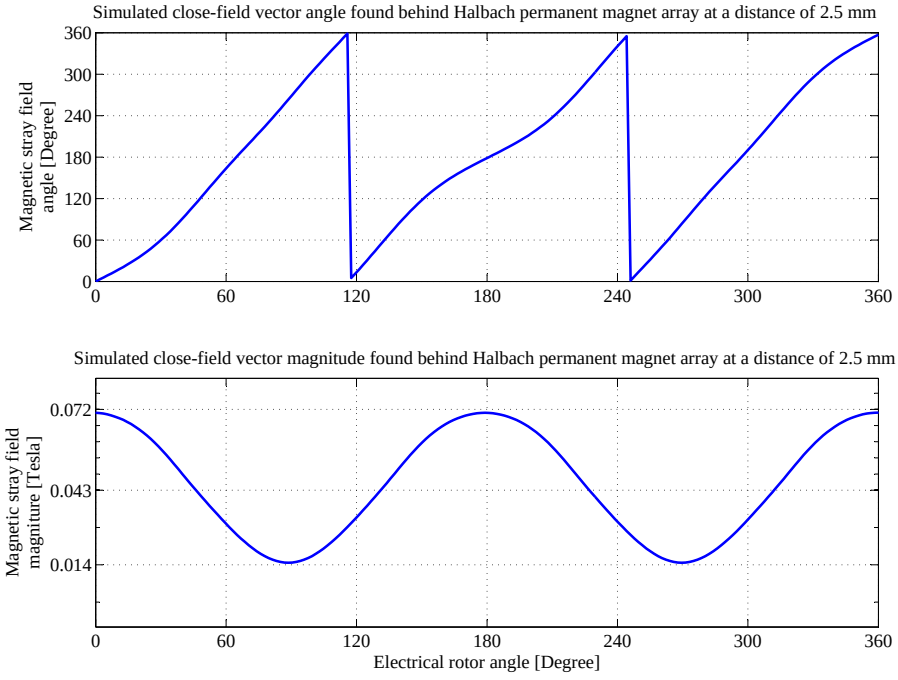

Figure 2.17: Simulated MSF vector angle and magnitude for one electrical angle rotation at a distance of 2.5 mm behind the Halbach permanent magnet array

Three measurement locations are selected at -60°, 0° and 60° electrical at a distance of 2.5 mm behind the Halbach permanent magnet array as shown in Figure 2.18.

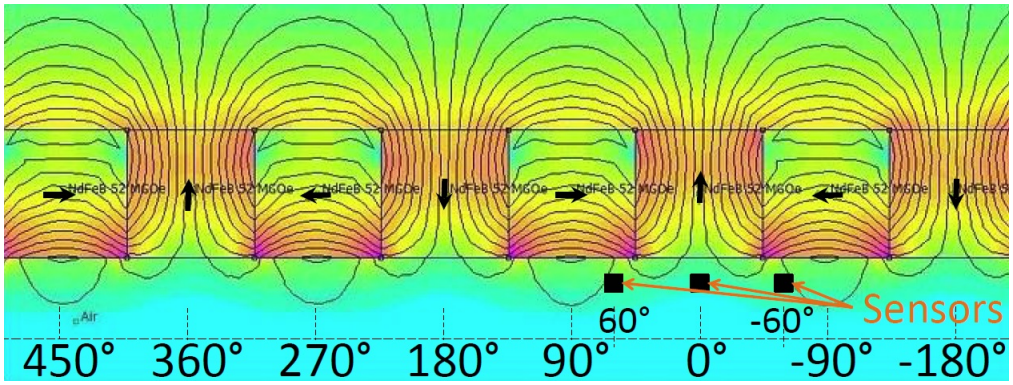

Figure 2.18: Magnetic stray close-field sensor placement behind Halbach permanent magnet array

This sensor spacing ensures that the MSF magnitude measurements have six equally spaced dips per electrical rotation as shown in Figure 2.19. Figure 2.19 shows the simulated MSF angle and magnitude graphs at the 0°-centre position in blue and the MSF magnitudes of the two side sensor locations at -60° and 60° electrical in the green and red graphs respectively. The initial start-up region of operation can now be identified by comparing the centre MSF angle measurement with the vector magnitudes at all three locations (therefore, which of the three MSF sensors are experiencing a magnitude dip).

2.5 Hardware development of MSF-sensor version 1.0

2.5.1 MSF-sensor version 1.0

Two types of magnetic sensors were considered. The first is a magnetoresistive sensor, the AFF755B manufactured by Sensitec. This magnetoresistive sensor measures magnetic field density and direction. At first glance this sensor looked like the ideal option. After further investigation it came to light that the nature of the magnetoresistive phenomenon and construction of this sensor prevents it from distinguishing between a change in magnetic field density and direction. Since both the magnetic field density and direction is unknown, this sensor will not be ideal. The second sensor considered is a linear unidirectional Hall sensor, the SS496A1 manufactured by Honeywell. This sensor measures the magnetic field density on a single axis with the Hall-effect phenomenon as described by:

$$V_H = I \times B \ . \tag{2.1}$$

The decision was made to rather measure the magnetic field density on two separate axes with two orthogonally positioned SS496A1 sensors at each measurement location and calculate the MSF magnitudes and angles from these measurements.

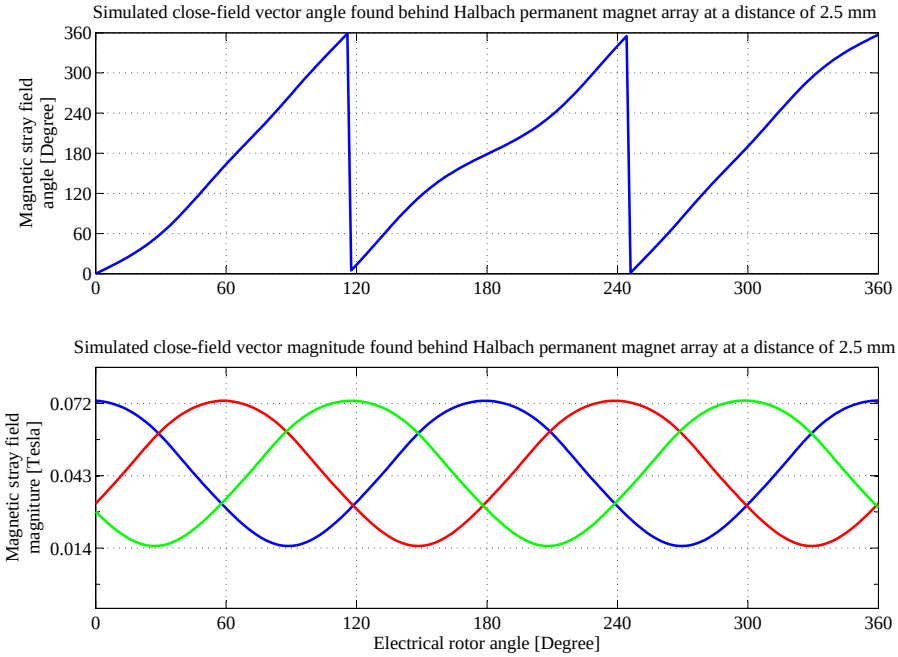

Figure 2.19: Simulated MSF vector angle at the centre sensor location and vector magnitudes of all three measurement locations for one electrical angle rotation at a distance of 2.5 mm behind the Halbach permanent magnet array

A MSF-sensor PCB containing a microcontroller and linear Hall sensors was developed. This MSF-sensor PCB is shown in Figure 2.20. The microcontroller and -60°, 0° and 60° electrical angle sensor locations are indicated in Figure 2.20. By close inspection of Figure 2.20 it will be noticed that each sensor block contains a tangential-positioned sensor at the bottom and a radial-positioned sensor right on top of it.

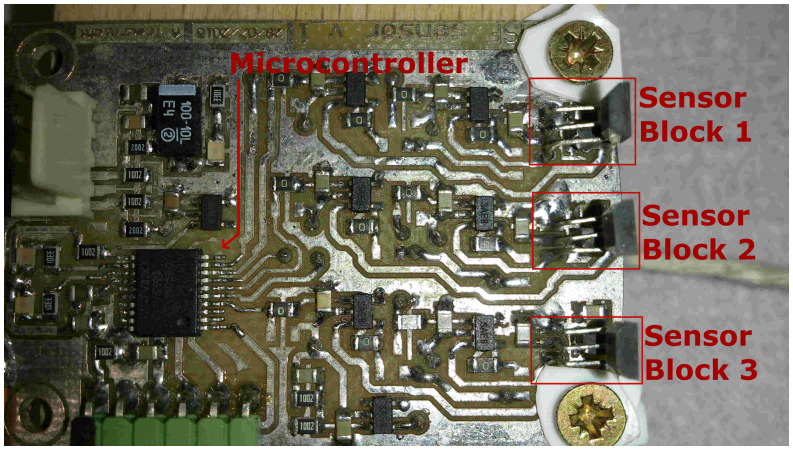

Figure 2.20: The first MSF-sensor PCB

Figure 2.21 shows the component interaction block diagram of the first MSF-sensor PCB. The SS496A1 linear Hall sensor requires a 5 V supply rail. This linear Hall sensor delivers its analogue result output as a voltage level that changes between 0.5 V and 4.5 V for a flux density change of between ±85mT. The PIC24FV32KA304 microcontroller is chosen since it can operate from a 5 V supply rail and supports all the necessary peripherals. Figure 2.21 shows that six 12-bit microcontroller ADC channels are used to measure the component field strength outputs of the six linear Hall sensors in the three sensor blocks. The microcontroller calculates the MSF magnitude and angle components at the three measurement locations from the measured radial and tangential components. These MSF magnitude and angle components in turn are used to calculate the rotor electrical angle. The MSF-sensor output is delivered as a varying duty cycle on a PWM signal.

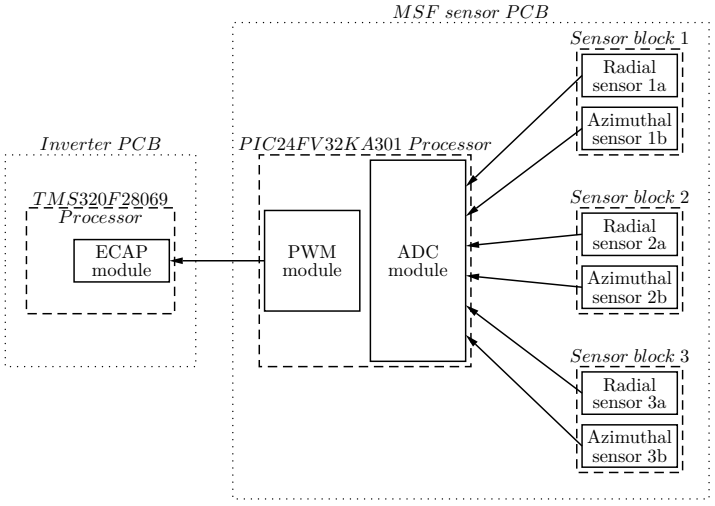

Figure 2.21: First MSF-sensor component interaction block diagram

Figure 2.22 shows the microcontroller's firmware flow diagram. As shown in Figure 2.22, at initial power-on the 60 MHz internal oscillator, 1 msec internal interrupt timer, six 12-bit ADC modules, a 10-bit 10 kHz PWM module and the applicable input-output-pins are configured. From that point on all operation continues in an interrupt loop. Once an interrupt is triggered, the six analogue Hall-sensor outputs are measured with the ADC module of the microcontroller. The MSF magnitudes and angles at the sensor locations are thereafter calculated from the measured components. The rotor angle is synthesized from the MSF data. Lastly the calculated rotor angle is delivered to the inverter in the form of a varying duty-cycle on a 10 kHz PWM signal.

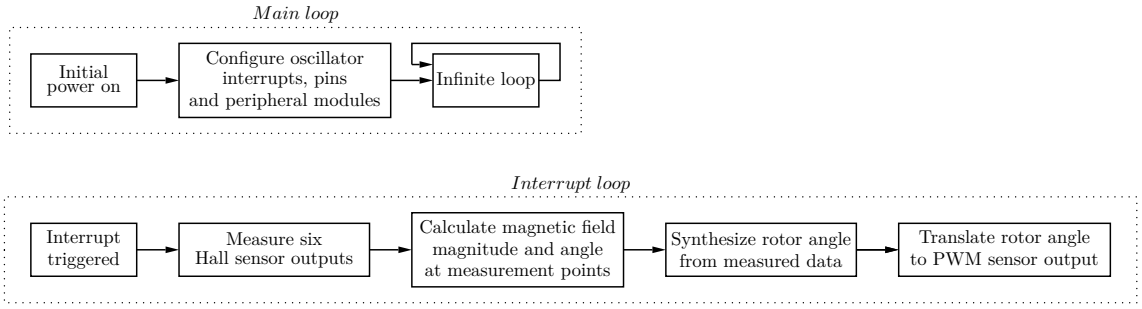

Figure 2.22: MSF-sensor V1.0 firmware flow diagram

2.5.2 Magnetic stray close-field measurements with the first MSF-sensor

At the time of the development of the first MSF-sensor, the third IDRFPMSM was still under construction. The rotor of the second IDRFPMSM was used to measure the magnetic stray close-field. Figure 2.23 shows a picture of the outside rotor of the second IDRFPMSM.

Figure 2.23: Outside rotor of second IDRFPMSM

Figure 2.24 shows the angles and magnitudes of the MSF measured at the thee sensor locations (-60°, 0° and 60°) over two electrical rotations. The blue, red and green curves show the measured angles and magnitudes of the MSF at sensor blocks one to three respectively. The simulated MSF magnitude and angle graphs shown in Figure 2.19 can now be compared with the measured data in Figure 2.24. There is a strong correspondence

between the measured and simulated stray close-field angle. The measured angle changes fairly linearly with rotor position and can therefore be used to measure the rotor electrical angle. The measured MSF magnitude is, however, different from one electrical rotation to the next as shown in Figure 2.24. This is possibly due to magnet strength and motor manufacturing tolerances. These measurements therefore show that the MSF magnitudes cannot be used to identify the initial angle region as were proposed earlier in this chapter. This in turn means that only the close-field angle could be used to construct a relative rotor position sensor, not an absolute position sensor as is required in this project.

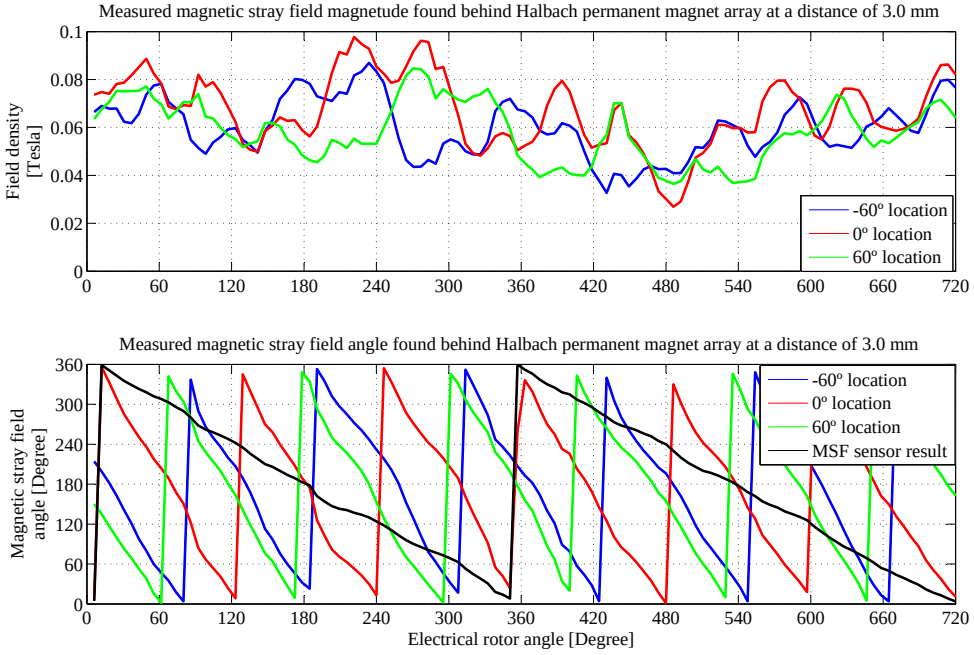

Figure 2.24: Measured magnetic stray close-field angles and magnitudes at the three sensor blocks for two electrical rotations

2.6 Rotor position from far-field measurements

2.6.1 Sensor placement

Figure 2.25 shows the simulated MSF angle and magnitude for one electrical angle rotation at a distance of 15.6 mm behind the Halbach permanent magnet array. The magnetic stray far-field angle completes one rotation for every electrical angle rotation as shown in Figure 2.25. This in itself means that the magnetic stray far-field angle alone can be used to construct an absolute electrical-angle rotor position sensor. However, the downside is at this distance the field strength and therefore the signal-to-noise ratio is significantly

less than in the close-field region. Figure 2.25 shows that a maximum field strength of 3.8 mT could be expected at this distance. Since the MSF-sensor has a resolution of 41 µT, accurate rotor angle measurement can be made even at this distance.

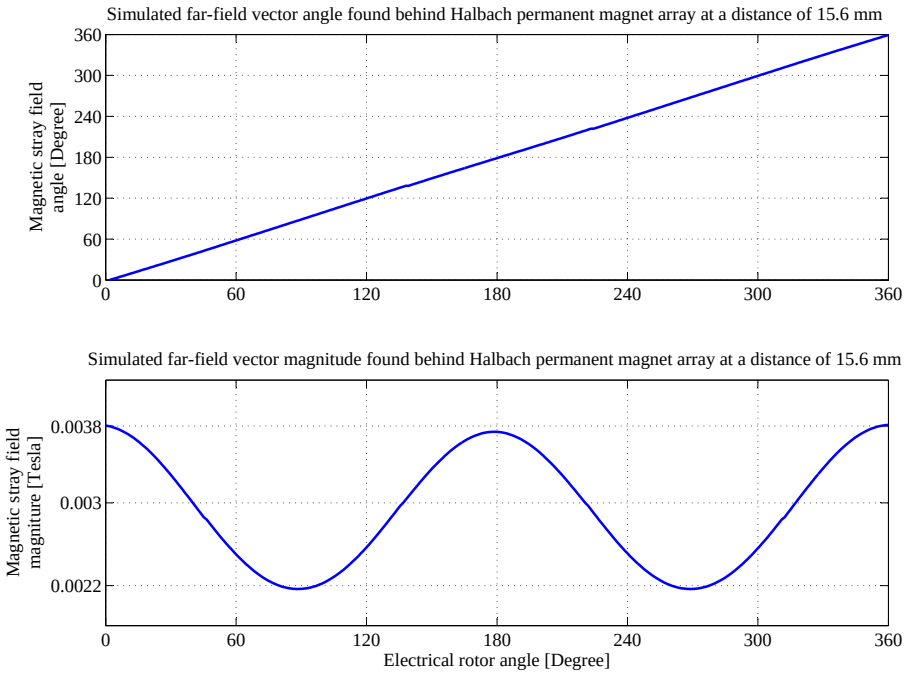

Figure 2.25: Simulated MSF vector angle and magnitude at the centre sensor location for one electrical angle rotation at a distance of 15.6 mm behind the Halbach permanent magnet array

Only one sensor block positioned at the 0° electrical angle is used to measure the magnetic stray far-field angle as shown in Figure 2.26. As in the case of the close-field measurement, the sensor block consists of two orthogonally positioned SS496A1 linear Hall sensors, one facing the tangential and one facing the radial direction.

2.6.2 Hardware development of MSF-sensor version 2.0

The available space inside the third IDRFPMSM is significantly less than in its predecessor. As a result the MSF-sensor was redesigned to a smaller packaging as shown in Figure 2.27.

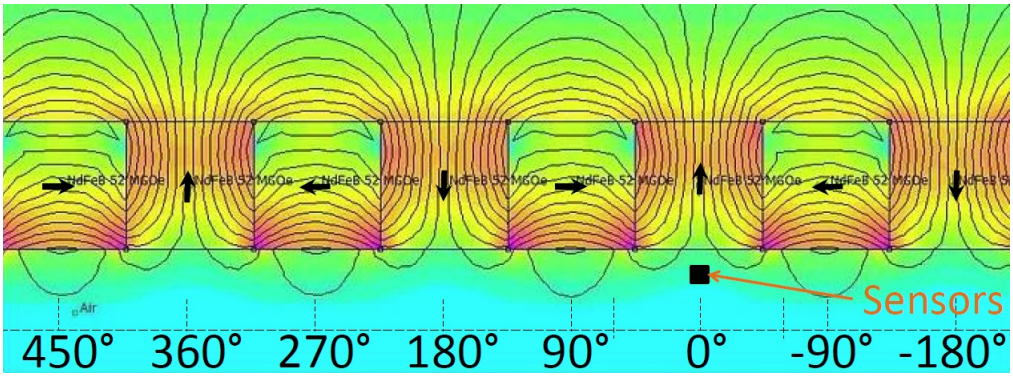

Figure 2.26: Magnetic stray far-field sensor placement behind Halbach permanent magnet array

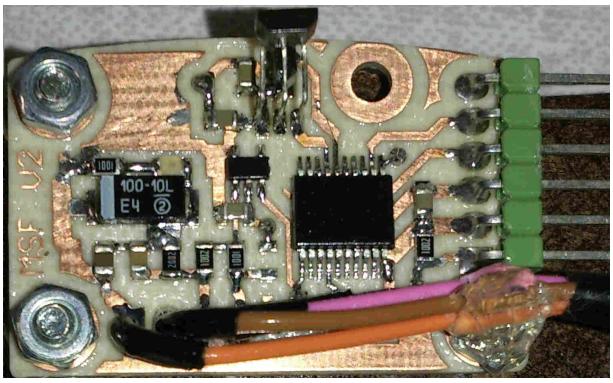

Figure 2.27: Second MSF-sensor PCB

Figure 2.28 shows the component interaction block diagram of the redesigned MSF-sensor. Since the MSF angle need only be measured in one location when using the far-field region for rotor position identification, the sensor blocks have been reduced to a single sensor block consisting of a radial and tangential linear Hall sensor.

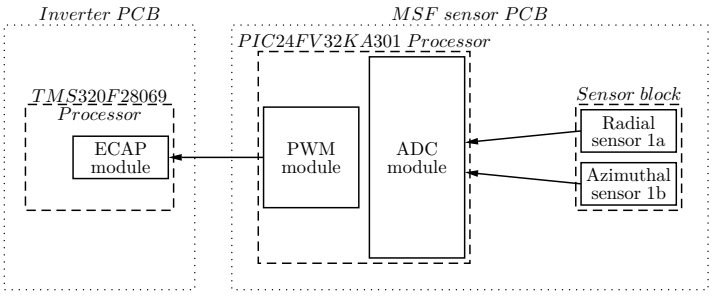

Figure 2.28: Second MSF-sensor's component interaction block diagram

Figure 2.29 shows the firmware flow diagram of the second MSF-sensor. At initial power-

on the 60 MHz internal oscillator, 1 msec internal interrupt timer, two 12-bit ADC modules, a 10-bit 10 kHz PWM module and the applicable input-output pins are configured. Once an interrupt is triggered, only two analogue Hall sensor output pins are measured with the ADC module of the microcontroller. These two sensor outputs are used to calculate the MSF angle. The electrical rotor angle is now calculated by removing the constant error from the magnetic stray far-field angle. The MSF-sensor output is delivered as a varying duty-cycle on a 10 kHz PWM signal.

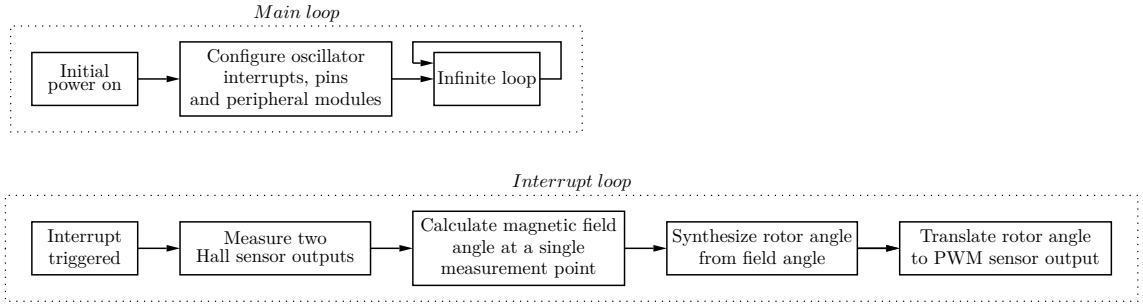

Figure 2.29: Second MSF-sensor's firmware flow diagram

2.6.3 Installing the MSF sensor onto the stator

Figure 2.30 shows an auxiliary section of the IDRFPMSM with MSF sensor installed. In this chapter the magnetic stray-field at different distances behind the Halbach permanent magnet array are investigated. For this experiment the MSF sensor needs to be able to move closer to and further away from the magnet array as required. A motorised sliding table was developed that allows the user to move the MSF sensor closer to or further away from the magnet array from outside the assembled machine as required. Figure 2.30 shows the MSF sensor and motorised sliding table installed directly onto the stator. The IDRFPMSM rotor has a web that prevents the machine from being assembled with an extended MSF sensor. The machine is therefore assembled with a retracted sliding table and only extended after assembly as shown by the blue dots in Figure 2.30.

Figure 2.31 shows the MSF sensor and motorised sliding table installed onto the stator with the MSF sensor fully retracted in (a) and fully extended in (b). The MSF sensor is retracted to the position in (a) before machine assembly. After assembly the sensor is extended to the required position.

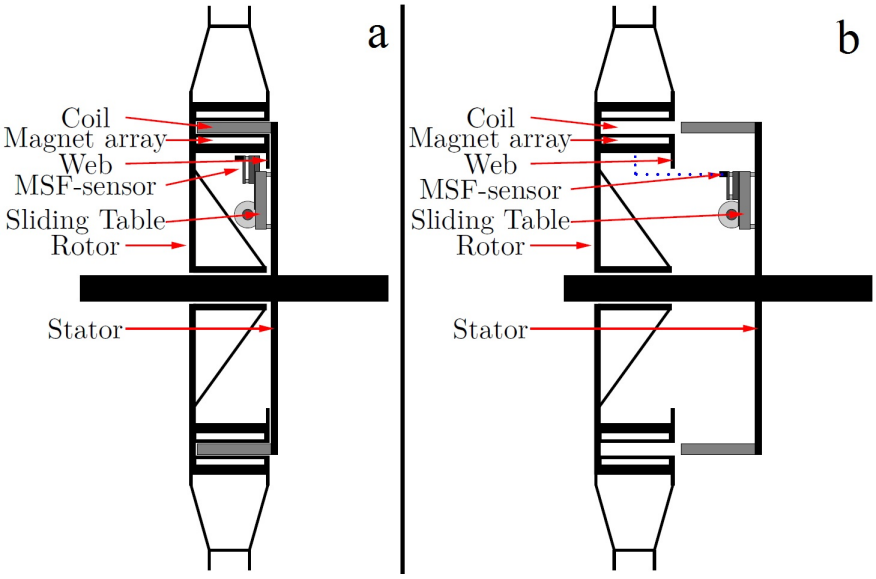

Figure 2.30: Auxiliary section of IDRFPMSM with MSF sensor

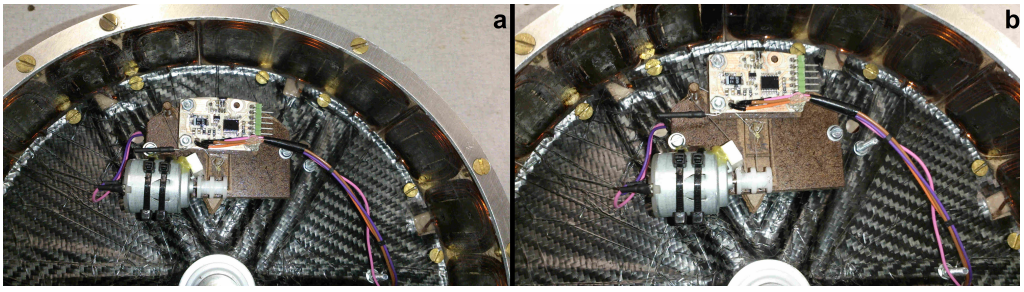

Figure 2.31: MSF-sensor and motorised sliding table installed onto the stator with the MSF-sensor fully retracted in (a) and fully extended in (b)

2.7 MSF sensor measurement results

Figure 2.32 shows the electrical rotor angle results measured with the MSF sensors. The horizontal axes show the actual electrical rotor angle and the vertical axes show the electrical rotor angle measured with the MSF sensors. The top graph shows the electrical rotor angle measurement with the magnetic stray far-field in its linear region. Please take note of the measurement ripple due to the low signal-to-noise ratio of the weak magnetic stray fields at this distance from the magnet array. Since the magnetic stray far-field completes one rotation for every electrical angle rotation, the electrical angle is the same as the magnetic stray far-field angle. The middle graph shows the electrical rotor angle measurement with the magnetic stray far-fields in its non-linear region.

The magnetic stray close-field, however, completes three rotations for every electrical

angle rotation as shown in the bottom red graph in Figure 2.32. The relative electrical rotor angle is in turn calculated from the magnetic stray close-field angle as shown in the bottom blue graph in Figure 2.32. The bottom graph shows that even though the magnetic stray close-field angle has significant non-linearities, the three times scaling factor of this calculation makes the electrical rotor angle calculated from the magnetic stray close-fields quite usable.

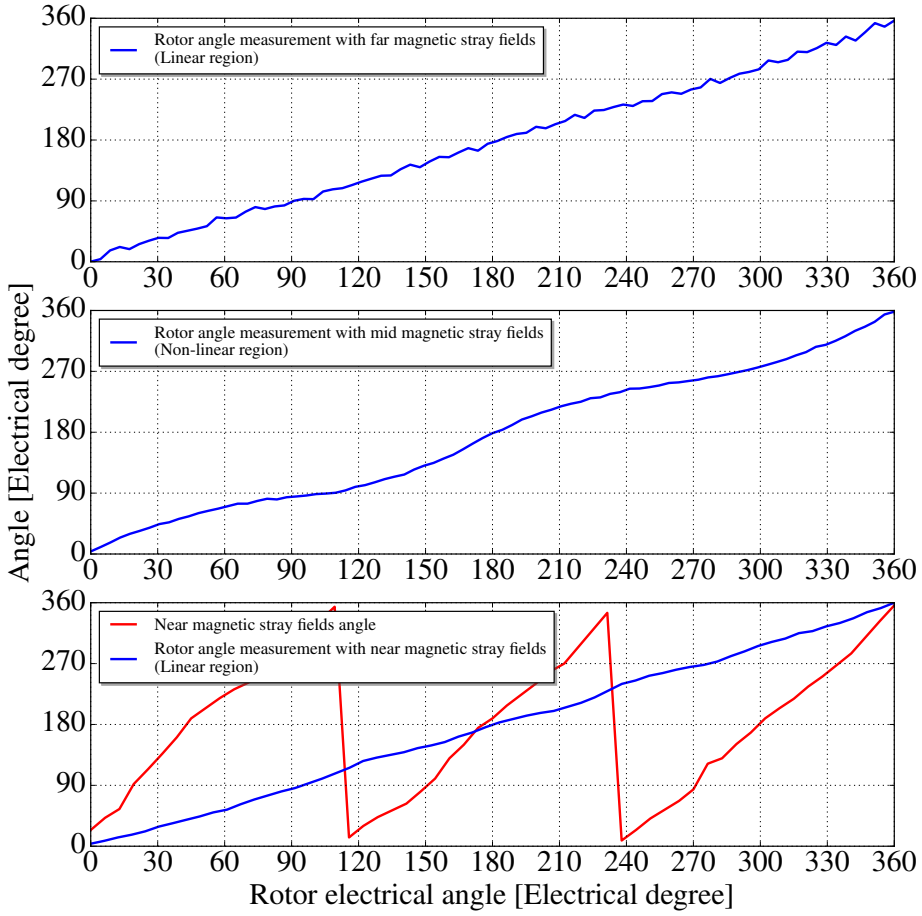

Figure 2.32: Rotor angle measured with MSF sensors

The red graph in Figure 2.33 shows the electrical rotor angle calculated from the magnetic stray close-fields and the blue graph shows the electrical rotor angle measured with the magnetic stray far-fields. Figure 2.34 shows the electrical rotor angle measurement error with the close-fields in red and the far-fields in blue. These two graphs show that the electrical rotor angle calculated from the magnetic stray close-fields has an angle error of

about ±5° electrical due to non-linearities and with the magnetic stray far-fields has an angle error of about ±15° electrical due to measurement noise and non-linearities.

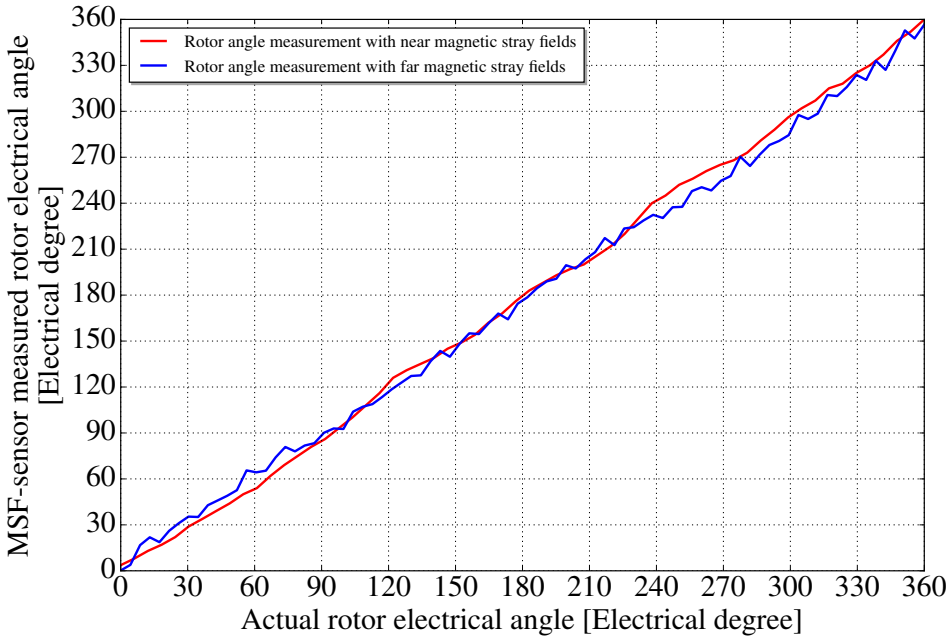

Figure 2.33: MSF sensor accuracy on close and far-field measurements

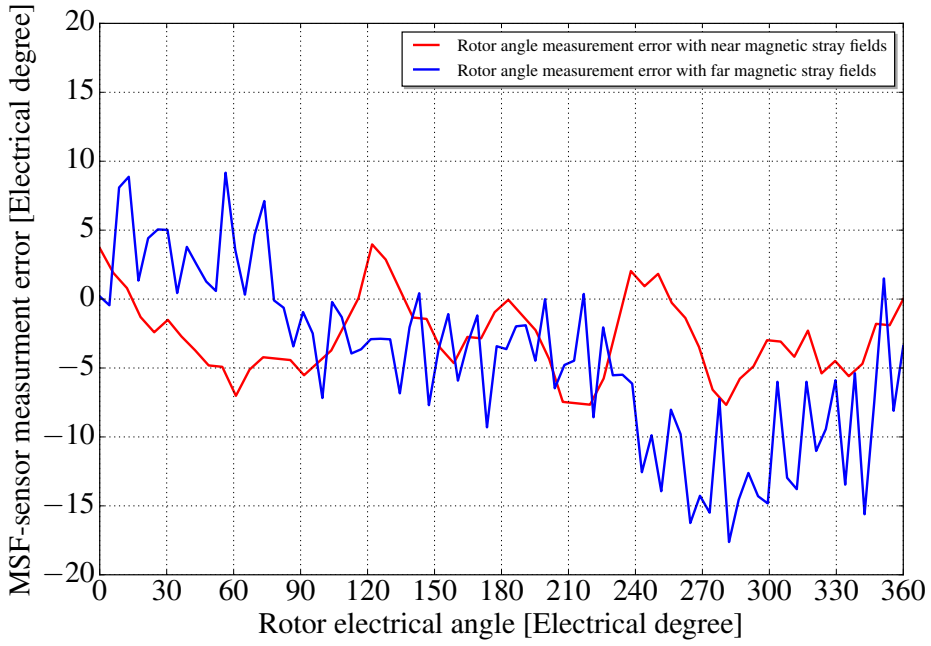

Figure 2.34: MSF sensor close and far-field measurement error

2.8 Chapter conclusion

This chapter investigates using the magnetic stray fields behind the Halbach permanent magnet array of an IDRFPMSM for rotor-position estimation. A simulation identified two potential sensor placement locations. Since the magnetic stray field angle in the close-field region completes three rotations for every electrical angle rotation, it was attempted to use the magnet stray-field relative magnitudes as well as angles in three measurement locations. Practical measurements soon revealed the relative magnitudes are unreliable due to magnet strength and machine manufacture tolerances. As a result the magnetic stray close-fields could only be used to construct a relative electrical rotor angle sensor. The magnetic stray far-field was successfully used to construct an absolute electrical angle sensor as the magnetic stray far-fields complete one rotation for every electrical angle rotation.

Comparison of the final measurement results revealed that the electrical rotor angle calculated with the close-field angle has higher accuracy that that calculated with the far-field angle. The accuracy can be improved by using both the close-fields and the far-fields in the electrical rotor angle estimation. Using an observer or system-state-estimator should improve the measurement linearity significantly as well.

Chapter 3

Automatic PMSM parameter measurement

3.1 Chapter introduction

Accurate machine parameters are essential to achieve optimum vector control. The machine parameters of many commercial PMSMs are not provided by the motor manufacturers. Even if the machine parameters are known, once the machine is installed, the moment-of-inertia and friction-coefficient change to the total driven parameters. The parameters of the assembled systems should therefore be identified before closed-loop operation is attempted. Many system-identification technologies exist, including model reference adaptive systems, recursive least square algorithms, Kalman filters, artificial neural networks and evolutionary algorithms [16]. These technologies all use the phase currents, terminal-voltage measurements and rotor-position measurements to estimate the system parameters.

3.2 Chapter outline

The literature study section in 3.3 introduces methods used by different authors to estimate the PMSM parameters. The machine parameters are first measured using a test-bench method to establish an accurate baseline in 3.4. Subsequently an open-loop parameter-estimation method is introduced in 3.5 that serves as a sensorless alternative to the test-bench method. Closed-loop parameter estimation is thereafter introduced in 3.6 followed by the results in 3.7 and a brief conclusion in 3.8.

3.3 Literature study related to PMSM parameter estimation

3.3.1 Parameter estimation background

Jaganathan et al. [10] used an unsupervised learning method to estimate the direct-axis and quadrature-axis stator inductance, torque and PM flux magnitude of a PMSM. Jaganathan explained that neural networks can be trained to represent complex multi-input multi-output non-linear systems, making it one of the best ways to estimate PMSM parameters. However, this method requires on-line and off-line training. Jaganathan also used simulated data for off-line training. Even though this method delivered promising results, simulated data was needed to train the system. The questions are whether this system could be used with a completely unknown machine without the simulated result being used for off-line calibration and how calculation intensive this process is.

Khov et al. [17] presented both on-line and off-line PMSM parameter-estimation method. The sinusoidal (harmonic) compositions of the PWM driving signal together with a recursive least squares method is used to estimate the stator coil resistance and stator coil inductance. The author did not indicate which harmonic was used. The author claimed that good results were recorded with a PWM switching frequency of 5 kHz. The harmonic composition of the PWM driving signal is used as excitation. This means that when a machine with low stator phase inductance is used, a PWM switching frequency of 50 kHz or higher will be required. ADC measuring and arithmetic speeds far beyond that of an average microcontroller is required. This method is therefore not ideal for microcontroller implementation.

Lee et al. [18] presented a closed-loop PMSM parameter-estimation method that makes use of PI controller gain tuning. Lee moves the controller "zero" around by changing the PI controller gain until the controller "zero" is on top of the motor "pole" and effective zero cancellation takes place. At this point the closed-loop system is reduced to and responds as a first-order system. Lee evaluates the gain tuning progress by monitoring the current. A single current loop controller was used to estimate the phase resistance, phase inductance and BEMF constant.

Makela et al. [19] used a 2D finite element analysis and differential evolution algorithm to estimate PMSM parameters. The machine was modelled using finite element analysis. A theoretical model was fitted to the resulting numerical data using a least-squares cost function. The cost function was then minimised using a differential evolution algorithm.

Rashed et al. [20] presented an indirect rotor field-oriented control scheme for a synchronous machine, that is insensitive to stator resistance mismatch. The author added a model reference adaptive system to estimate the stator resistance and rotor flux speed and magnitude. Rashed claimed that experimental results showed excellent performance.

Xiao et al. [21] used a Kalman filter to estimate rotor permanent magnet flux. Xiao explained that as the rotor's PM temperature increased, the PM residual flux density and intrinsic coercivity decreased. When the PM cools, the PM residual flux density and intrinsic coercivity returns to its original level. Should the PM temperature rise beyond its critical temperature level, demagnetisation occurs. Once demagnetisation occurs, higher current is needed to reach the required torque. This in turn could damage the machine further. Xiao prevents this with early PM demagnetisation detection.

3.3.2 Method of implementing the PMSM parameter measurement

The literature study of this chapter discusses methods used to estimate machine parameters in both open-loop and closed-loop configuration. In all of these studies three or less of the five PMSM parameters were estimated. It is worth mentioning that all five parameters are required for accurate closed-loop operation. Most of these methods are very calculation intensive and would therefore not be ideal for microcontroller implementation. In this study a new IDRFPMSM with unknown parameters is used. A test-bench parameter measurement method was developed to measure the machine parameters. This provides a baseline with which to compare the results of the automatic parameter-measurement system. This chapter then presents an alternative sensorless open-loop and closed-loop method for machine parameter measurement. It is assumed that the machine being used has unknown parameters. At power-on the system therefore first identifies the machine parameters with an open-loop test and then updates the machine parameters during the closed-loop operation.

3.4 Test-bench PMSM parameter measurement

3.4.1 Overview

The machine parameters are measured with a test-bench setup to establish an accurate baseline reference. The mathematical model of a PMSM is described by [2]:

$$\begin{aligned} V_d &= Ri_d + L_d\frac{di_d}{dt} - \omega_e L_q i_q \\ V_q &= Ri_d + L_q\frac{di_q}{dt} + \omega_e L_d i_d + \omega_e \lambda_m \\ T_m &= \frac{3}{2}P\left(\lambda_m i_q + (L_d - L_q)i_d i_q\right) \\ \frac{d\omega_e}{dt} &= \frac{P}{J}T_m - \frac{B}{J}\omega_e \end{aligned} \tag{3.1}$$

It should be noted that the connection between BEMF constant K_e and rotor flux magnitude λ_m is: K_e=Pλ_m where P is the amount of pole pairs. Since this is a non-salient machine, $L_q = L_d$ = L. There are five parameters that need to be measured: the phase resistance R, phase inductance L, BEMF constant K_e, friction coefficient B_f and moment of inertia J.

3.4.2 Bench measurement of phase resistance and phase inductance

The phase resistance and phase inductance are measured with a precision LCR meter between a single phase terminal and the neutral terminal while the rotor is at standstill as shown in Figure 3.1. Since this is a balanced three phase load, the phase resistance and phase inductance respectively of all three phases are identical.

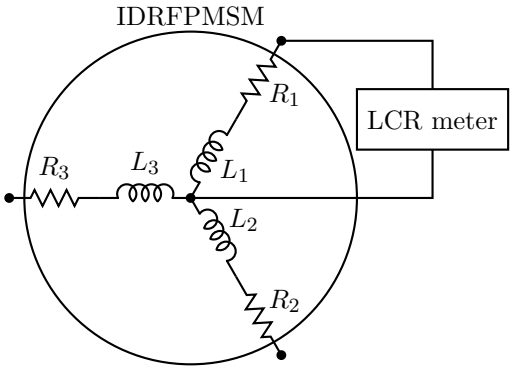

Figure 3.1: Bench phase resistance and phase inductance measurement setup

3.4.3 Bench measurement of BEMF-constant

The BEMF-constant K_e is measured by spinning the IDRFPMSM rotor at a constant speed with an electric drill and measuring the generated sinusoidal waveform (BEMF) between the phase terminal and the neutral terminal as shown in Figure 3.2.

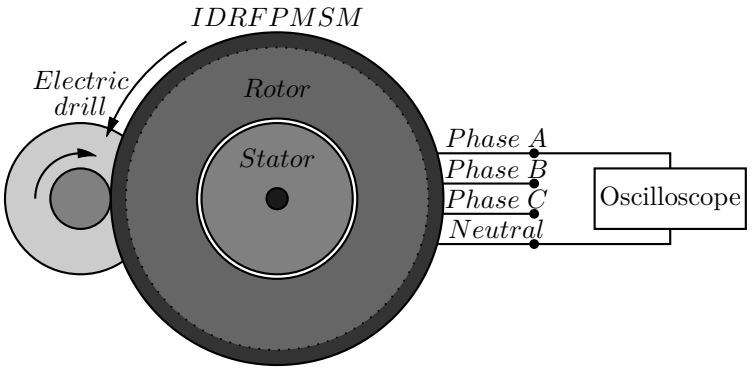

Figure 3.2: BEMF measurement setup

The BEMF constant K_e is calculated by:

$$K_e = \frac{V_{positive\_peak} P}{2\pi f_{generated}} \tag{3.2}$$

Where $V_{positive\_peak}$ is the peak phase-to-neutral voltage, P is the number of pole pairs and $f_{generated}$ is the electric frequency obtained from the sinusoidal period $T_{generated}$.

3.4.4 Bench measurement of friction-coefficient and moment-of-inertia

Since the friction coefficient of this machine is fairly small, a pendulum test is used to identify the mechanical parameters of the machine. Figure 3.3 shows the measurement setup used.

A weight with a known mass m_2 is attached to the wheel rotor at distance l from the axle centre as show in Figure 3.3. The total moment-of-inertia now consists of the unknown moment-of-inertia of the rotor J_1 and the known moment-of-inertia of the added weight J_2 as described in:

$$J_{total} = J_1 + J_2 = J_1 + m_2 l^2 \tag{3.3}$$

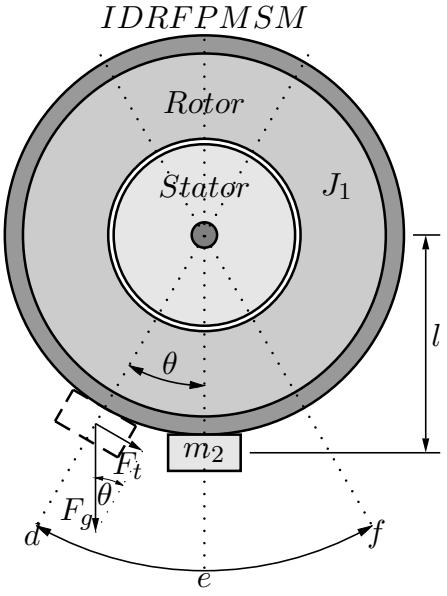

Figure 3.3: Pendulum test setup

The tangential force F_t of the weight m_2 being displaced from its position of rest by angle $\theta_t$is:

$$F_t = m_2 g sin\theta_m \tag{3.4}$$

Where g is gravitational acceleration of $9.81\frac{m}{sec^2}$. This tangential force F_t at distance l from the centre creates a torque $T_{tangential}$ described by:

$$T_{tangential} = F_t l = m_2 g l sin\theta_m \tag{3.5}$$

Friction dampening is described by:

$$T_{friction} = B_f \omega_m = B_f \dot{\theta}_m \tag{3.6}$$

Where $T_{friction}$ is the friction torque, B_f is the friction coefficient and ω_m (or $\dot{\theta}_m$) is the mechanical angular speed.

A second-order differential equation is written to represent the system:

$$(J_1 + m_2 l^2)\ddot{\theta}_m = -m_2 g l sin\theta_m - B_f \dot{\theta}_m \tag{3.7}$$

This second-order differential equation is now linearised by assuming $sin\theta_m \approx \theta_m$ for small angles of θ_m, therefore:

$$(J_1 + m_2 l^2)\ddot{\theta}_m = -m_2 g l \theta_m - B_f \dot{\theta}_m \tag{3.8}$$

The linearised second-order differential equation is now rearranged to:

$$\ddot{\theta}_m + \frac{B_f}{J_1 + m_2 l^2}\dot{\theta_m} + \frac{m_2 g l}{J_1 + m_2 l^2}\theta_m = \ddot{\theta}_m + 2\zeta\omega_n\dot{\theta}_m + \omega_n^2\theta_m = 0 \tag{3.9}$$

where ω_n is the natural angular frequency and ζ is the damping ratio. The moment of inertia of the rotor is calculated with:

$$\omega_n^2 = \frac{m_2 g l}{J_1 + m_2 l^2} \tag{3.10}$$

$$J_1 = \frac{m_2 g l}{\omega_n^2} - m_2 l^2 \tag{3.11}$$

The machine's friction coefficient is calculated with:

$$2\zeta\omega_n = \frac{B_f}{J_1 + m_2 l^2} \tag{3.12}$$

$$B_f = 2\zeta\omega_n(J_1 + m_2 l^2) \tag{3.13}$$

During rest, weight m_2 is at position e (Figure 3.3). An impulse is applied by pulling weight m_2 to position d and released. The rotor now oscillates between positions d and f with declining amplitude as shown in Figure 3.4. The impulse response of a second-order system is described by:

$$y(t) = ke^{-\sigma t}sin(\omega_d t) \tag{3.14}$$

Where $y(t)$ is the mechanical rotor angle, k is a gain constant, t is time in seconds and σ and ω_d are the real and imaginary components of the second-order complex poles. Two sets of measurements, mechanical rotor angle $(y(t_1; y(t_2)))$ at time $(t_1; t_2)$ are measured at the turning points at position d, one period apart as shown in Figure 3.4.

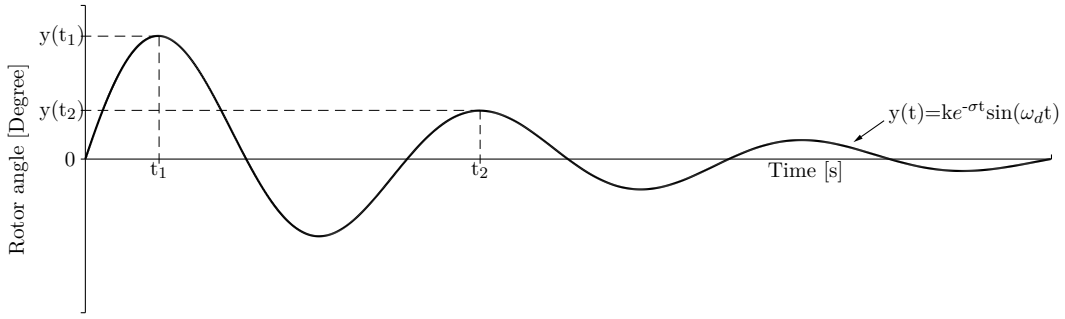

Figure 3.4: Rotor angle oscillation during pendulum impulse-response test

At the turning points at time t_1 and t_2, $sin(\omega_d t_{1or2}) = 1$, therefore from (3.14):

$$y(t_1) = ke^{-\sigma t_1} sin(\omega_d t_1) = ke^{-\sigma t_1}.1 = ke^{-\sigma t_1} \tag{3.15}$$

$$y(t_2) = ke^{-\sigma t_2} sin(\omega_d t_2) = ke^{-\sigma t_2}.1 = ke^{-\sigma t_2} \tag{3.16}$$

Constant k is eliminated by division:

$$\frac{y(t_1)}{y(t_2)} = \frac{ke^{-\sigma t_1}}{ke^{-\sigma t_2}} = e^{-\sigma(t_1 - t_2)} = e^{\sigma(t_2 - t_1)} \tag{3.17}$$

And rewritten to:

$$\sigma = \frac{1}{t_2 - t_1} ln\left(\frac{y(t_1)}{y(t_2)}\right) \tag{3.18}$$

The pendulum completes a full oscillation of 2π radians in between time t_1 and t_2 therefore from (3.14):

$$\omega_d(t_2 - t_1) = 2\pi \tag{3.19}$$

$$\omega_d = \frac{2\pi}{(t_2 - t_1)} \tag{3.20}$$

Now the natural angular frequency ω_n is:

$$\omega_n = \sqrt{\omega_d^2 + \sigma^2} \tag{3.21}$$

And the damping ratio ζ is:

$$\zeta = \frac{\sigma}{\omega_n} \tag{3.22}$$

Lastly from (3.11) and (3.13) the moment of inertia J_1 and the friction coefficient B_f of the rotor is calculated using:

$$J_1 = \frac{m_2 g l}{\omega_n^2} - m_2 l^2 \tag{3.23}$$

$$B_f = 2\zeta\omega_n(J_1 + m_2 l^2) \tag{3.24}$$

3.5 Open-loop parameter measurement

3.5.1 Automatic PMSM parameter measurement implemented on inverter PCB

Now, let's look at the parameter measurement system implemented on the microcontroller. This study focuses primarily on PMSM wind turbine and electric vehicle applications. As the machines used in these applications warm up, the coil resistance increases and rotor PM residual flux density and intrinsic coercivity decrease [21]. As the rotational speed of the machine changes, the drag associated with mechanical friction, eddy current losses and hysteresis losses changes. In a vehicle application as extra passengers or luggage are added to or removed from the vehicle, the combined inertia and friction coefficient of the system change. Most of these changes are unpredictable or not specified by the machine manufacturer, but has a significant influence on system control performance and should be considered. An on-line parameter estimator is developed that measures the machine parameters during normal operation and updates the control system accordingly. This on-line parameter estimator is a non-intrusive observer that estimates the machine parameters by analysing the response of the machine to the controller's commands. In normal operation the parameter estimator will not issue any commands, but rather wait for certain measurement conditions to occur. Figure 3.5 shows the component interaction block diagram of the inverter. As indicated in Figure 3.5, the on-line parameter estimator (highlighted in blue) uses the rotor speed, rotor acceleration and dq-axis machine voltage and current to estimate the parameters of the machine.

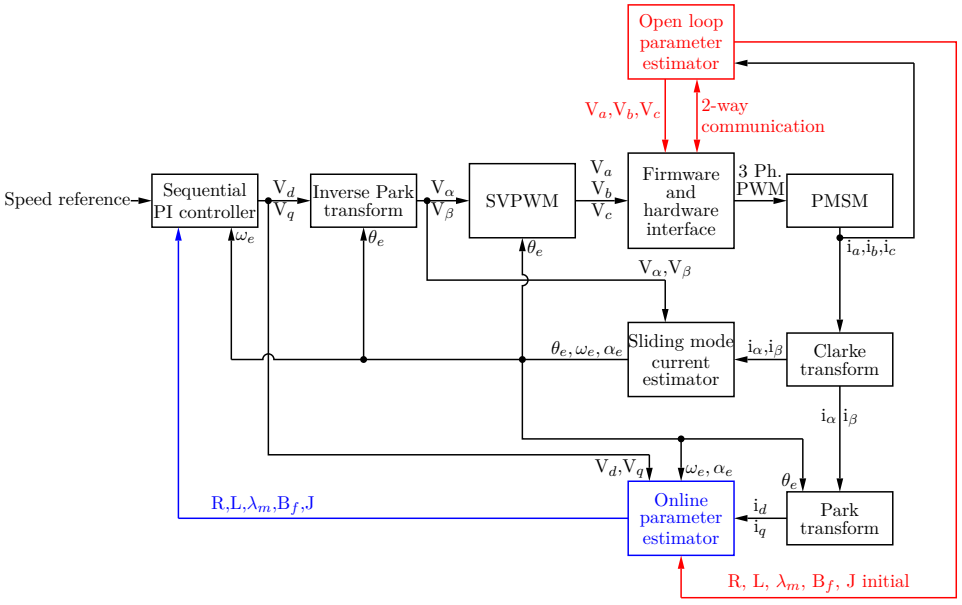

Figure 3.5: System component interaction block diagram

The on-line parameter estimator operates during closed-loop operation. Since stable closed-loop operation already requires a fairly accurate machine model, an open-loop test should first be performed at initial power-on to identify the machine model parameters. The open-loop parameter estimator is highlighted in red. The control system therefore start to operate with the parameters measured during the open-loop test and as the system parameters change during normal closed-loop operation, the control-loop parameters are updated accordingly.

3.5.2 Open-loop parameter measurement overview

In the open-loop test, the rotor is first aligned with the zero electrical angle. At this point the phase resistance is measured. An impulse is now applied by shifting the stator field angle from zero to $\frac{\pi}{6}$ rad electrical. The rotor now realigns with the $\frac{\pi}{6}$ rad electrical angle, oscillating around this point with the natural angular frequency ω_n of the system. The rotor moment-of-inertia J_1, friction-coefficient B_f and PM flux magnitude λ_m is measured by analysing oscillation behaviour. Once the oscillation has subsided, the phase inductance is measured.

3.5.3 Aligning rotor with zero electrical angle

At initial start-up, the rotor is aligned to zero electrical angle by forcing a current to flow into the phase A terminal and out of phase B and phase C terminals. This is done by

switching the phase B and C low-side switches and on and applying a 50 kHz PWM signal initially with a 0 % duty cycle to the phase A high-side switch, as shown in Figure 3.6. The duty cycle is increased at a rate significantly slower than the expected stator RL-time constant till a current of 1 A is flowing in phase A. The duty cycle is now kept constant at 1 A for a predefined time period. The rotor now realigns with the zero electrical stator field angle. The predefined time period is chosen long enough to allow the rotor oscillation to subside.

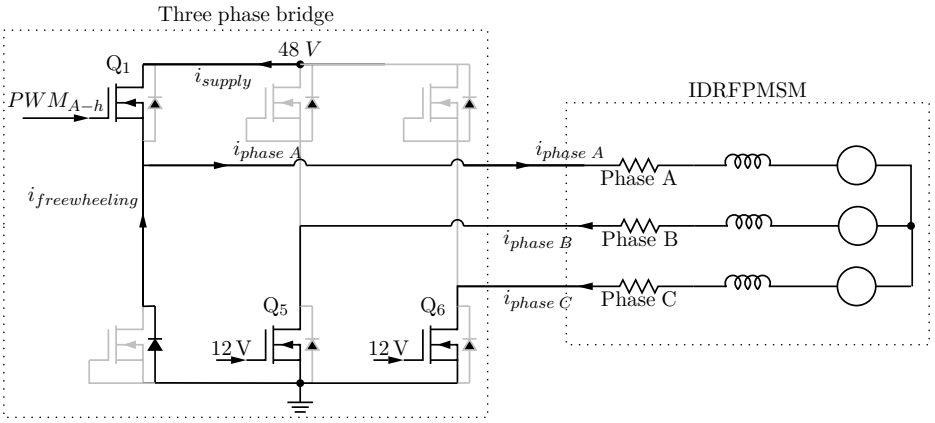

Figure 3.6: Zero rad alignment circuit

After the oscillation settled, the BEMF is zero and the phase current i_a is a DC value once again. Figure 3.7 shows the condensed electrical model with $V_{ac(avg)}$ applied between terminals a and c during rotor standstill. As shown in Figure 3.6, the average voltage drop across the coil inductance is zero. The series stator resistance $(R_a + R_b||R_c)$ is calculated from the voltage $V_{ac(avg)}$ applied between terminals A and C (or B) and phase current I_a by:

$$R_a + R_b||R_c = \frac{V_{ac(avg)}}{I_a} \tag{3.25}$$

Since the machine is a balanced three-phase load:

$$R_a = R_b = R_c = \frac{2V_{ac(avg)}}{3I_a} \tag{3.26}$$

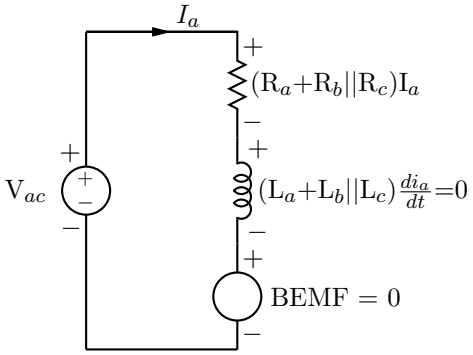

Figure 3.7: Condensed electrical model with V_{a-c} applied between terminals a and c during rotor standstill.

3.5.4 Apply impulse

Now that the rotor is aligned with the zero electrical angle, an impulse is applied by instantaneously shifting the stator field from 0 rad to $\frac{\pi}{6}$ rad electrical. This is done by switching the phase C low-side switch Q_6 on and applying a 50 kHz PWM signal with duty cycle D to the phase A high-side switch Q_1, the phase B low-side switch $Q5$ is switched off as shown in Figure 3.8. Duty cycle D is calculated so that a current of 1 A flows in phase A:

$$D = \frac{(R_a + R_b)I_a}{V_{input}} \tag{3.27}$$

The duty cycle is kept constant for a predefined time period. The rotor now realigns with the new stator field at $\frac{\pi}{6}$ rad electrical and oscillates around this point once it is reached, with natural angular frequency ω_n of the system and decaying amplitude due to friction dampening B_f.

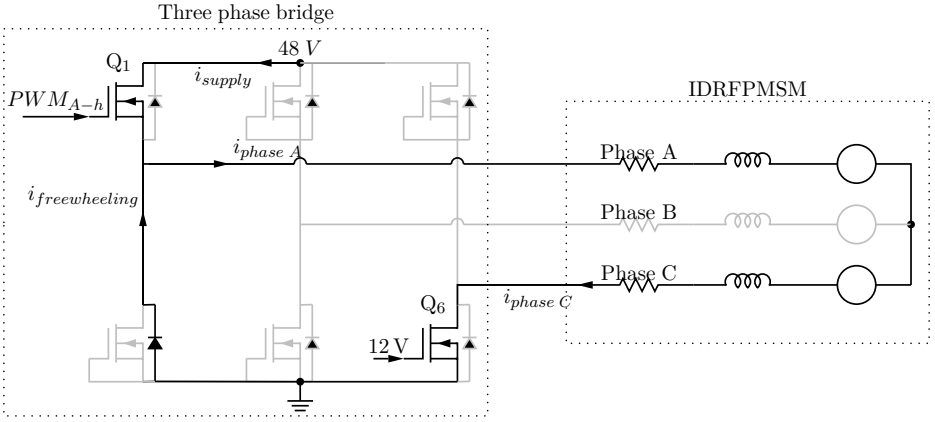

Figure 3.8: $\frac{\pi}{6}$ rad alignment circuit

Figure 3.9 shows the IDRFPMSM with force components and rotating travel path. As shown in Figure 3.9, when the rotor is aligned with the $\frac{\pi}{6}$ rad stator field at e ($\theta_e = \frac{\pi}{6}$ rad), only a direct-force component F_d is present, the magnitude of which is directly equivalent to the phase current magnitude. As the angle between rotor and stator field θ_e increases, the quadrature force component F_q increases, generating torque, and therefore an acceleration in the direction of the force F_q. This angle-dependent torque together with the moment-of-inertia and friction of the machine form a second-order system similar to the pendulum-test used earlier in this chapter. As the impulse is effectively applied in the negative angle direction and the stator field is positioned at $\frac{\pi}{6}$ rad, the angular path of the rotor is described by:

$$\theta_e(t) = ke^{-\sigma t} sin(\omega_d t + \frac{3\pi}{2}) + \frac{\pi}{6} \tag{3.28}$$

Where $\theta_e(t)$ is the electrical rotor angle, k is the angle constant, t is time in seconds and σ and ω_d are the real and imaginary components of the second-order complex poles of the system. Figure 3.9 shows the angular travel path of the rotor with an impulse applied by shifting the stator field from zero rad to $\frac{\pi}{6}$ rad (position d to position e), followed by 1.5 oscillations (positions d to e to f to e to g to e to h to e).

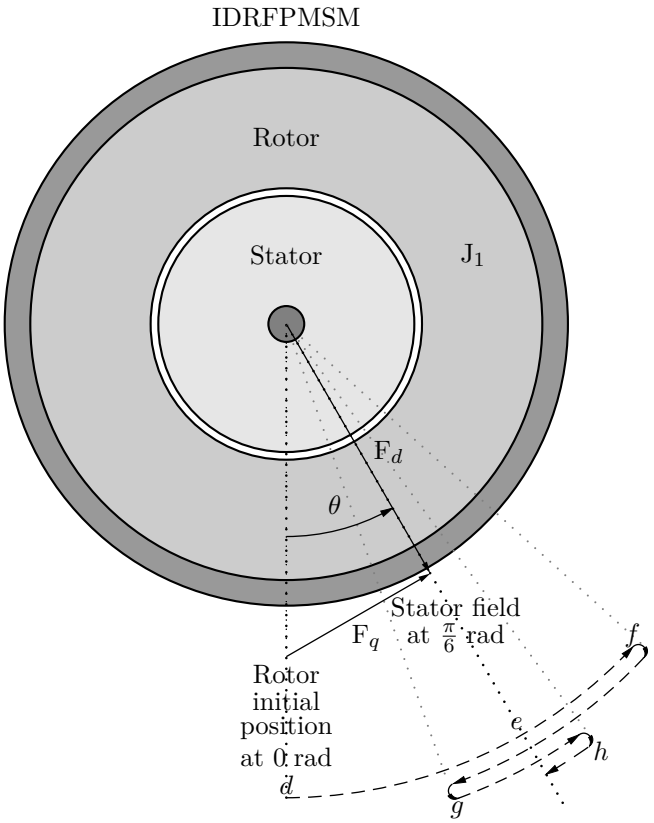

Figure 3.9: IDRFPMSM impulse-test angular travel path

The angular velocity of the rotor is calculated from (3.28) by:

$$\omega_e(t) = \frac{d\theta_e(t)}{dt} = ke^{-\sigma t}(-\sigma sin(\omega_d t + \frac{3\pi}{2}) + \omega_d cos(\omega_d t + \frac{3\pi}{2})) \tag{3.29}$$

The angular position θ_e and angular velocity ω_e of the rotor are shown in blue and red traces respectively in Figure 3.10. Please take note of the corresponding labels d to h in Figure 3.9 and Figure 3.10.

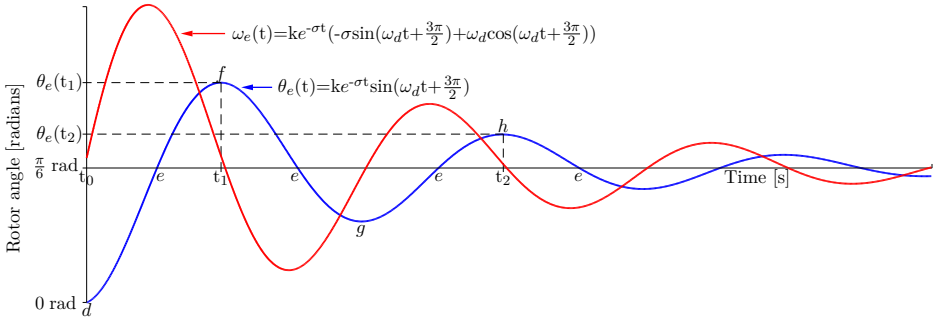

Figure 3.10: Rotor oscillation after impulse is applied

Now let's have a look at what the electrical model of the machine does during this oscillation. Figure 3.11 shows a circuit diagram of pulse-width modulated voltage source V_{a-c} connected between machine phases A and C.

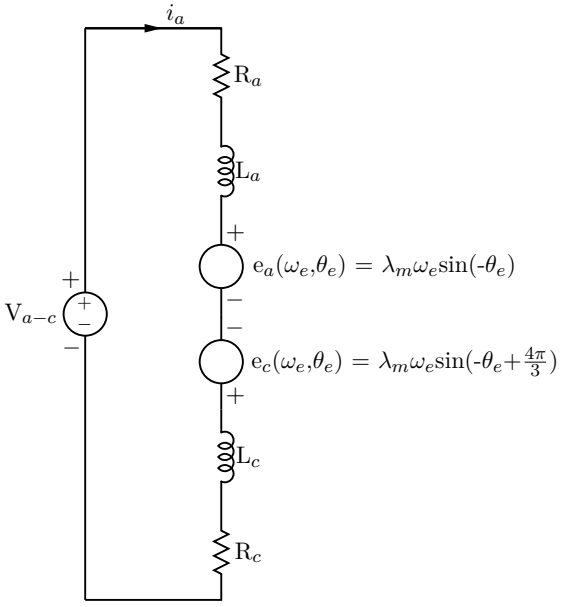

Figure 3.11: Electrical model with V_{a-c} applied between terminals a and c

The two-phase PMSM electrical model in Figure 3.11 is condensed to Figure 3.12.

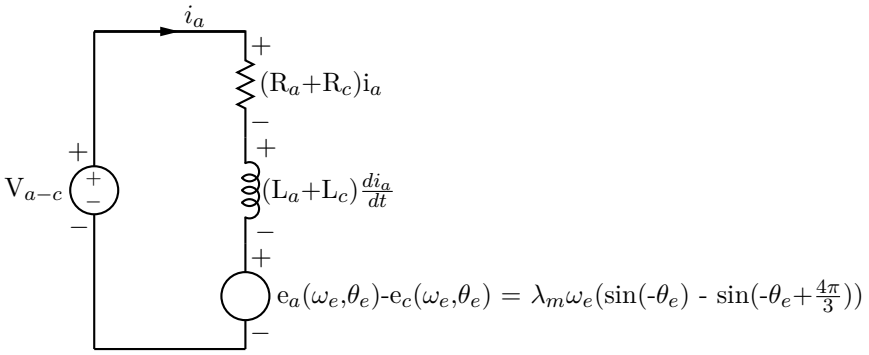

Figure 3.12: Condensed electrical model with V_{a-c} applied between terminals a and c

The voltage equation of the circuit in Figure 3.12 is:

$$V_{a-c}(t,\theta_e,\omega_e) = (R_a + R_c)i_a + (L_a + L_c)\frac{di_a}{dt} + \lambda_m\omega_e(sin(-\theta_e) - sin(-\theta_e + \frac{4\pi}{3})) \quad (3.30)$$

The PWM-switching frequency is chosen so that an acceptable current ripple is achieved for an expected coil inductance. The choice of PWM-switching frequency is discussed in the next chapter. Let us assume for this discussion that the current-ripple due to switching frequency is negligible. The system's natural frequency, which is considered in this analysis, is significantly lower than the PWM-switching frequency. Assuming that the coil inductance maintains a neglectably small phase current ripple and the source voltage V_{a-c} is a constant value. The average voltage drop across the coil inductors is zero, therefore: $(L_a + L_c)\frac{di_a}{dt} = 0$

Figure 3.13 shows the angular position θ_e and angular velocity ω_e of the rotor in the blue and red graphs respectively during this oscillation. As the rotor oscillates around the $\frac{\pi}{6}$ rad electrical stator field, BEMF voltages are developed at the stator coils. This BEMF signal is dependent on the rotor's angular velocity and the angle between the rotor and the stator field as describe by:

$$e_a(\theta_e,\omega_e) - e_c(\theta_e,\omega_e) = \lambda_m\omega_e(sin(-\theta_e) - sin(-\theta_e + \frac{4\pi}{3})) \quad (3.31)$$

The BEMF voltage signal of $(e_a(\theta_e,\omega_e) - e_c(\theta_e,\omega_e))$ is shown in the green curve in Figure 3.13. Since this generated BEMF voltage is dependent on both rotor angle and angular

velocity, every time the rotor crosses the $\frac{\pi}{6}$ rad point or the angular velocity equals zero, the BEMF voltage is zero. These BEMF zero-crossings can be utilized to sensorlessly determine rotor position. Since the source voltage V_{a-c} is kept constant, a change in BEMF voltage causes an equivalent change in phase current. Phase-A current $i_a(\theta_e, \omega_e)$ is described by:

$$i_a(\theta_e, \omega_e) = \frac{V_{a-c} - \lambda_m \omega_e (sin(-\theta_e) - sin(-\theta_e + \frac{4\pi}{3}))}{R_a + R_c} \tag{3.32}$$

As shown by the phase-A current curve $i_a(\theta_e, \omega_e)$ in Figure 3.13, the phase-A current crosses the 1 A level for the first time when the initially impulse is applied at t_0. The 1 A level is crossed for the second time when the rotor is aligned with the stator field at t_2 and for the third time when the angular velocity equals zero at t_3 with the rotor at its furthest point after its first swing.

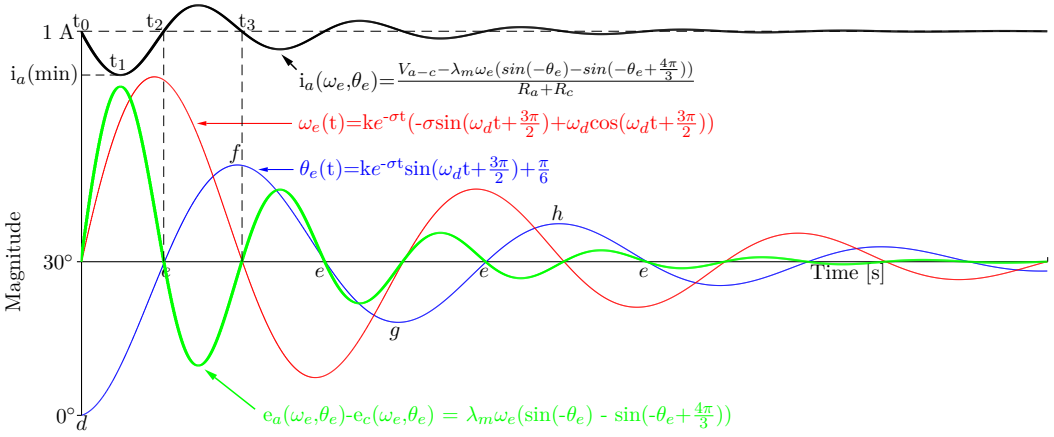

Figure 3.13: Phase current during rotor oscillation

As previously stated the stator field is instantaneously shifted from zero to $\frac{\pi}{6}$ rad-electrical at time $t = 0$. The rotor at this point in time is still positioned at zero. The angle of the rotor at $\theta_e(0)$ with reference to the $\frac{\pi}{6}$ rad electrical stator field, is $-\frac{\pi}{6}$rad electrical. The constant k is therefore calculated from (3.28) with:

$$k = \frac{-\frac{\pi}{6}}{e^{\sigma(0)} sin(\omega_d(0) + \frac{3\pi}{2})} = \frac{-\frac{\pi}{6}}{sin(\frac{3\pi}{2})} = \frac{\pi}{6} \ [rad] \tag{3.33}$$

Since the rotor angle $\theta_e(t)$ completes a quarter oscillation between time t_0 and t_2, ω_d is calculated by:

$$\omega_d = \frac{\frac{1}{2}\pi}{t_2 - t_0} \left[\frac{rad}{sec}\right] \tag{3.34}$$

Since the rotor angular velocity $\omega_e(t)$ equals zero at time t_3, σ is calculated from (3.29) by:

$$\sigma = \frac{\omega_d cos(\omega_d(t_3 - t_0) + \frac{3\pi}{2})}{sin(\omega_d(t_3 - t_0) + \frac{3\pi}{2})} \left[\frac{rad}{sec}\right] \tag{3.35}$$

The natural circular frequency ω_n is calculated with:

$$\omega_n = \sqrt{\omega_d^2 + \sigma^2} \left[\frac{rad}{sec}\right] \tag{3.36}$$

and the damping ration ζ is calculated with:

$$\zeta = \frac{\sigma}{\omega_n} \tag{3.37}$$

Now that the constants k, ω_d and σ are known, equations for the rotor position $\theta_e(t)$ and angular velocity $\omega_e(t)$ are formulated with (3.28) and (3.29) respectively. As the stator coil resistance is also known, the rotor flux magnitude λ_m is calculated with the minimum phase-current measurement at t_1 using:

$$\lambda_m = \frac{V_{a-c(avg)} - i_{a(min)}(R_a + R_c)}{\omega_e(t_1)(sin(-\theta_e(t_1)) - sin(-\theta_e(t_1) + \frac{4\pi}{3}))} \left[\frac{V.s}{rad}\right] \tag{3.38}$$

Let us define a new axis system with $\theta_{temp} = -\theta_e + \frac{\pi}{6}$. The angle relationship between these axes systems are illustrated in Figure 3.14.

The developed torque in a PMSM is described by [2]:

$$T_{dev} = \frac{3}{2}P\left(\lambda_m i_q + (L_d - L_q) i_d i_q\right) \tag{3.39}$$

As this PMSM is a non-salient machine (therefore $L_d = L_q$) and $i_q = i_a sin(-\theta_e + \frac{\pi}{6}) = i_a sin(\theta_{temp})$ therefore:

$$T_{dev} = \frac{3}{2}P\lambda_m i_a sin(\theta_{temp}) \tag{3.40}$$

With moment-of-inertia J_1 and friction-coefficient B_f, a second-order differential equation is formulated to describe the system:

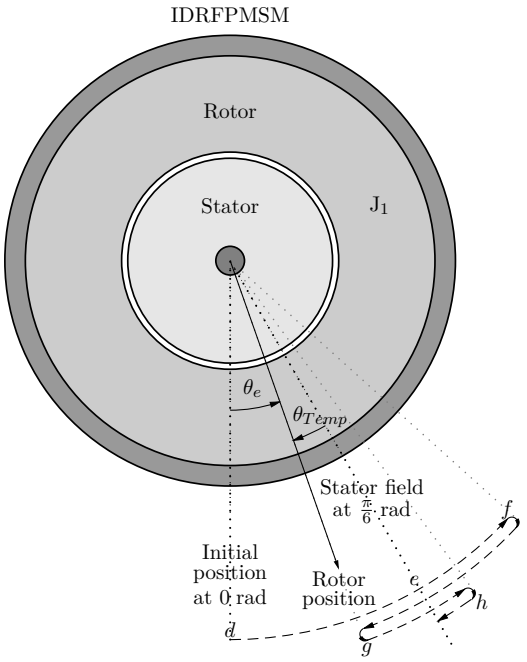

Figure 3.14: Angle relationship between two axes

$$\frac{J_1}{P}\ddot{\theta}_{temp} + \frac{B_f}{P}\dot{\theta}_{temp} + \frac{3}{2}P\lambda_m i_a sin(\theta_{temp}) = 0 \tag{3.41}$$

This second-order differential equation is now linearised by assuming $sin\theta_{temp} \approx \theta_{temp}$ for small angles of θ_{temp}, therefore:

$$\frac{J_1}{P}\ddot{\theta}_{temp} + \frac{B_f}{P}\dot{\theta}_{temp} + \frac{3}{2}P\lambda_m i_a \theta_{temp} = 0 \tag{3.42}$$

and rewritten to:

$$\ddot{\theta}_{temp} + \frac{B_f}{J_1}\dot{\theta}_{temp} + \frac{3P^2\lambda_m i_a}{2J_1}\theta_{temp} = \ddot{\theta}_{temp} + 2\zeta\omega_n\dot{\theta}_{temp} + \omega_n^2\theta_{temp} = 0 \tag{3.43}$$

Now from (3.43) the moment of inertia is calculated by:

$$J_1 = \frac{3P^2\lambda_m i_a}{2\omega_n^2} \tag{3.44}$$

and the friction coefficient is calculated by:

$$B_f = 2\zeta\omega_n J_1 \tag{3.45}$$

3.5.5 Coil inductance current discharge test

At this point, a (known) dc current is flowing through both the phase A and phase C stator coils. The stator inductances can be estimated by analysing its current discharge curve as the charged stator inductance (with unknown value) is discharged through the stator resistance (with known value). This is done by instantaneously switching the phase A high-side switch Q_1 off and switching the phase A low-side switch Q_4 on, while keeping phase C low-side switch Q_6 on. Figure 3.15 shows a circuit diagram used in the stator inductor current discharge test. Also note the current direction in Figure 3.15.

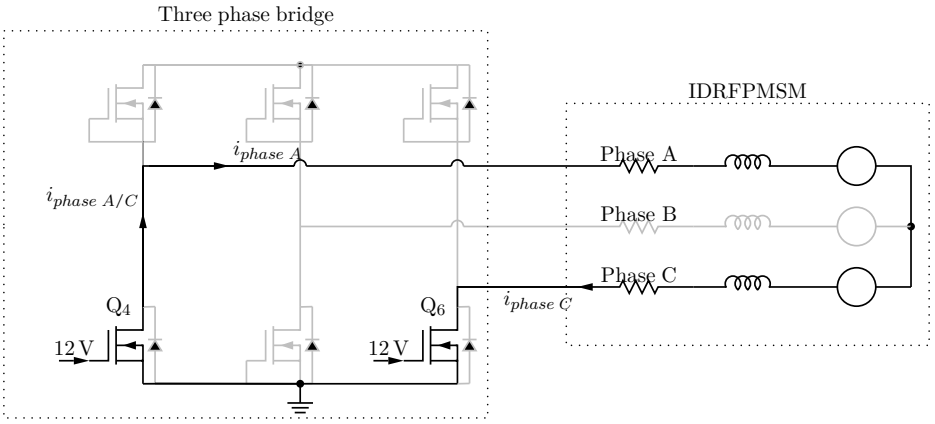

Figure 3.15: Current discharge circuit

The charged stator coil inductances will oppose the current change by inducing a voltage across the stator thereby acting as current source for a short time period. Figure 3.16 shows a graph of the current through the inductor. The current measurement i_{a4} at time t_4 is measured the instant just before the current discharge circuit is implemented. Current measurement i_{a5} at time t_5 is measured after the inductor current has decayed to 33 % of its original value after one time constant decay.

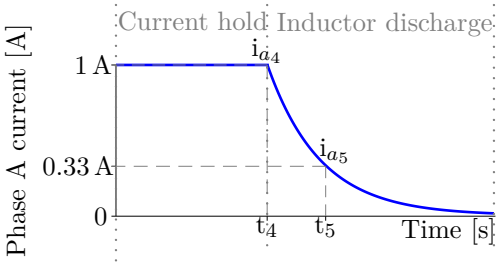

Figure 3.16: Phase A current during stator inductance discharge

Figure 3.17 shows a condensed circuit diagram of the discharge circuit. The rotor is stationary during this measurement, so the induced BEMF voltage is zero.

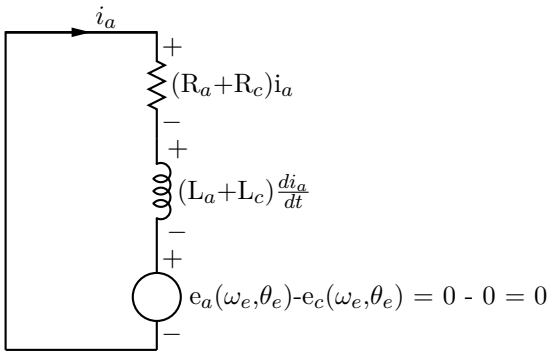

Figure 3.17: Condensed electrical model with phase A and C stator inductances discharging across stator resistances during rotor standstill

From Kirchhoff's voltage law, the discharge circuit diagram in Figure 3.17 is described by:

$$(R_a + R_c)i_a + (L_a + L_c)\frac{di_a}{dt} = 0 \tag{3.46}$$

Through integration:

$$-(R_a + R_c)\int_{t_4}^{t_5} dt = (L_a + L_c)\int_{i_{a4}}^{i_{a5}} \frac{1}{i_a} di_a \tag{3.47}$$

and rewritten in terms of series inductance as:

$$(L_a + L_c) = \frac{(R_a + R_c)(t_5 - t_4)}{ln(\frac{i_{a4}}{i_{a5}})} \tag{3.48}$$

As the PMSM is a balanced three-phase load with $R = R_a = R_b = R_c$ and $L = L_a = L_b = L_c$, 3.48 is rewritten to:

$$L = \frac{R(t_5 - t_4)}{ln(\frac{i_{a4}}{i_{a5}})} \tag{3.49}$$

As time t_5 is always measured when $i_{a5} = 0.33i_{a4}$, the inductance equation can further be simplified to:

$$L = \frac{R(t_5 - t_4)}{ln(\frac{1}{0.33})} = 0.902R(t_5 - t_4) \tag{3.50}$$

3.6 On-line (Closed-loop) parameter measurement

3.6.1 Overview

The on-line parameter estimator refines the parameters measured during the open-loop parameter measurement cycle as well as account for any parameter changes that occur during normal operation. This on-line parameter estimator is a non-intrusive observer that estimates the machine parameters by analysing the response of the machine to the commands of the controller. In normal operation, the parameter estimator will therefore not issue any commands, but rather wait for certain measurement conditions to occur. Parameters are estimated at critical points with the use of (3.51) when operating conditions cause unwanted terms to become negligible small, thereby simplifying the machine equations. Since the speed loop of the control system is optimally damped and therefore has a small overshoot, all necessary measurement conditions are encountered during rotor acceleration, deceleration or steady state operation. The PMSM parameter model is described by [2]:

$$\begin{aligned} V_d &= Ri_d + L_d\frac{di_d}{dt} - \omega_e L_q i_q \\ V_q &= Ri_d + L_q\frac{di_q}{dt} + \omega_e L_d i_d + \omega_e \lambda_m \\ T_m &= \frac{3}{2}P(\lambda_m i_q + (L_d - L_q)i_d i_q) \\ \frac{d\omega_e}{dt} &= \frac{P}{J}T_m - \frac{B}{J}\omega_e \end{aligned} \tag{3.51}$$

3.6.2 Measure rotor flux magnitude

The rotor flux magnitude λ_m is estimated during free spin when the i_d and i_q current components are zero. As the PWM switching frequency is much higher than that of the speed-loop and the average voltage-drop across an inductor is zero, the high frequency voltage ripple caused by the inductor component $L_q\frac{di_q}{dt}$ is removed by means of low pass filtering. The quadrature voltage equation $V_q = Ri_d + L_q\frac{di_q}{dt} - \omega_e L_d i_d + \omega_e \lambda_m$ is then simplified so that the rotor flux magnitude λ_m is estimated with:

$$\lambda_m = \frac{V_q}{\omega_e} \tag{3.52}$$

3.6.3 Estimate mechanical parameters

Since this is a non-salient pole machine (therefore $L_q = L_d$), the generated torque is calculated from:

$$T_m = \frac{3}{2} P \lambda_m i_q \tag{3.53}$$

The PMSM mechanical rotor model is described by: $J_1 \alpha_e = P T_m - B_f \omega_e$. The rotor electrical acceleration is described by $\alpha_e = \frac{d\omega_e}{dt}$. The friction-coefficient B_f is estimated with the mechanical model during steady state operation when $\alpha_e = 0$. The friction-coefficient is therefore calculated by:

$$B_f = \frac{P T_m}{\omega_e} \tag{3.54}$$

Once the friction-coefficient B_f is known, the moment-of-inertia is estimated during rotor acceleration or deceleration with:

$$J_1 = \frac{P T_m - B_f \omega_e}{\alpha_e} \tag{3.55}$$

3.7 Parameter measurement results

3.7.1 Test-bench parameter measurement results

A phase resistance of 0.2 Ω and a phase inductance of 143 μH are measured between a single-phase terminal and the neutral terminal with a precision LCR meter, as shown in 3.1.

During BEMF-constant measurement the rotor of the IDRFPMSM was spun at 52.2 rpm with the electric drill, as shown in Figure 3.2. The BEMF waveform generated between the neutral point and a phase terminal is shown in Figure 3.18. Figure 3.18 shows that a 5.88 Hz sinusoidal BEMF voltage curve is generated with a peak voltage of 3.68 V

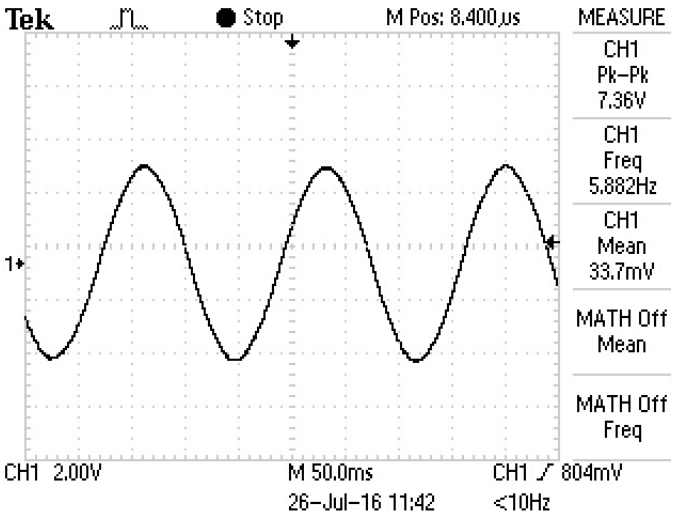

Figure 3.18: Phase-to-neutral BEMF waveform with rotor spinning at 52.2 rpm

The BEMF constant K_e is calculated by:

$$K_e = \frac{V_{positive\_peak} P}{2\pi f_{generated}} = 0.7964 \, \frac{V.sec}{rad} \tag{3.56}$$

During mechanical parameter measurement a weight of 110 g was attached to the outside of the machine rotor as shown in Figure 3.19.

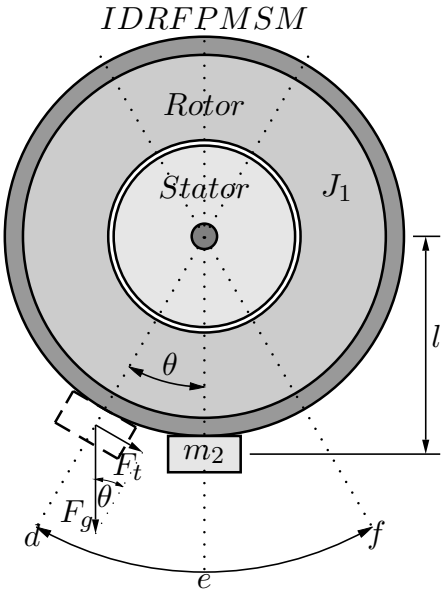

Figure 3.19: Pendulum test setup

An impulse was applied by pulling the weight to an angle of θ_m =77.1° and released. The rotor oscillated with decaying amplitude, as shown in 3.20.

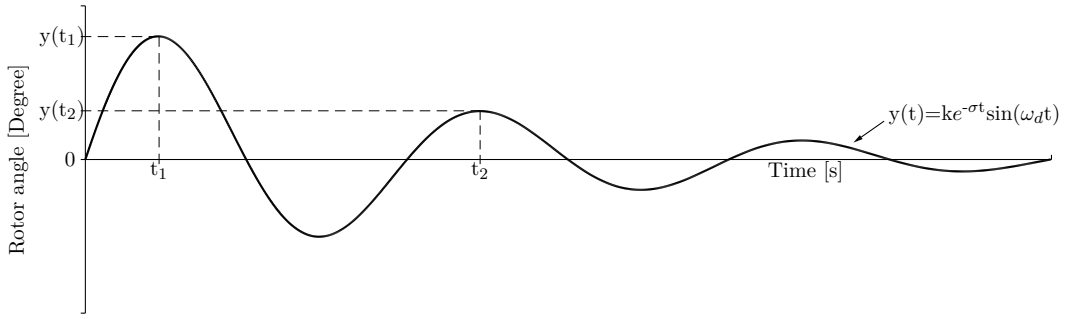

Figure 3.20: Rotor-angle oscillation during pendulum impulse-response test

The rotor was released at time t_1. At time t_2 the rotor completed a full oscillation. The rotor angle and time measurements are shown in Table 3.1.

Table 3.1: Time and rotor-angle measurements of a full oscillation period

t_1	t_2	$y(t_1)$	$y(t_2)$
0 sec	4.55 sec	77.14 ° mechanical	48.7 ° mechanical

The complex components σ and ω_d are calculated with the measurements in Table 3.1 as:

$$\sigma = \frac{1}{t_2 - t_1} ln\left(\frac{y(t_1)}{y(t_2)}\right) = 0.134 \frac{rad}{sec} \tag{3.57}$$

and

$$\omega_d = \frac{2\pi}{(t_2 - t_1)} = 1.381 \frac{rad}{sec} \tag{3.58}$$

The natural angular frequency ω_n is:

$$\omega_n = \sqrt{\omega_d^2 + \sigma^2} = 1.387 \frac{rad}{sec} \tag{3.59}$$

and the damping ratio ζ is:

$$\zeta = \frac{\sigma}{\omega_n} = 0.0967 \tag{3.60}$$

The moment-of-inertia was calculated with:

$$J_1 = \frac{m_2 g l}{\omega_n^2} - m_2 l^2 = 0.1396 \, \frac{N.m.sec^2}{rad} \tag{3.61}$$

and friction-coefficient with:

$$B_f = 2\zeta\omega_n(J_1 + m_2 l^2) = 0.0395 \, \frac{N.m.sec}{rad} \tag{3.62}$$

3.7.2 Open-loop parameter measurement results

Now let us take a step back and see the forest from the trees and recap all the steps taken during the open-loop parameter-estimation method. The open-loop parameter measurement cycle was performed at inverter power-on. Figure 3.23 shows the phase-A current measurement graph of the entire open-loop parameter measurement cycle. As shown in Figure 3.21, at time $t = 0$, phase B and C low-side switches Q_5 and Q_6 are switched on and a 50 kHz PWM signal with an initial 0 % duty cycle is applied to the phase A high-side switch Q_1. The duty cycle is linearly increased till a current of 1 A flows in phase A. The voltage magnitude at $V_{ac(avg)}$ is kept constant for 1.25 seconds to allow the rotor to move to the zero position and any oscillation to subside. The stator coil resistance is calculated by 3.63 with the applied average voltage $V_{ac(avg)}$ and the resultant phase current I_a.

$$R_a = R_b = R_c = \frac{2V_{ac(avg)}}{3I_a} = 0.226\,\Omega \tag{3.63}$$

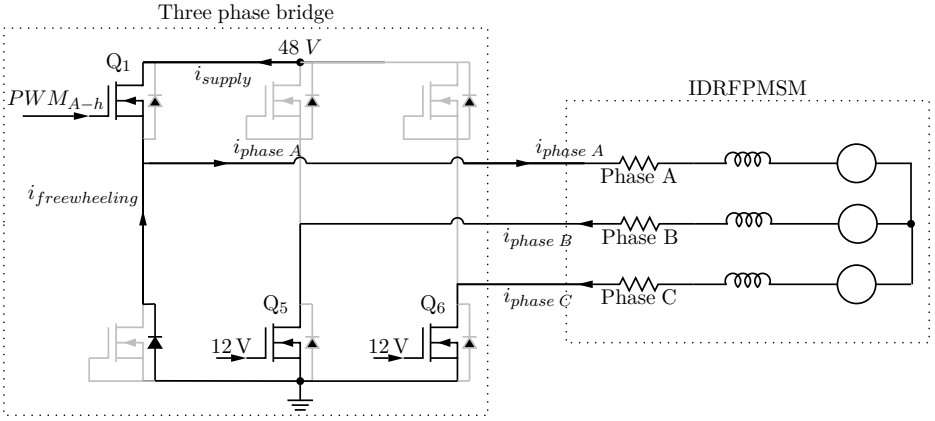

Figure 3.21: Zero rad alignment circuit

An impulse is now applied by instantaneously shifting the stator field from zero to $\frac{\pi}{6}$ rad. This is done by switching the phase C low-side switch Q_6 on and applying a 50 kHz PWM signal with duty cycle D to the phase A high-side switch Q_1 , the phase B low-side switch Q_5 is switched off as shown in Figure 3.64. Duty cycle D is calculated so that a current of 1 A flows in phase A:

$$D = \frac{(R_a + R_b)I_a}{V_{input}} = 0.0094 \tag{3.64}$$

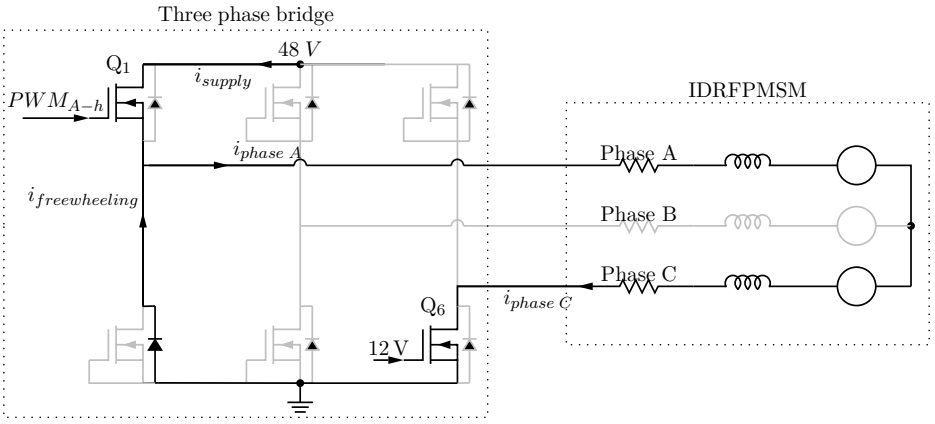

Figure 3.22: $\frac{\pi}{6}$ rad alignment circuit

Once the impulse is applied, the rotor oscillates around the $\frac{\pi}{6}$ rad stator field with decaying amplitude. Figure 3.23 shows the resultant phase A current oscillation with a dc voltage source connected between the phase A and C terminals of a machine with oscillating rotor and therefore oscillating BEMF voltage. After the rotor oscillation subsides at 6.24 seconds, the stator inductance is measured with the inductance discharge test.

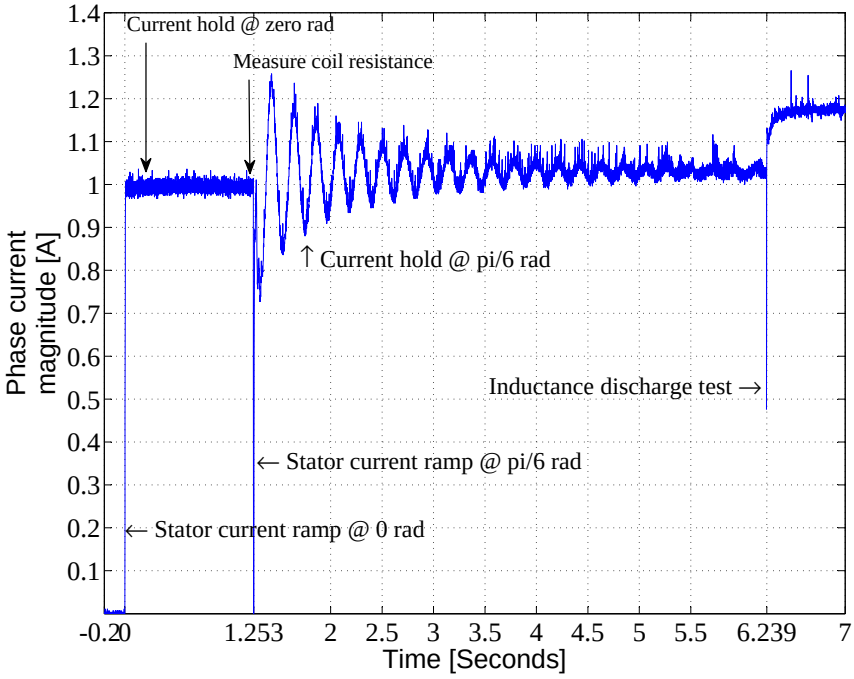

Figure 3.23: Measured phase-A current during entire open-loop parameter measurement cycle

Figure 3.24 shows an enlarged view of the phase A current oscillation. Please take note of indicated measuring points t_0, t_1, t_2 and t_3 in Figure 3.24.

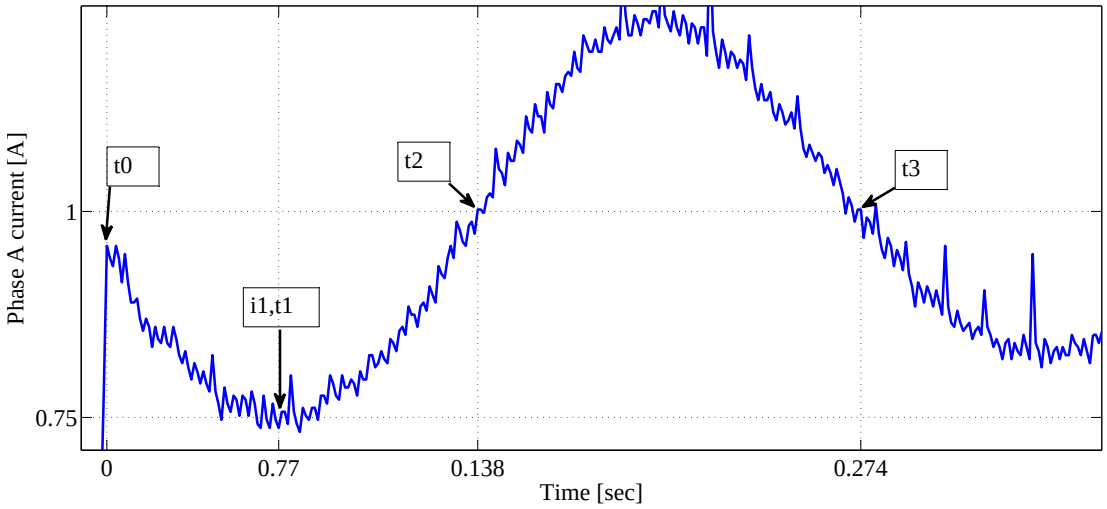

Figure 3.24: Enlarged view of measured phase A current during rotor oscillation

Since an impulse angle of $\frac{\pi}{6}$ rad is applied:

$$k = \frac{-\frac{\pi}{6}}{e^{\sigma(0)}sin(\omega_d(0) + \frac{3\pi}{2})} = \frac{-\frac{\pi}{6}}{sin(\frac{3\pi}{2})} = \frac{\pi}{6}\,rad \tag{3.65}$$

The complex components ω_d and σ are calculated with the time measurement t_0, t_2 and t_3 by:

$$\omega_d = \frac{\frac{1}{2}\pi}{t_2 - t_0} = 11.38\,\frac{rad}{sec} \tag{3.66}$$

$$\sigma = \frac{\omega_d cos(\omega_d(t_3 - t_0) + \frac{3\pi}{2})}{sin(\omega_d(t_3 - t_0) + \frac{3\pi}{2})} = 0.26\,\frac{rad}{sec} \tag{3.67}$$

The natural circular frequency ω_n is calculated with:

$$\omega_n = \sqrt{\omega_d^2 + \sigma^2} = 11.39\,\frac{rad}{sec} \tag{3.68}$$

and the damping ration ζ is calculated with:

$$\zeta = \frac{\sigma}{\omega_n} = 0.023 \tag{3.69}$$

Equations for the rotor's angular position θ_e and angular velocity ω_e is calculated from the above constants as:

$$\theta_e(t) = \frac{\pi}{6}e^{-0.26t}sin\left(11.38t + \frac{3\pi}{2}\right) + \frac{\pi}{6} \tag{3.70}$$

$$\omega_e(t) = \frac{d\theta_e(t)}{dt} = \frac{\pi}{6}e^{-0.26t}\left(-0.26sin(11.38t + \frac{3\pi}{2}) + 11.38cos(11.38t + \frac{3\pi}{2})\right) \tag{3.71}$$

The time and current measured at measuring point t_1 is now used to calculate the rotor flux magnitude λ_m by:

$$\lambda_m = \frac{V_{a-c(avg)} - i_{a(min)}(R_a + R_c)}{\omega_e(t_1)(sin(-\theta_e(t_1) + \frac{\pi}{6}) - sin(-\theta_e(t_1) + \frac{3\pi}{2}))} = 0.0452\,\frac{V.s}{rad} \tag{3.72}$$

and

$$K_e = P\lambda_m = 0.633\,\frac{V.sec}{rad}$$

The average phase A current I_a is used to calculate the moment of inertia with:

$$J_1 = \frac{3P^2\lambda_m i_a}{2\omega_n^2} = 0.103\,\frac{N.m.sec^2}{rad} \tag{3.73}$$

and the friction coefficient is calculated by:

$$B_f = 2\zeta\omega_n J_1 = 0.0531\,\frac{N.m.sec}{rad} \tag{3.74}$$

After the rotor oscillation has subsided and the phase A current has a constant value once again, an inductor discharge test is used to identify the stator phase inductance. This is done by instantaneously switching the phase A high-side switch Q_1 off and switching the phase A low-side switch Q_4 on while keeping phase C low-side switch Q_6 on, as shown in Figure 3.25. The stator inductance now discharges through the stator resistance with the current path, as shown in Figure 3.25.

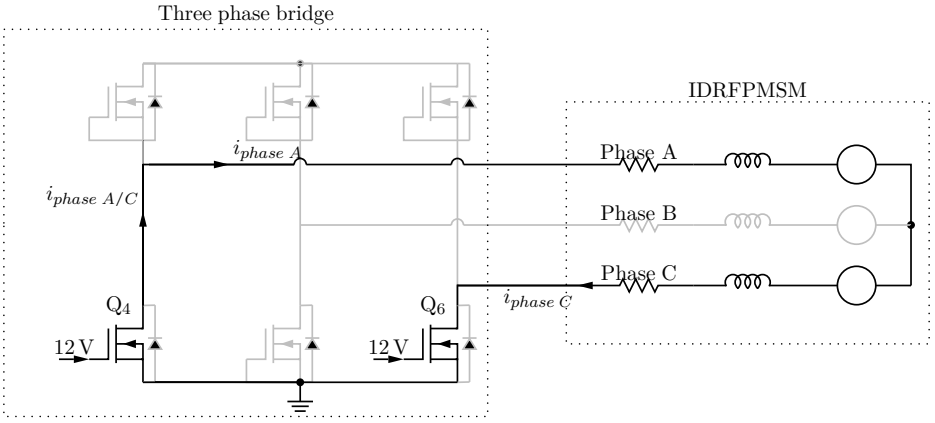

Figure 3.25: Current discharge circuit

Figure 3.26 shows a zoomed view of a measured phase A current curve during the inductor discharge test. Measuring point t_4 is recorded just before the discharge test is implemented and measuring point t_5 is recorded when the phase current has decayed to 33 % of the value at t_4. The stator coil inductance is now measured with:

$$L = \frac{R(t_5 - t_4)}{ln(\frac{1}{0.33})} = 0.902R(t_5 - t_4) = 147\,\mu H \tag{3.75}$$

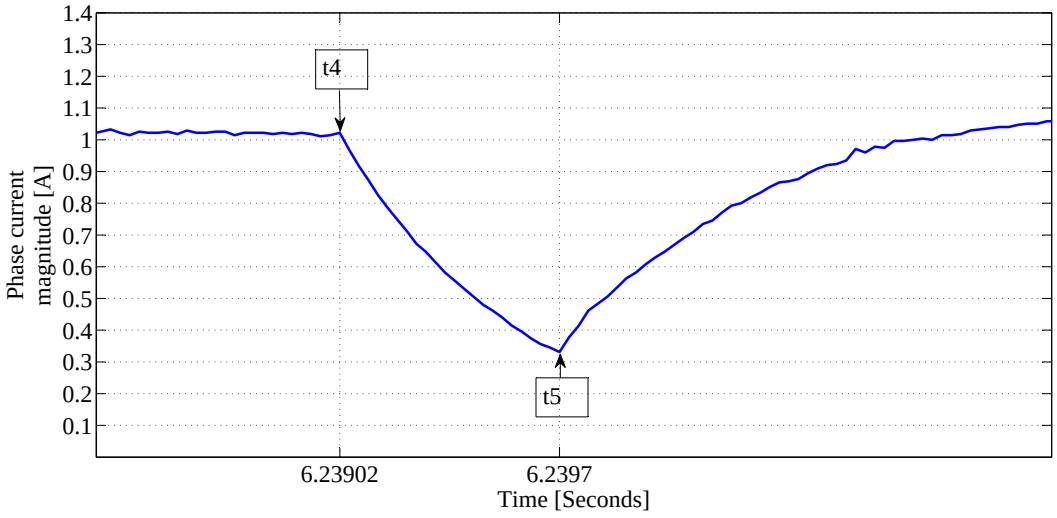

Figure 3.26: Enlarged view of measured phase A current during inductor discharge test

3.7.3 Comparison between parameter measurement methods

Figure 3.2 shows the PMSM parameter measurement results of the different methods discussed in this chapter. The first column indicates the parameter names, the second column their units and the third column shows the measured test-bench results. The measurement taken with the test-bench method is used as a reference with which to compare the results of the sensorless methods. The fourth column shows the results obtained with a Texas Instrument DRV8301-69M kit and the accompanying InstaSPIN software. The measurements in columns three and four in Figure 3.2 correlate well. The fifth column shows the measurements recorded with the on-line method and the sixth column those recorded with the open-loop method. The results produced by the open-loop method show accurate stator resistance and stator inductance, but less accurate rotor-flux magnitude, friction coefficient and moment of inertia. The on-line method has showed better measurement accuracy but requires closed-loop operation. The control-system requires a moderately accurate machine-model for stable closed-loop operation. Both the open-loop and on-line methods therefore needs to be implemented. At system start-up the open-loop method measures a rough estimate of the machine-parameters which allow for stable closed-loop operation. The on-line method later refines the parameters measured during closed-loop operation.

Table 3.2: IDRFPMSM parameter measurement results

Parameter	Unit	Testbench	InstaSPIN	Online	Openloop
R	Ω	0.2	0.199	-	0.226
L	μH	143	131	-	147
K_e	$\frac{V \cdot sec}{rad}$	0.7964	0.699	0.65	0.633
B_f	$\frac{N \cdot m \cdot sec}{rad}$	0.0395	0.042	0.045	0.0531
J	$\frac{N \cdot m \cdot sec^2}{rad}$	0.1396	0.143	0.128	0.103

3.8 Chapter conclusion

An accurate machine-model is essential to closed-loop control, sensorless position and velocity estimation. This chapter introduces different methods to identify the PMSM parameters. This chapter starts by introducing an accurate test-bench parameter measurement technique. If a rotor position sensor is available, this test-bench technique is by far the easiest method of machine parameter identification. The MSF-sensor introduced in the previous chapter was used in the test-bench setup, however, any linear rotor position sensor with sufficient resolution can be used. Sensorless PMSM parameter estimation is a more complex endeavour. This chapter tackles this challenge in two phases. First an impulse test is used to obtain a rough estimate of the system parameters. The full analytical description of the PMSM's behaviour during this impulse test is discussed. These rough-estimate parameters are accurate enough to allow for stable closed-loop operation. The on-line method can next be used to refine the PMSM parameters.

Chapter 4

Hardware design

4.1 Hardware design chapter overview

The decisions on critical hardware design made during the development of the inverter are discussed in this chapter. Two consecutive versions of the inverter were developed during this project. The purpose of the first circuit board was to demonstrate proof of concept and to eliminate any errors. Even though the circuit functioned correctly, this first circuit board had noise problems, which could be traced to poor PCB layout. The noise reduction techniques are discussed in the literature study section of this chapter. The most effective noise reduction techniques were implemented in the second version of the circuit board, solving the noise and ringing problems completely.

The two design objectives are the highest inverter efficiency and smallest PCB size. Throughout the chapter much emphasis is placed on reducing the power dissipated in each component as well as reducing component size where possible. This chapter only presents the power dissipated in each circuit region.

4.2 Chapter outline

Research relevant to the development of the inverter is presented in the literature study section in 4.3. The design of the two consecutive inverter versions is discussed in 4.4, followed by the measured inverter efficiency in 4.5 and chapter conclusion in 4.6.

4.3 Literature study related to hardware design

4.3.1 Background

As the demand for smaller and more efficient power supplies becomes more important, faster power supply switching times are required. These fast switching times could cause the following undesired phenomena [22]: Fast switch-node voltage transition can cause inadvertent low-side MOSFET turn-on that could generate shoot-through currents and as a result reduced inverter efficiency and could even lead to inverter failure. In addition the fast switching times cause voltage ringing on the switch-node which in turn contributes to the noise of the system, and could cause device failure in severe cases if the maximum voltage ratings are exceeded.

Figure 4.1 shows a block diagram of a three-phase MOSFET-bridge. The three-phase MOSFET-bridge and three-phase motor could be viewed as three identical synchronous buck-converters. In this subsection the discussion focuses specifically on a single synchronous buck-converter and the results could be duplicated in all three phases.

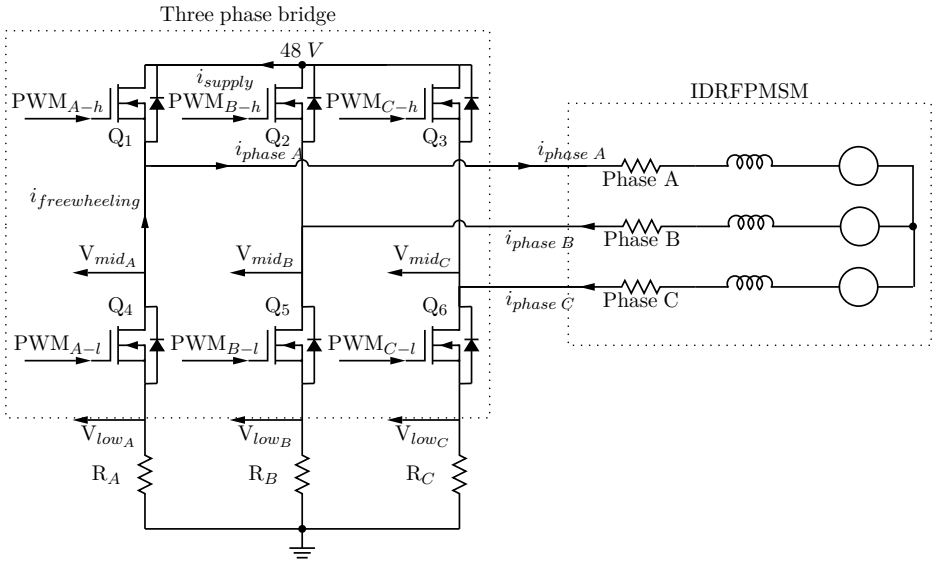

Figure 4.1: The three-phase MOSFET-bridge

4.3.2 Inadvertent low-side MOSFET turn-on due to fast switch-node voltage transition

Figure 4.2 shows a schematic-diagram of a synchronous buck-converter. Please take note of the "switch-node" label.

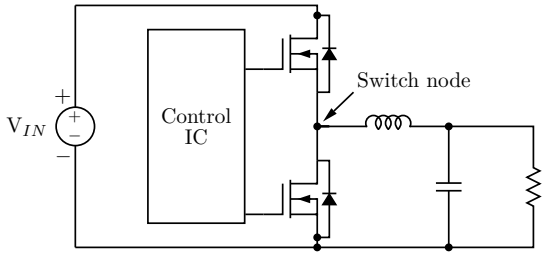

Figure 4.2: Schematic diagram of a synchronous buck-converter

Figure 4.3 shows a MOSFET-model with the following parasitic components: Drain-to-gate capacitance C_{DG}, gate-to-source capacitance C_{GS} and the parasitic transistor in the MOSFET structure with its base-to-source resistor R_{BS} and the base-to-drain capacitor C_{BD} [23].

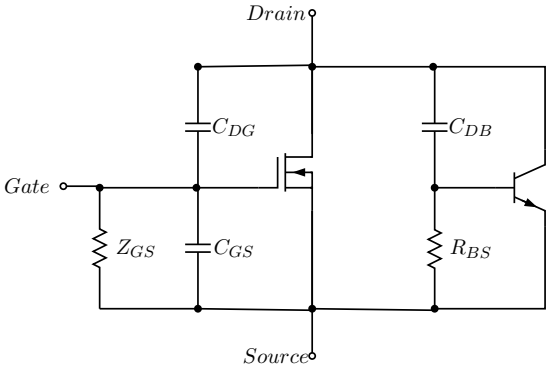

Figure 4.3: MOSFET model [23]

When the low-side MOSFET is conducting, its drain-to-source voltage is small. If the low-side MOSFET is switched off and the high-side MOSFET is switched on, the voltage across the low-side MOSFET rapidly increases, causing a current to flow through the drain-to-gate capacitor C_{DG}, gate resistance R_G and through the gate-driver to ground. If the voltage-change occurs too quickly and the gate-driver cannot drain the low-side gate-charge fast enough through the gate-resistance, the low-side gate-to-source voltage rises. Should the low-side gate-to-source voltage rises above the low-side MOSFET threshold voltage, the low-side MOSFET switches on, causing a shoot-through current. [23].

The internal parasitic transistor of the MOSFET should also be considered. Should the drain-to-source voltage $\frac{dV_{ds}}{dt}$ changes too quickly, the voltage across the internal base-to-source resistor R_{BS} could cause the base-emitter junction of the internal parasitic transistor to be forward biased and could lead to device failure [23].

4.3.3 Voltage ringing phenomenon caused by parasitics

There are two major concerns regarding switch-node voltage ringing: The voltage overshoot could damage components if their maximum voltage-ratings are exceeded. The voltage ringing also contributes to conducted and radiated electromagnetic noise [24].

Figure 4.4 shows a schematic diagram of a synchronous buck-converter. Please take note of the parasitic components indicated in red. The switch-node ringing phenomenon is caused as follows [24], [25]: During the time period when the low-side MOSFET is switched on, current is conducting from source-to-drain through the low-side MOSFET. During the dead-time period after the low-side MOSFET is switched off, current is conducting through the low-side MOSFET body-diode and energy is stored in the low-side parasitic inductances. The high-side MOSFET is switched on after the dead-time period. The low-side parasitic inductances want to discharge its stored energy, thereby forcing the low-side body-diode to conduct and raising the switch-node voltage above the bus-voltage level (causing the first switch-node voltage overshoot). Once the energy stored in the low-side parasitic inductances is depleted, current flows from the supply-rail through the parasitic inductances to raise the low-side body-capacitance voltage to bus-voltage level. The parasitic inductances will once again discharge its stored energy into the low-side body-capacitance causing its voltage to rise above the bus-voltage level. The low-side body-capacitance then discharges through the low-side parasitic inductances once again and the cycle is repeated.

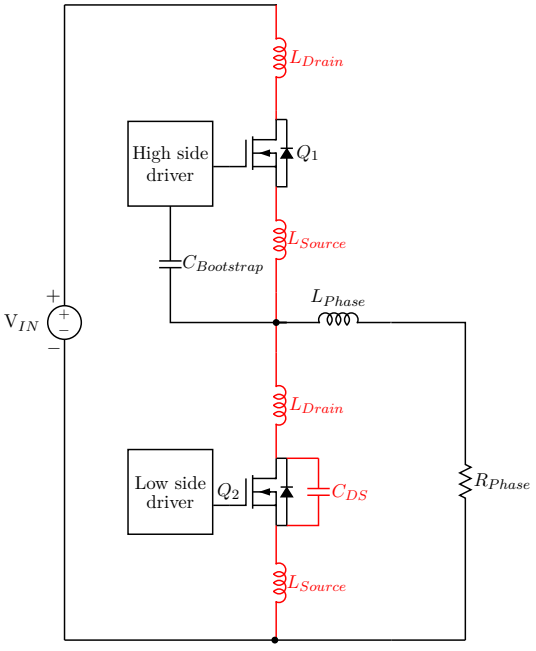

Figure 4.4: Synchronous buck-converter with parasitic components

Figure 62 shows an example graph of the switch-node voltage ringing due to parasitic components when the high-side MOSFET is switched on.

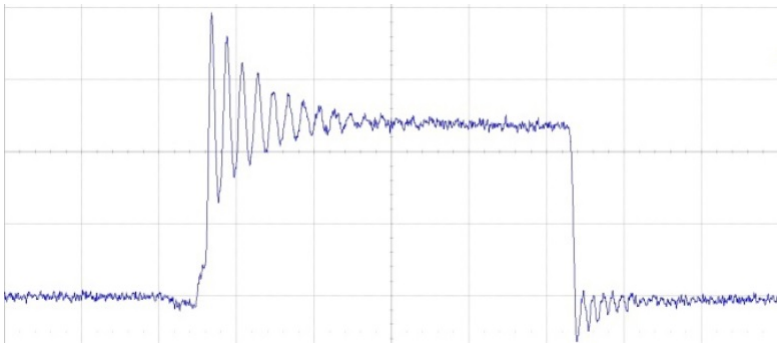

Figure 4.5: Switch-node voltage ringing due to parasitic components [24]

4.3.4 Parasitic ringing suppression methods

There are a couple of methods suggested to prevent and suppress switch-node voltage ringing. These methods include: correct PCB layout, adding a MOSFET series gate resistance, adding a discharge diode to the gate resistance, adding a bootstrap resistance and adding a snubber circuit.

Correct PCB layout

Parasitic ringing can be significantly reduced by careful PCB layout as discussed in [24],[26]. One of the components singled out in the discussion in [24] is the input capacitor. The track distance between the input capacitor and the high-side MOSFET drain as well as the track distance between the input capacitor and the low-side MOSFET source should be as short as possible to minimise the parasitic (track) inductance. In typical PCB layouts a compromise is made to have one short track and the other longer. Figure 4.6 suggested a synchronous buck PCB layout that minimises both input capacitor track lengths [24]. Figure 4.6 shows the input-capacitors positioned right next to the high-side MOSFET drain and low-side MOSFET source. Two PCB layouts (a typical layout and an optimised layout) were tested by the author in [24] and found a 20% reduction in ringing amplitude with the optimised PCB layout compared to the typical PCB layout. The author further stated the importance of using ceramic capacitors for the input capacitor due to its inherently low equivalent series inductance (ESL) and low equivalent series resistance (ESR).

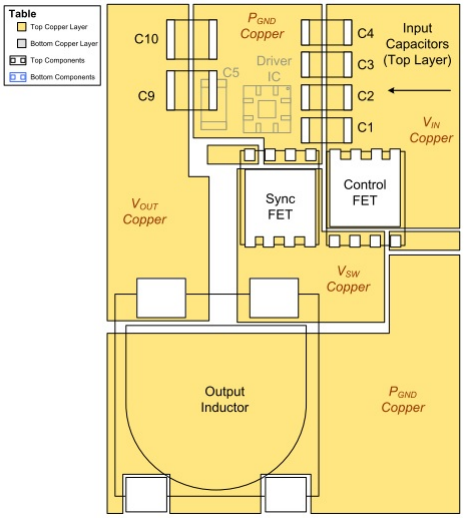

Figure 4.6: Synchronous buck PCB-layout that minimises input capacitor track length[24]

Gate resistance

The ringing can be reduced or prevented by slowing down the high-side MOSFET turn-on time. This is accomplished by adding a series high-side gate resistance as shown in Figure 4.7, which is discussed in [24] and [27].

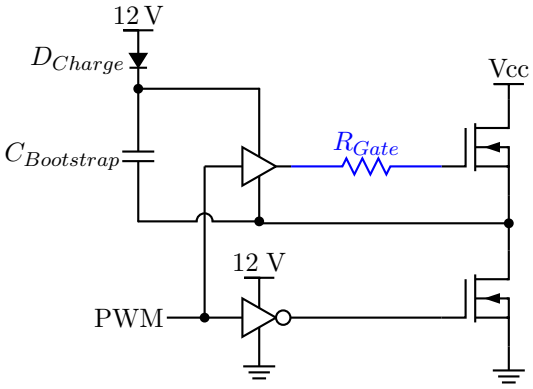

Figure 4.7: Synchronous buck-converter with high-side gate resistance

Gate resistance with discharge diode

The ringing occurs only when the high-side MOSFET is switched on. Adding a high-side MOSFET gate resistance will slow-down the switch-on and switch-off times, thereby increasing switching-losses in both transitions [24]. Since only the high-side switch-on time needs to be slowed down, the high-side switch-off time remains short if an additional discharge path is provided. The discharge path is provided by adding a gate-discharge diode in parallel to the high-side gate-resistor, as shown in Figure 4.8. The high-side gate

now slowly charges through the gate-resistor and discharge quickly through the diode at switch-off.

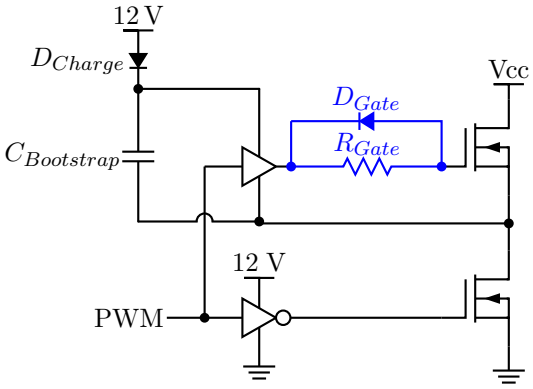

Figure 4.8: Synchronous buck-converter with high-side gate charge resistance and discharge diode

Bootstrap resistor in series with the bootstrap capacitor

Slow high-side switch-on and fast switch-off can also be achieved by adding a bootstrap resistor in series with the bootstrap capacitor, as shown in Figure 4.9 and discussed in [24], [27] and [26]. The biggest concern with adding a bootstrap resistor is since the bootstrap capacitor charges through the bootstrap resistor during the low-side on-state, the bootstrap capacitor might not be able to replenish its charge during short low-side on-state times (therefore high switch-node duty cycle).

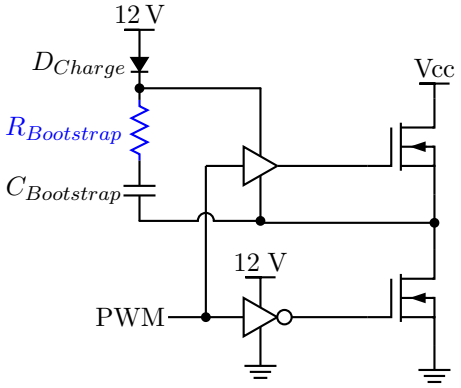

Figure 4.9: Synchronous buck-converter with bootstrap resistor

Snubber circuit

Switch-node ringing can also be suppressed by adding a snubber circuit, as discussed in [24], [27] and [26]. A synchronous buck-converter with a snubber circuit is shown in

Figure 4.10. A snubber circuit consists of a capacitor in series with a resistor connected between the switch-node and ground. The snubber capacitor value is calculated so that the high-frequency ringing energy is dissipated in the snubber resistor thereby suppressing the switch-node ringing above the selected frequency range. Snubbers tend to be quite lossy and will therefore not be implemented in this PCB layout.

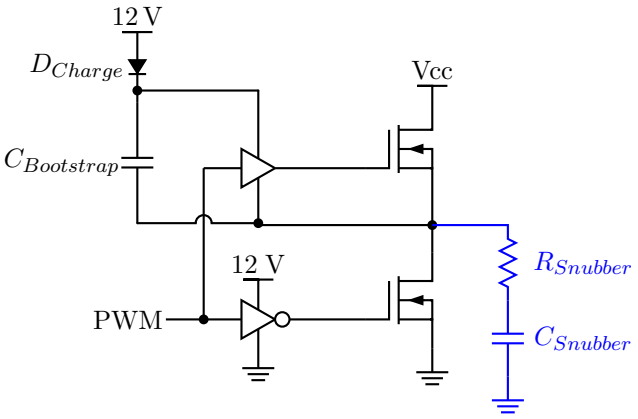

Figure 4.10: Synchronous buck-converter with snubber circuit

Noise isolation - Ground plane design

Williams at al. [28] stated that designing for good electromagnetic compatibility (EMC) starts with controlling the flow of interference into and out of electronic devices. All active devices generate some degree of interference. To improve EMC, barriers are placed to divert or absorb interference before entering or exiting a circuit.

Since the copper tracks on the PCB has resistance, according to Ohm's law, a current flowing through the PCB tracks will cause a voltage drop across it. This therefore means that two different points on the same current-conducting track (or conductive area) is not at the same voltage potential. Should this current be a square-wave signal, according to Fourier-series expansion a whole spectrum of harmonics is generated. This is a cause of PCB noise. The effect of this noise can be minimised in two ways: By using ground planes the resistance between two ground points can be minimised and therefore smaller noise amplitude is generated. Secondly, separate ground plane areas with only one entry point ensures current that does not belong in a certain area cannot flow in that area.

Noise isolation - Noise shielding with ferrite beads

Ferrite chokes or sleeves are added regularly to cables to reduce incoming and outgoing RF noise between electronic devices. The same technique can be applied to a PCB [29].

Ferrite beads used in conjunction with bypass capacitors can provide improved power supply filtering and decoupling [30]. These ferrite beads consist of conductive wires inserted through hollow ceramic beads. At low frequencies ferrite beads act as normal inductors. As the frequency is increased, the eddy-current core-losses increase causing the ferrite bead resistance to rise. Above a certain frequency the self-capacitance of the inductor takes over and the capacitive reactance dominates causing the ferrite bead resistance to fall again [31]. Resistive bands of ferrite beads are normally above 10 MHz. The ferrite bead should be chosen so that the target noise frequencies fall within its resistive band. Figure 4.11 shows a diagram of how to use a ferrite bead in conjunction with a bypass-capacitor [30].

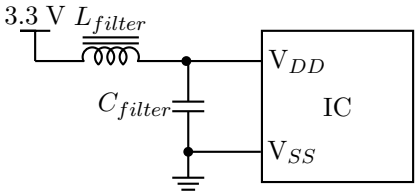

Figure 4.11: Ferrite bead used in conjunction with a bypass-capacitor

Ferrite beads can be divided into: High quality-factor (Q-factor) ferrite beads used for resonating circuits and low Q-factor ferrite beads used for noise shielding as discussed in this subsection. The Q-factor describes the relation between the inductance and resistance of the inductor. When designing this LCR filter, care should be taken to add sufficient resistive dampening should the resonant peak of the filter fall within the inductive region of the ferrite bead.

4.4 Inverter design

4.4.1 Overview

Figure 4.12 shows a block diagram of the first version of the inverter circuit board. To simplify the explanation, this block diagram is divided into a microcontroller block, MOSFET gate-driver block and a MOSFET bridge block as shown in red, green and blue respectively.

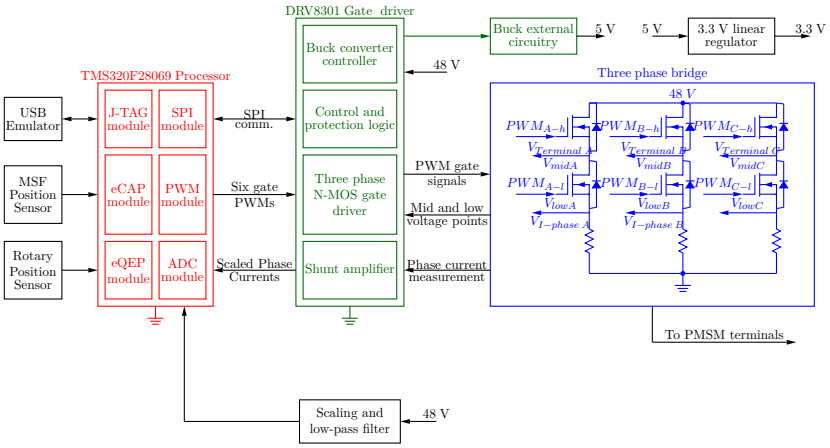

Figure 4.12: Block diagram of the first version of the inverter circuit board

4.4.2 Microcontroller block

Starting with the microcontroller block, in this project an online parameter estimator measures the machine parameters during closed-loop sensorless vector-control operation. A high-end microcontroller is required as this algorithm is computing intensive and requires both floating-point and trigonometric calculations. The following peripherals are required as shown in Figure 4.12: a capture and compare module (eCAP) to measure the MSF-sensor PWM output; a quadrature encoder module (eQEP) to read a rotary position sensor output (optional); a SPI module to initialise the DRV8301 control and protection logic registers; six MOSFET-gate PWM output pins; and three analogue-to-digital converter (ADC) pins to measure the two phase currents and the scaled and filtered supply voltage. The Texas Instruments TMS320F28069 microcontroller was chosen as it has a dedicated 32-bit floating-point processor, it can operate with a 90 MHz clock frequency and it has all the peripherals required for the project.

4.4.3 MOSFET gate-driver block

The IDRFPMSM is a 48 V machine. The inverter therefore needs to be able to operate from supply voltages exceeding 48 V. The external position sensors require a 5 V supply-rail. The microcontroller requires a 3.3 V supply-rail. A buck-converter is used to step the 48 V-bus down to 5 V. A 3.3 V linear regulator (TPS73633) is used to step 5 V to 3.3 V. A current of 0.13 A is expected on the 3.3 V bus resulting in 0.44 W dissipated in the 3.3 V circuitry and 0.23 W dissipated in the 3.3 V linear regulator.

A few IC developers, including Texas Instruments, Microchip and Renesas, manufacture all-in-one: buck-converter, three-phase gate driver and shunt-amplifier IC devices. Texas

Instruments is the only manufacturer of devices that can operate at bus-voltages of up to 60 V. The Texas Instruments DRV8301 is chosen. This will allow a 12 V safety margin (48 V to 60 V) during regenerative breaking. The DRV8301 has a built-in buck-converter controller, a three-phase gate driver, software-settable shunt amplifiers (which is settable through SPI) and control-and-protection logic, as shown in Figure 4.12.

4.4.4 Buck-converter design

Figure 4.13 shows the buck-converter circuit diagram. The high-side switch, gate driver and controller are embedded in the DRV8301 device. The external components consist of the bootstrap capacitor C_{54}, the freewheeling diode D_{12} and LC-filter consisting of L_{15} and C_{55}. Resistors R_{34} and R_{37} form a voltage divider that supplies the controller with feedback. A current of 0.2 A is expected on the 5 V rail, which is dependent on the current demand of position sensor used. The buck-converter is designed to deliver an acceptable efficiency while keeping the PCB footprint small and the voltage ripple low. A buck-converter switching frequency of 581 kHz was chosen to keep switching-losses low. Since a fairly constant current is drawn, a maximum inductor current ripple of 0.2 A is chosen. The inductor-current therefore oscillates between 0.1 A and 0.3 A when a 48 V-supply is used. This larger inductor current ripple keeps the inductance value lower, thereby keeping the physical inductor size smaller. The inductor L_{15} is calculated with:

$$L_{15} = \frac{V_{out}(V_{in} - V_{out})}{V_{in} f_{switch} \Delta i_{L_{15}}} = 38\mu H \tag{4.1}$$

An output voltage ripple of 0.001 V is chosen. The capacitor C_{55} is calculated with:

$$C_{55} = \frac{V_{out}(V_{in} - V_{out})}{8 V_{in} f_{switch}^2 L \Delta V_{C_{55}}} = 43\mu F \tag{4.2}$$

The larger inductor current ripple results in higher current flowing into and out of C_{55}. Ceramic capacitors have very low equivalent-series resistance (ESR) and would therefore cause the least amount of conduction losses.

The controller comparator has a 0.79 V reference. The feedback scaling is chosen so that a 5 V output will produce a feedback of 0.79 V. Voltage divider resistor R_{37} is chosen as 10 kΩ. Resistor R_{34} is calculated with:

$$R_{34} = \frac{R_{37}(V_{out} - V_{ref})}{V_{ref}} = 53.3k\Omega \tag{4.3}$$

A total of 0.17 W is dissipated in the buck-converter circuitry, giving it a conversion efficiency of 60.6%. Since the power delivered to the 5 V rail is very low, the buck-converter efficiency has little influence on the overall system efficiency. During normal operation the DRV8301 device draws a constant 15 mA current. With a 48 V supply the DRV8301 will dissipate 0.75 W.

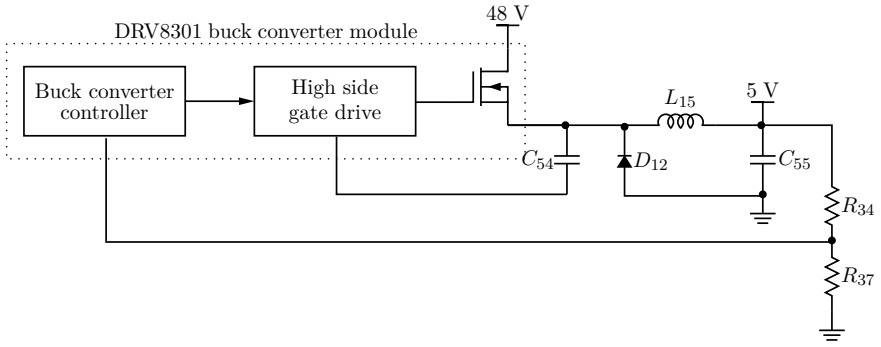

Figure 4.13: Buck-converter circuit diagram

4.4.5 Bus-voltage measurement

The firmware algorithm uses the bus-voltage measurement for duty-cycle calculation and overvoltage detection. A voltage divider consisting of R_7 and R_{10} scales the bus voltage to an acceptable measurement range, as shown in Figure 4.14. Resistor R_7 is chosen as 100 kΩ to minimise the voltage-divider current and power dissipated. The value of R_{10} is calculated so that the analogue-to-digital converter pin of the microcontroller measures a full-scale deflection of 3.3 V at a bus-voltage of 73 V. The 25 V safety margin ensures the microcontroller will not be damaged during overvoltage or surge conditions. Resistor R_{10} is given by:

$$R_{10} = \frac{V_{ADC\_max} R_7}{V_{bus\_max} - V_{ADC\_max}} = \frac{3.3\,V * 100\,k\Omega}{73\,V - 3.3\,V} = 4.7k\Omega \tag{4.4}$$

The MOSFET bridge PWM signals generate a full spectrum of harmonics as described by Fourier series expansion. A filter capacitor is added to the voltage-divider circuit to retain only the lower harmonics. The low-pass filter cut-off frequency is chosen higher than that of the speed loop so not to inhibit the control and overvoltage detection during regenerative braking. Ultimately, the low-pass filter cut-off frequency has to be lower

than the three-phase bridge switching frequency. A cut-off frequency of 300 Hz is chosen that will cause a negligible phase shift (at the speed-loop frequency) but filter out most unwanted noise. The filter capacitor C_{26} is calculated from:

$$C_{26} = \frac{1}{2\pi f_{\text{cutoff}}(\frac{R_7 R_{10}}{R_7+R_{10}})} = \frac{1}{2 * \pi * 300 * (\frac{100k\Omega * 4.7k\Omega}{100k\Omega+4.7k\Omega})} = 118\,nF \tag{4.5}$$

The voltage divider dissipates 22mW in total with a supply voltage of 48V.

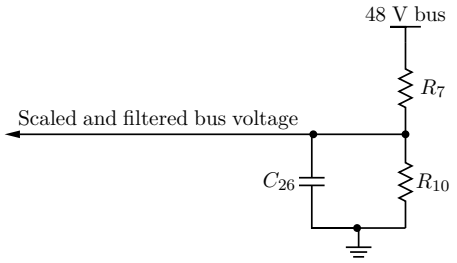

Figure 4.14: Bus-voltage scale and filter circuit

4.4.6 Three-phase MOSFET bridge

Figure 4.15 shows a block diagram of the three-phase MOSFET-bridge. The bridge consists of six MOSFET switches, one high-side switch and one low-side switch for each of the three phases. The IRFS3307Z N-channel power-MOSFET was chosen for the first PCB since it has a fairly low on-state resistance of 4.5 mΩ and can handle a maximum drain-source voltage and current of 75 V and 120 A respectively.

A 15 mΩ current-measurement resistor is connected between each low-side MOSFET source pin and ground. The voltage drops across these resistors are amplified by the software-settable shunt amplifiers of the DRV8301. The firmware algorithm uses these amplified voltage drops to calculate the phase current of the machine.

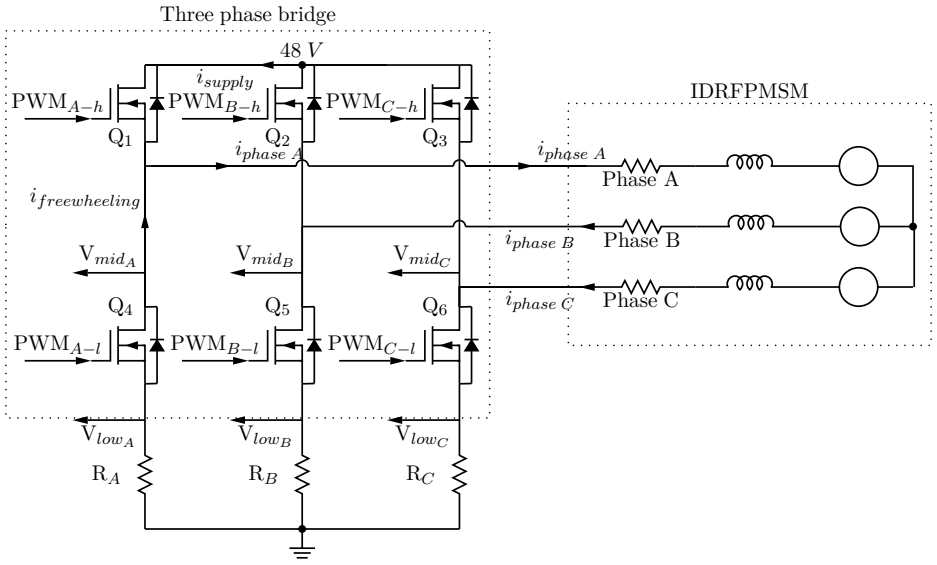

Figure 4.15: The three-phase-MOSFET-bridge

Figure 4.16 shows a picture of the first inverter PCB

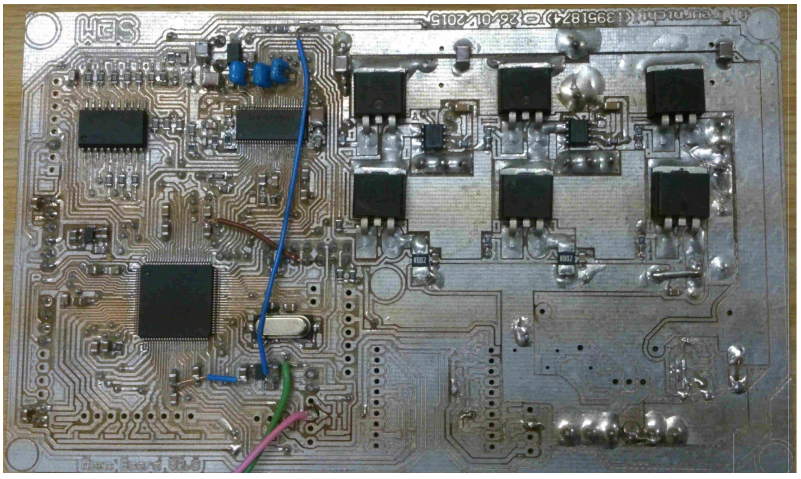

Figure 4.16: First inverter PCB

4.4.7 Calculated efficiency of the first inverter PCB

The inverter losses are categorised under constant-losses, conduction-losses and switching-losses. The constant-losses cover all the inverter losses except that found in the three-phase bridge. All losses discussed thus far are constant-losses which are unaffected by inverter power output. Conduction-losses are caused by current flowing through resistive loads. The two largest conduction-loss contributors are the current-sense resistors (R_{49}-R_{51}) and the bridge MOSFETs during their on-state (Q_1-Q_6).

The switching-loss contributors consist of the power dissipated in the bridge-MOSFETs while switching on and off as well as the power required to charge the MOSFET gate-capacitance every time a MOSFET is switched on. The switching-losses contribute the majority of the inverter losses and can be reduced by lowering the switching frequency. The downside of this is as the switching frequency is lowered, the phase current ripple increases. The peak phase current ripple is calculated using:

$$\Delta i_{L(peak)} = \frac{V_{supply}}{4 L_{phase} f_{switch}} \tag{4.6}$$

where V_{supply} is the supply voltage, L_{phase} is the phase inductance of the machine and f_{switch} is the PWM switching-frequency.

An increase in current-ripple size or frequency will cause an equivalent increase in eddy-current losses in the machine [32], as well as an increase in inverter noise [28]. A specific work point that provides acceptable efficiency and phase current ripple therefore needs to be chosen.

Figure 4.17 shows the calculated peak-efficiency and peak phase current ripple of the first inverter (when $V_{out}=\frac{1}{2}V_{supply}$) against switching frequency with the IDRFPMSM spinning at a full speed of 300 rpm and phase current of 8.5 A_{rms}. A peak current ripple of 15.32 % is expected with a switching frequency of 50 kHz. This will ensure an inverter efficiency of 97.69 % at 432 W output power.

The inverter efficiency is influenced by both the switching frequency and the power delivered to the load. The load power depends on the torque or current delivered as well as the generated BEMF of the machine which is speed dependent. The inverter efficiency declines to the same extent as the rotor speed or torque demand. Figure 4.18 shows the inverter efficiency curve with a constant phase current and changing rotor speed. Above 100 rpm (150 W delivered to the load) the efficiency curve stays quite flat in the high 90 % efficiency range. Below 100 rpm the inverter efficiency declines very quickly. This is due to lack of generated BEMF-voltage at this low rotational speed.

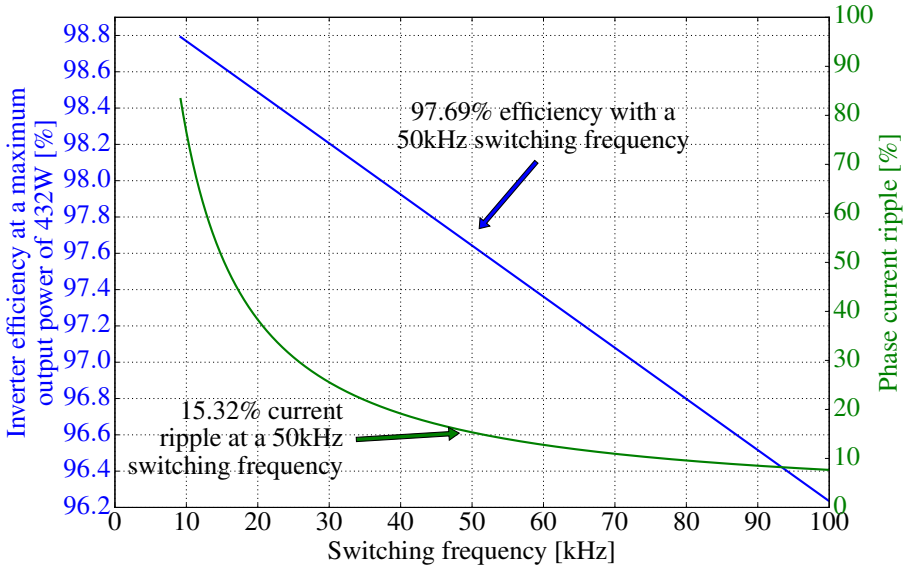

Figure 4.17: Correlation between inverter efficiency, phase-current ripple and switching frequency of the first inverter PCB

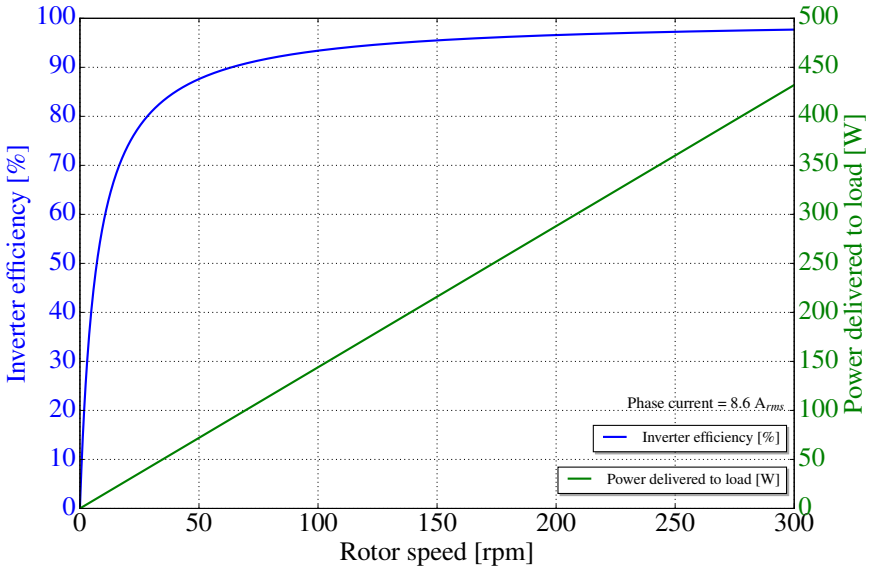

Figure 4.18: Correlation between inverter efficiency and rotor speed

Figure 4.19 shows an inverter efficiency curve with a constant rotor speed of 300 rpm and changing phase current. Similar to the speed curve in Figure 4.18, the inverter efficiency stays quite flat above a phase current of $2\,A_{rms}$. Below $2\,A_{rms}$ the inverter efficiency quickly drops.

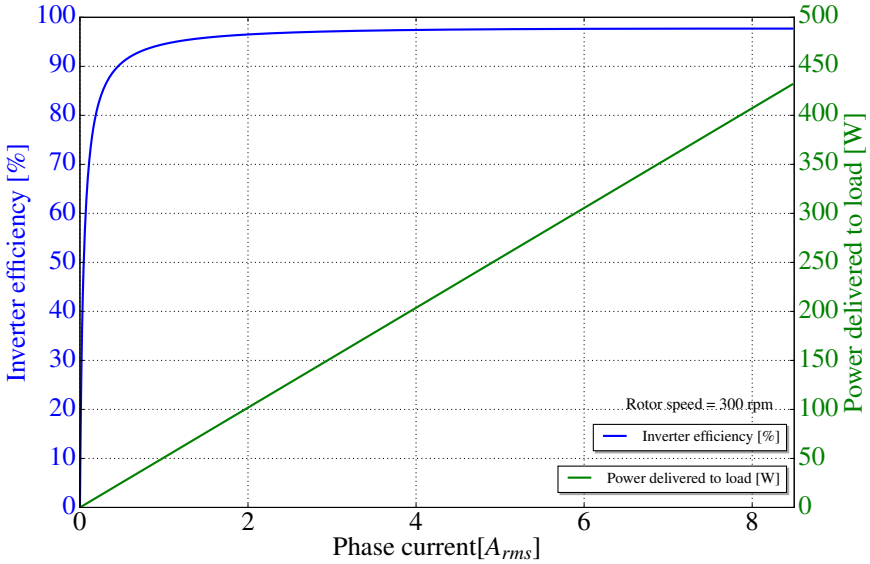

Figure 4.19: Correlation between inverter efficiency and torque demand

As seen in both Figure 4.18 and Figure 4.19 the inverter efficiency is strongly influenced by both the rotational speed and torque demand of the machine. It is therefore ideal to keep the torque and rotational speed above a certain level to achieve acceptable efficiency.

4.4.8 Changes made in second inverter PCB design

Apart from a couple of minor changes, the circuit is essentially the same in the second inverter PCB. The focus was rather to reduce noise levels. In this chapter the literature study discusses methods of minimising ringing. The noise can further be reduced by isolating certain circuit areas from the noise generated in other areas. These methods are largely implemented in this subsection.

Figure 4.20 shows a block diagram of the second inverter circuit. The elements in blue indicate changes made. A 3.3 V linear regulator that solely supplies the processor was added to isolate the supply-rail of the processor from noise generated in other areas.

Sensorless trapezoidal control is also investigated. The BEMF zero crossings on the floating machine terminals during trapezoidal control are used to estimate the rotor position. Voltage-dividers with low-pass filter capacitors were used to scale and filter the machine terminal voltage similar to that used for the bus voltage measurement earlier in this chapter, but now designed with a 2 kHz cut-off frequency.

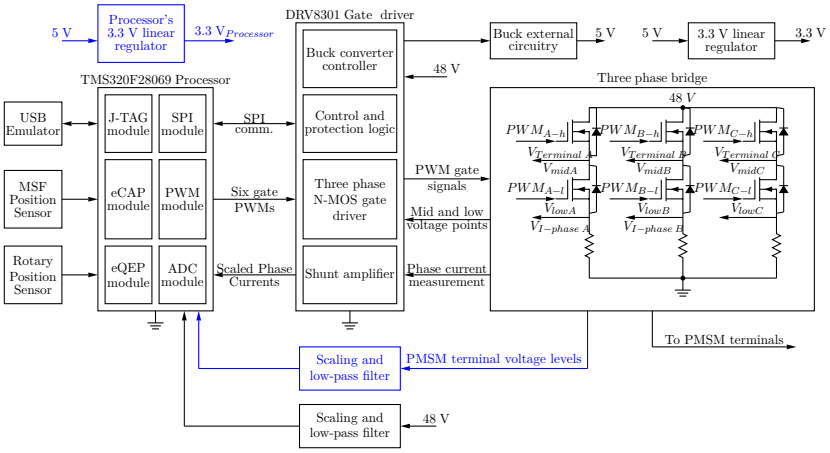

Figure 4.20: Block diagram of second inverter circuit board

Figure 4.21 shows a picture of the second inverter PCB. The circuit layout suggested in [24] to minimise the distance between the input capacitor and low-side MOSFET source pin and high-side MOSFET drain pin is implemented at label *a*. The MOSFET gate resistors were added to slow down switch-on times and reduce ringing as suggested in [24].

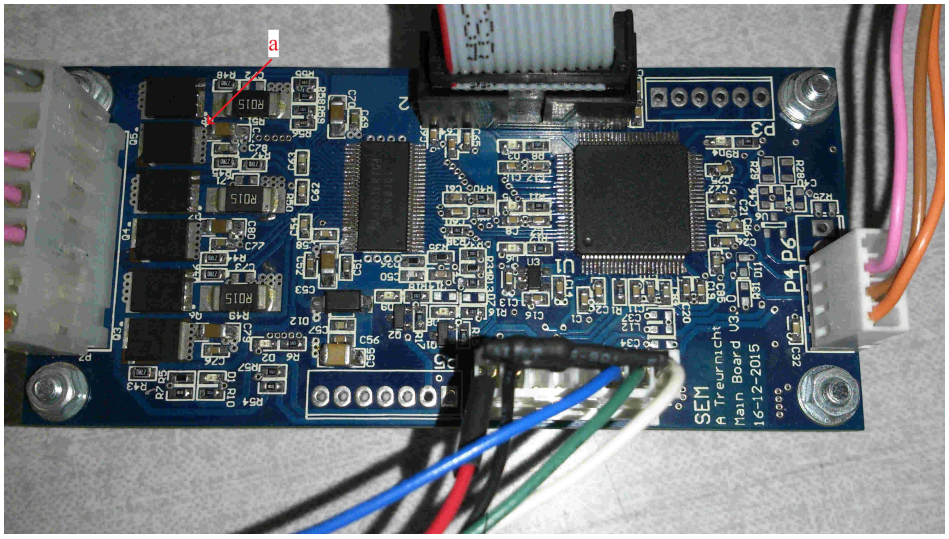

Figure 4.21: Second inverter PCB

Second-order low-pass filters consisting of ferrite beads in conjunction with bypass capacitors were added to all IC supply pins to act as filters and protect the device against voltage spikes as suggested in [30]. The filter is designed so that the resonant peak frequency

falls in the resistive region of the ferrite bead and is therefore sufficiently damped. Figure 4.22 shows a circuit diagram of the second-order ferrite bead bypass capacitor filter. [30].

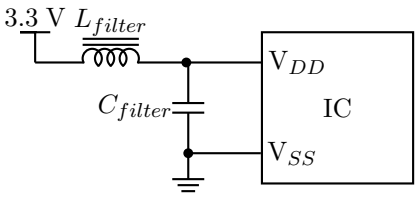

Figure 4.22: Ferrite bead used in conjunction with a bypass-capacitor

Figure 4.23 shows the second inverter PCB's ground plane Williams et al. [28] suggested that the noise generated in certain circuit areas could be reduced by preventing unwanted currents from flowing in that areas. This is implemented by dividing the ground plane up into separate areas which are only connected at a single point, as shown in Figure 4.23.

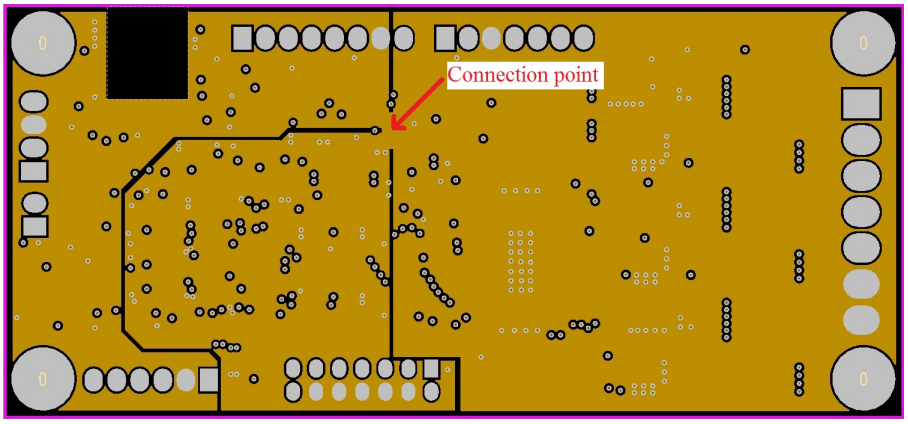

Figure 4.23: Second-inverter PCB ground-plane

It was later decided to further improve the inverter efficiency by replacing the three 15 mΩ current sense resistors with two ACS711 Hall current sensors which has only 1.6 mΩ resistance. Figure 4.24 shows the current sensors (in blue) added to the inverter block diagram. The bridge MOSFETs were also changed to CSD19502Q5B which has significantly faster switching times, lower on-state resistance and less parasitic inductance than the IRFS3307Z used in the previous version.

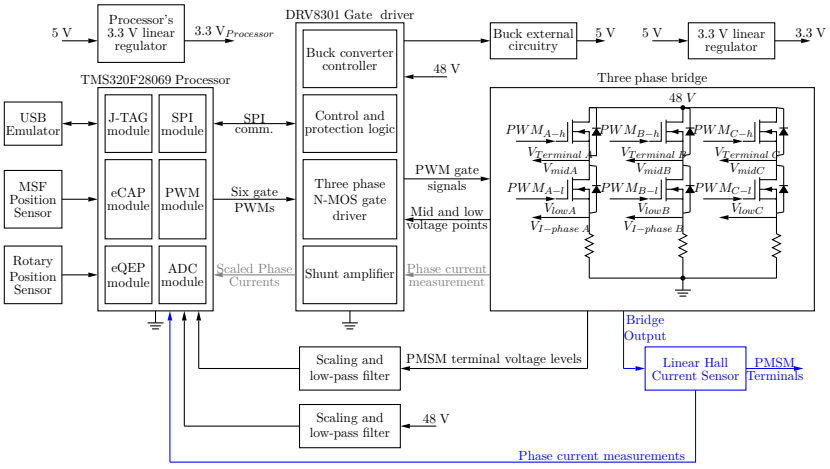

Figure 4.24: Block diagram of second inverter circuit board with Hall current sensors

Figure 4.25 shows the developed current sensor PCB. Please take note that only two-phase current measurements are needed as the machine is a balanced three-phase load. The third-phase current is calculated from the other two measurements.

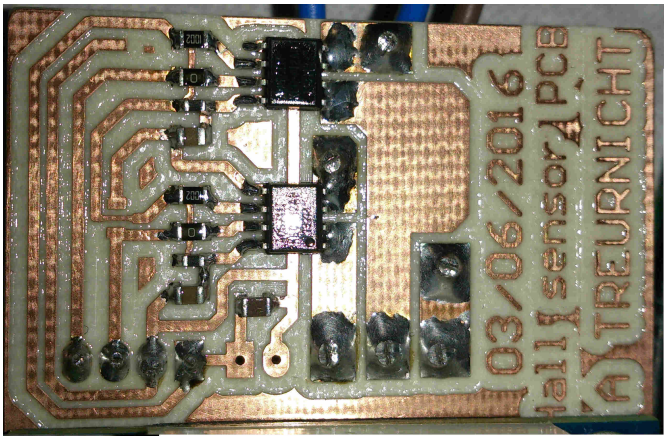

Figure 4.25: Current sensor PCB

Figure 4.26 shows a picture of the current sensor PCB installed onto the second inverter PCB.

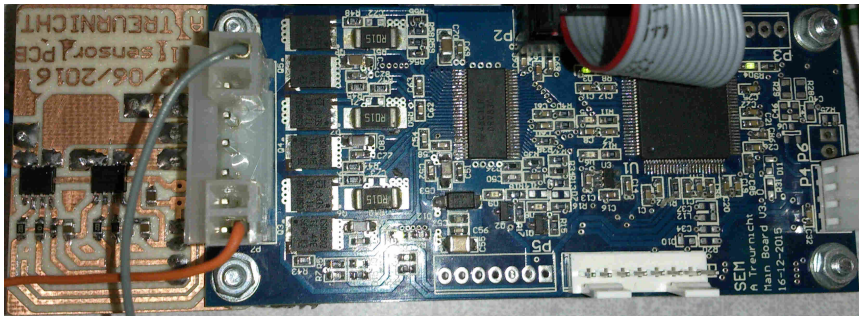

Figure 4.26: Current sensor PCB installed onto second inverter PCB

4.4.9 Calculated efficiency of second inverter PCB

Figure 4.27 shows the calculated peak efficiency and peak phase current ripple of the second inverter (when $V_{out}=\frac{1}{2}V_{supply}$) as a function of the switching frequency with the IDRFPMSM spinning at a full speed of 300 rpm and phase current of 8.5 A_{rms}. The inverter efficiency has been increased from 97.7 % to 98.95 % by improved design and component choices.

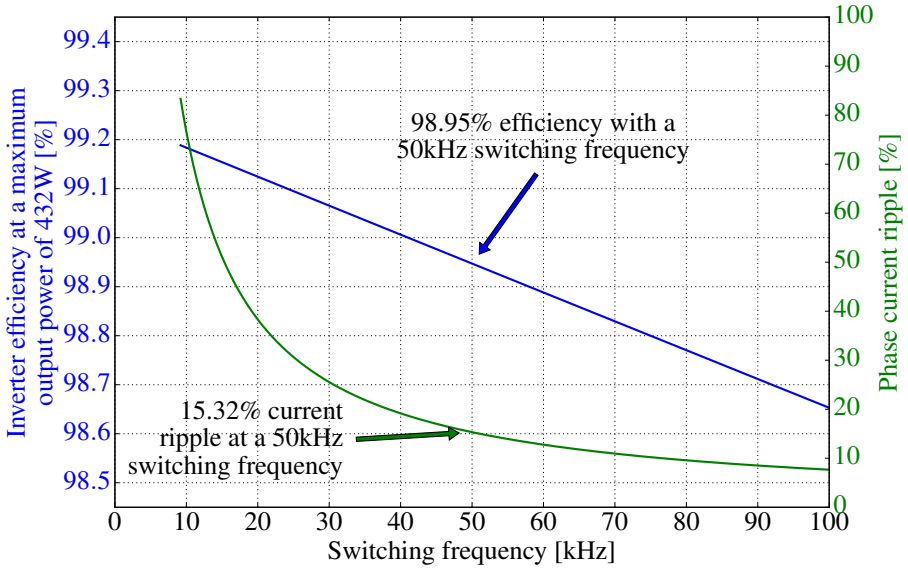

Figure 4.27: Correlation between second inverter efficiency, phase current ripple and switching-frequency

4.5 Second inverter PCB performance results

Figure 4.28 shows the switch note voltage measured between an inverter output terminal and ground. This graph shows that the machine has a period of 20 μsec, therefore a

50 kHz PWM frequency.

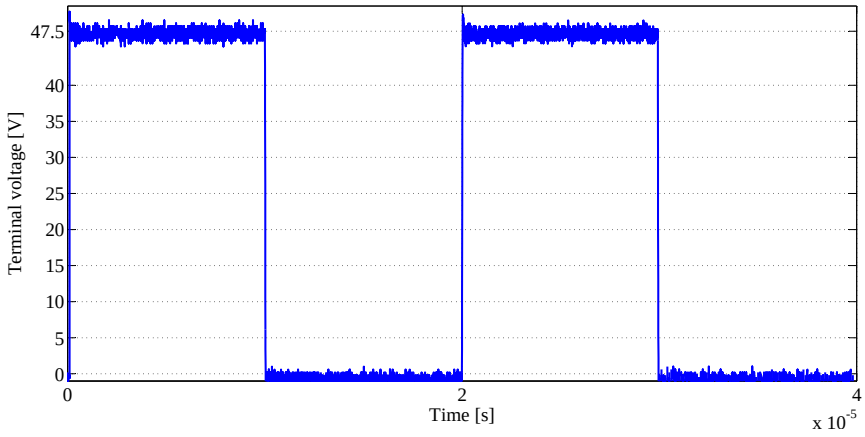

Figure 4.28: Measured PWM voltage signal

Figure 4.29 shows a zoomed view of a rising transient presented in Figure 4.28. Figure 4.29 shows that the PWM signal has a 10-90 % rise-time and fall-time of 25 ns. The changes made in the second inverter version ensured that despite this fast switching times, the ringing overshoot was dampened to a mere 6.1 %

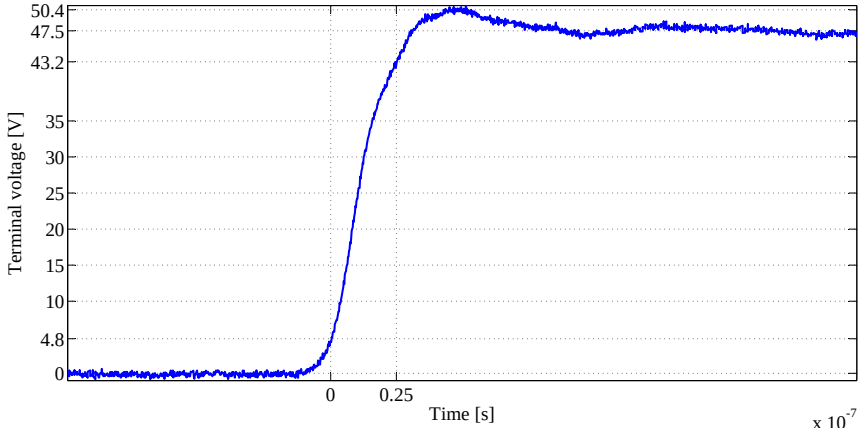

Figure 4.29: Measured rise time and ringing

Figure 4.30 shows the measured inverter efficiency against load current. These measurements were made by connecting three potentiometers in series with the three IDRFPMSM phases and applying a stator field at 0° electrical. A supply voltage of 50 V was used. Three graphs are shown: one for a 48 V output, one for a 22.6 V output and one for a 4.7 V output. The three graphs show the effect that the BEMF (or rotational speed) has on

inverter efficiency. As the load current is increased the inverter efficiency also increases as shown in Figure 4.30. The black graph shows that the second inverter PCB has a maximum inverter efficiency of 98.77 % at an output voltage of 48 V and a load current of 10 A. These measured efficiency curves correlate well with the calculated efficiency graphs presented earlier in this chapter.

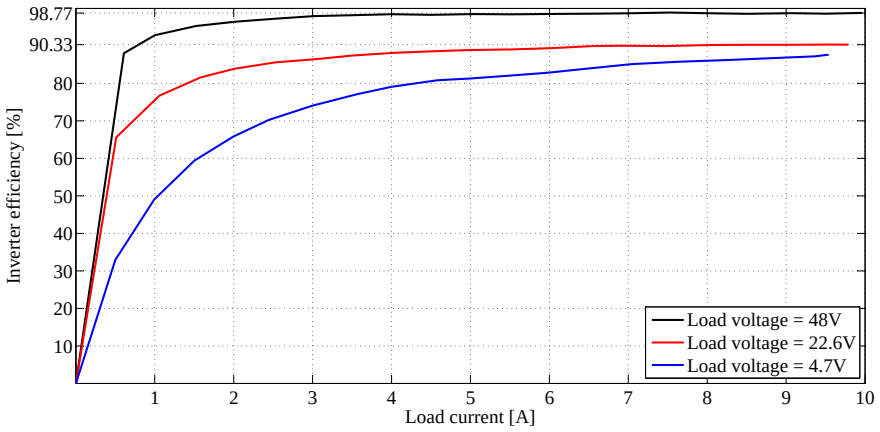

Figure 4.30: Measured inverter efficiency with different output voltages

Figure 4.31 shows the measured current ripple with a phase current (load current) of 2.76 A. The measured current ripple of 15.94 % correlates well with the 15.32 % theoretically calculated value.

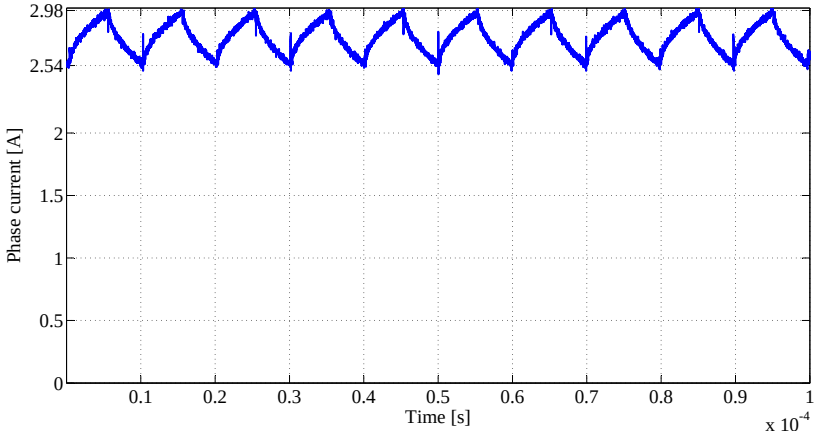

Figure 4.31: Measured current ripple

4.6 Chapter conclusion

This chapter introduced the two inverter versions that were developed during the course of this project. The two main design constraints were highest inverter efficiency and smallest PCB size. An in-depth study and explanation was presented on the influence on inverter efficiency and current ripple. The first version of the inverter functioned correctly but had severe ringing and noise problems. Research done showed that noise and ringing could be significantly reduced by clever board layout and component choices. The addition of MOSFET bridge gate resistors slowed the switching transients down, thereby dampening the ringing further. The noise problem was solved by implementing these methods in the second version of the inverter. Throughout this chapter there exists a strong correlation between calculated and measured results. With the IDRFPMSM the final measurements show an inverter efficiency of up to 98.77 % with a current ripple of 15.94 %.

Chapter 5

Closed-loop system integration

5.1 Chapter introduction

Permanent-magnet synchronous machines (PMSM) became very popular due to their high efficiency, high operating speeds and high power density, etc. [10]. To achieve peak driving efficiency with a PMSM, the stator field is applied with a vector direction perpendicular to the rotor position at all times. This in turn requires rotor-angle measurements. The current position of the rotor is required continuously, and therefore, many applications use shaft-mounted position sensors. In this chapter a sensorless rotor-position approach will be studied.

5.2 Chapter structure

A system overview is presented that explains the interaction between all the elements in the embedded system in 5.3. In the literature study section in 5.4 a deeper look is taken at the design of each of the elements, then the system design is discussed in 5.5, followed by the closed-loop system results in 5.6.

5.3 Closed-loop system overview

Figure 5.1 shows a block diagram of the entire embedded system. Assume that at start-up the open-loop parameter estimator was able to identify all the important machine parameters. The system continues to operate normally.

The control structure used is based on the standard sensorless architecture. During normal operation (motor running), the following actions are performed: The Clarke trans-

form converts the phase current measurements from a three-axis stationary reference frame (i_a, i_b and i_c) to a two-axis stationary reference frame (i_α and i_β). The current observer (rotor-position estimator) is implemented in the two-axis stationary reference frame ($\alpha\beta$-plane). The current observer uses the i_α, i_β, V_α and V_β measurements to estimate the rotor position. The Park transform converts the two-axis stationary reference frame current measurements (i_α and i_β) to the two-axis rotating reference frame (i_d and i_q). The control system is implemented in the dq-plane. The output voltage-command of the control system is converted from a two-axis rotating reference frame (V_d and V_q) to a two-axis stationary reference frame (V_α and V_β). From here the SVPWM conversion algorithm calculates the three-phase duty cycle values and sets the appropriate peripheral registers.

An online-parameter estimator is implemented to refine the open-loop parameter measurements and to keep the system parameters up to date. This online-parameter estimator is a non-intrusive observer that uses the current and voltage measurements in the dq-plane to estimate the machine parameters.

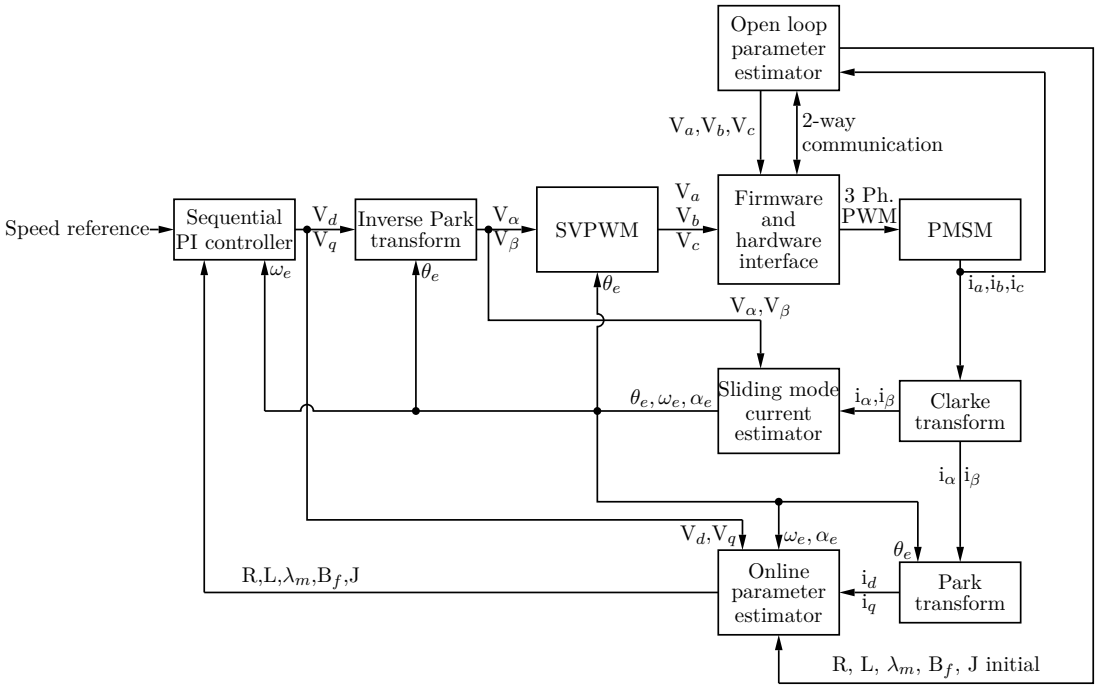

Figure 5.1: Block diagram of the entire embedded system

5.4 Literature study related to closed-loop system integration

5.4.1 Clarke transform

The Clarke transform is used to convert the three-phase current measurements of the machine from a three-axis stationary reference frame (i_a, i_b and i_c) to a two-axis two-phase orthogonal stationary reference frame (i_α and i_β) [33] [34]. Figure 5.2 shows the three-axis as well as the two-axis reference frames on the same graph.

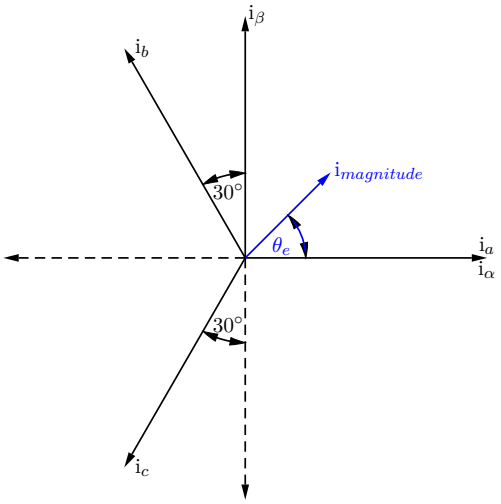

Figure 5.2: Clarke transform axis

From Figure 5.2 the axis conversion is performed by:

$$i_\alpha = i_a - i_b \sin 30° - i_c \sin 30° = \frac{3}{2} i_a \tag{5.1}$$

$$i_\beta = i_b \cos 30° - i_c \cos 30° = \frac{\sqrt{3}}{2}(i_b - i_c) \tag{5.2}$$

5.4.2 Park transform

The two-axis orthogonal stationary reference-frame current measurement (i_α and i_β) are converted to a two-axis rotating reference frame (i_d and i_q) with the Park transform [33]. Figure 5.3 shows the stationary reference-frame axis and the rotating reference-frame axis where θ_e is the electrical rotor angle. The direct component i_d is aligned with the rotor of the machine. The quadrature or torque component i_q is perpendicular to the direct component.

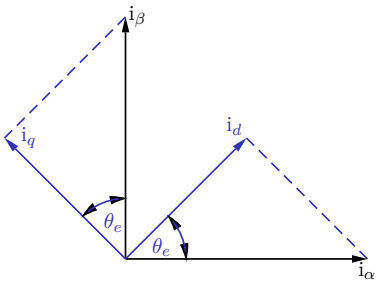

Figure 5.3: Park transform axis

The i_d and i_q components are calculated with:

$$i_d = i_\alpha \cos\theta_e - i_\beta \sin\theta_e \tag{5.3}$$

$$i_q = -i_\alpha \sin\theta_e - i_\beta \cos\theta_e \tag{5.4}$$

5.4.3 Inverse-Park transform

The output-voltage command of the control system is converted from a two-axis rotating reference frame (V_d and V_q) to a two-axis stationary reference frame (V_α and V_β) with the Inverse-Park transform [33]. Figure 5.4 shows the rotating reference frame as well as the stationary reference frame on the same axis.

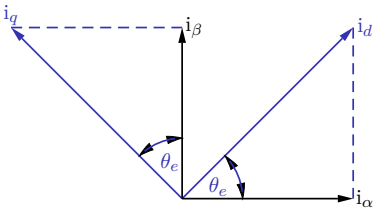

Figure 5.4: Inverse-Park transform axis

The V_α and V_β components are calculated with:

$$i_\alpha = i_d \cos\theta_e - i_q \sin\theta_e \tag{5.5}$$

$$i_\beta = -i_d \sin\theta_e + i_q \cos\theta_e \tag{5.6}$$

5.4.4 Decoupling

In field-oriented control the rotor-field component i_d and torque producing component i_q need to be controlled independently [35]. The electrical machine model in (5.7) and (5.8) clearly shows that the direct-voltage component (V_d) and quadrature-voltage component (V_q) are coupled [35].

$$V_d = Ri_d + L_d\frac{di_d}{dt} - \omega_e L_q i_q \tag{5.7}$$

$$V_q = Ri_q + L_q\frac{di_q}{dt} + \omega_e L_d i_d + \omega_e \lambda_m \tag{5.8}$$

The coupling term $\omega_e L_d i_d$ in the direct-voltage component equation is dependent on the rotor speed ω_e, quadrature-stator inductance L_d and the quadrature-current component i_q. Since the direct-current component i_d is forced to zero, only the coupled component $\omega_e L_q i_q$ in the direct-voltage equation needs to be considered.

5.4.5 Space vector pulse-width modulation

Space vector pulse-width modulation (SVPWM) is a voltage-control scheme that converts a voltage vector from a two-axis stationary reference frame to a three-axis stationary reference frame. Figure 5.5 shows a circuit diagram of the three-phase bridge connected to a PMSM [36].

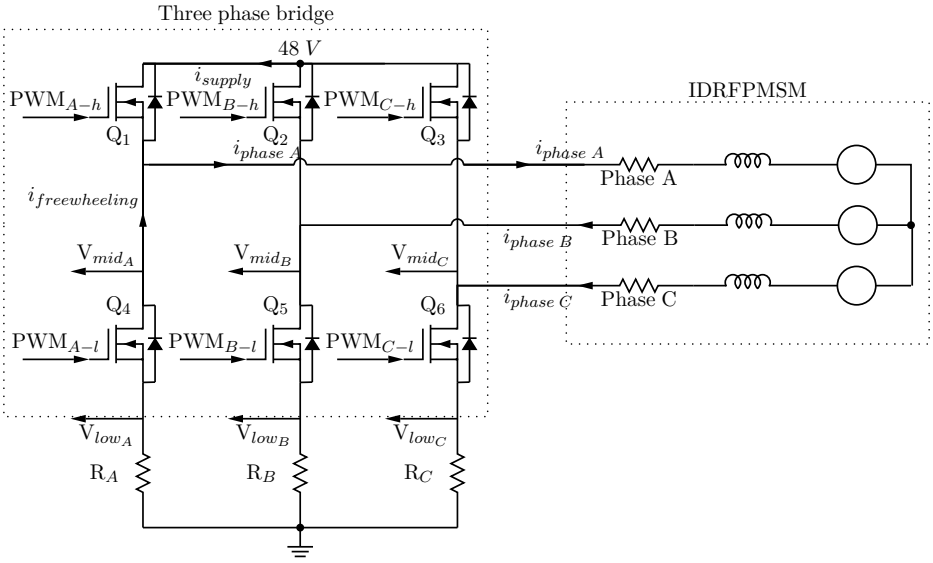

Figure 5.5: Three-phase MOSFET bridge connected to PMSM

Each of the three phases contains a high-side switch and a low-side switch. At any time in each phase one of the two switches is switch on while the other is switched off. There are eight possible switching combinations, as shown in Table 5.1 [36].

Table 5.1: Three-phase bridge switching combinations

State	Conducting MOSFET
000	Q_4,Q_5,Q_6
001	Q_4,Q_5,Q_3
010	Q_4,Q_2,Q_6
011	Q_4,Q_2,Q_3
100	Q_1,Q_5,Q_6
101	Q_1,Q_5,Q_3
110	Q_1,Q_2,Q_6
111	Q_1,Q_2,Q_3

Figure 5.6 shows the two sets of axes used in the conversion from the two-axis stationary reference frame ($\alpha\beta$-plane) to the three-axis stationary reference frame (abc-plane). Please note that in combination (111) with all the high-side switches on and in combination (000) with all the low-side switches on, the machine terminals are shorted together and no current is flowing from the power supply. These two states are known as "null" states and are used to control the voltage vector magnitude V_{ref}. The other six states divide the electrical rotation up into six 60° segments, as shown in Figure 5.6. The vector angle θ_e in a specific sector is controlled by the duty-cycle ratio of the two legs (states) adjacent to that sector [36].

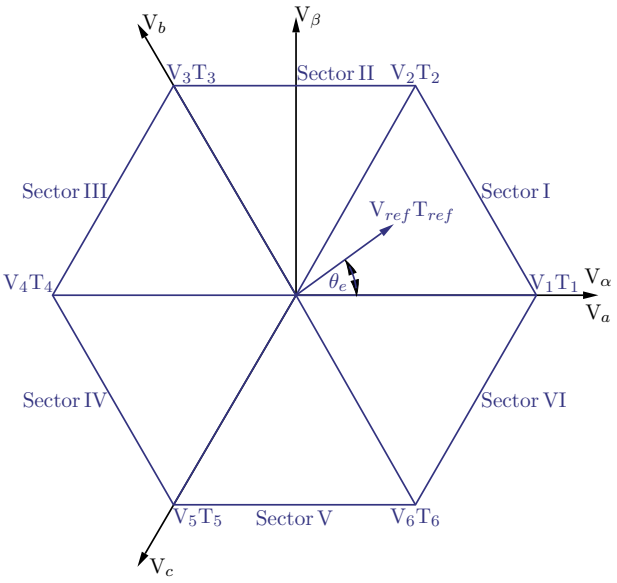

Figure 5.6: Two sets of axes used for PWM conversion

Sector I derivation

Figure 5.7 shows the two sets of axes used to do the PWM conversion in sector I.

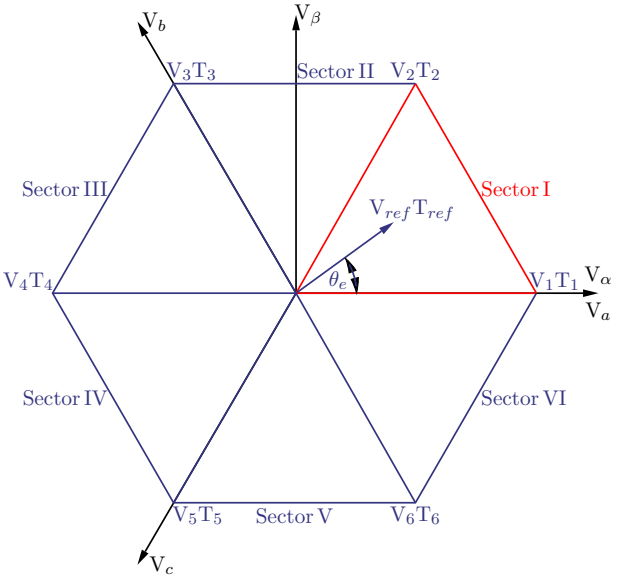

Figure 5.7: Two sets of axes used for PWM conversion with sector I

The voltage equation on the α-axis consists of:

$$V_1T_1 + V_2T_2\cos 60^\circ = V_{\text{ref}}T_{\text{ref}}\cos\theta_e \tag{5.9}$$

The voltage equation on the β-axis consists of:

$$V_2 T_2 \sin 60^\circ = V_{\text{ref}} T_{\text{ref}} \sin \theta_e \tag{5.10}$$

The relation between times T_1 and T_2 determines the angle θ_e. Times T_1 and T_2 are calculated from (5.9) and (5.10) as:

$$T_2 = \frac{2V_{\text{ref}} T_{\text{ref}} \sin \theta_e}{\sqrt{3} V_2} = T_P \frac{2V_{\text{ref}} \sin \theta_e}{\sqrt{3} V_{\text{power supply}}} \tag{5.11}$$

$$T_1 = \frac{V_{\text{ref}} T_{\text{ref}} \cos \theta_e - \frac{1}{2} V_2 T_2}{V_1} = \frac{2V_{\text{ref}} T_{\text{ref}}}{\sqrt{3} V_1} \left(\frac{\sqrt{3}}{2} \cos \theta_e - \frac{1}{2} \sin \theta_e \right) = \frac{2V_{\text{ref}} T_P}{\sqrt{3} V_{\text{power supply}}} \sin(60^\circ - \theta_e) \tag{5.12}$$

Time T_0 determines the magnitude of the voltage vector calculated with:

$$T_0 = T_P - T_1 - T_2 \tag{5.13}$$

where T_P is half of the PWM period as shown in Figure 5.8. Figure 5.8 shows the alignment of the PWM signals on the three machine phases. The PWM signals are aligned at the centre of the on-state as shown in Figure 5.8. The phase currents are measured at the centre of the PWM on-state where ringing is at a minimum.

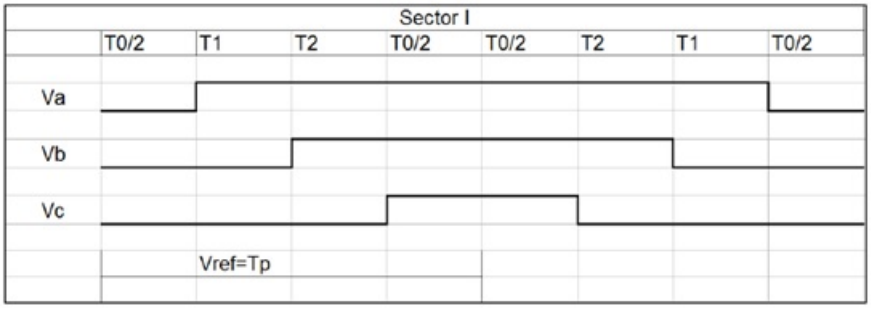

Figure 5.8: Three phase PWM waveform in sector I

With the graphs shown in Figure 5.8 the PWM duty-cycle at the three phases is calculated as:

$$D_A = \frac{T_1 + T_2 + \frac{T_0}{2}}{T_P} \tag{5.14}$$

$$D_B = \frac{T_2 + \frac{T_0}{2}}{T_P} \tag{5.15}$$

$$D_C = \frac{\frac{T_0}{2}}{T_P} \tag{5.16}$$

where D_A, D_B and D_C are the PWM duty-cycle of the three phases respectively. The derivation of the other five sectors is a repeat of the process presented in Sector I and are therefore not shown.

5.4.6 Sequential PI control system design

PI control system overview

Figure 5.9 shows a block diagram of the sequential PI controller, PMSM and the speed-measurement filter. The control system uses an inner current loop that controls the generated torque and an outside speed loop that controls the speed of the machine.

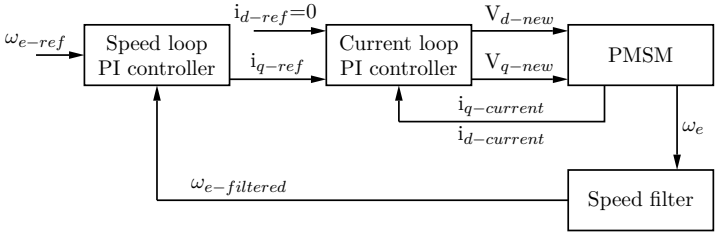

Figure 5.9: Sequential PI controller block diagram

Current-loop design

Figure 5.10 shows a block diagram of a PI controller. The K_P term represents the proportional gain and the K_I term represents the integral term [37].

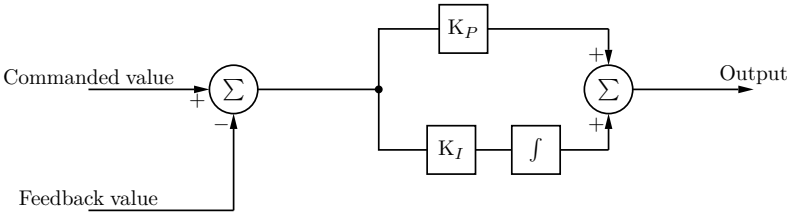

Figure 5.10: PI controller block diagram

Figure 5.11 shows the frequency response of a PI controller. As shown in Figure 5.11, the proportional gain term K_P specifies the higher frequency gain and the integral gain term

K_I specifies the low-frequency gain. A particular point of interest is the inflection point, as shown in Figure 5.11. The inflection-point position is determined by the location of controller zero [37]. The design goal is to cancel the machine pole in (5.20) with the controller zero in (5.19).

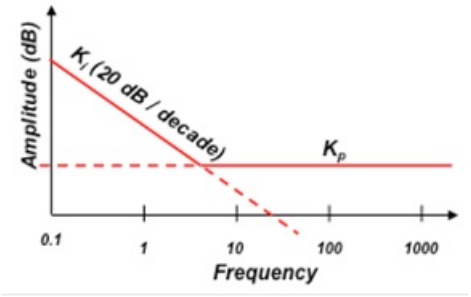

Figure 5.11: PI controller frequency response [37]

We will be working with the PI controller series topology as shown in Figure 5.12. Series gain term K_a sets the gain at all frequencies. Term K_b specifies the inflection-point (zero) location [37]. The relation between the series-topology gain terms (K_a and K_b) and the parallel-topology gain terms (K_P and K_I) are:

$$K_a = K_P \tag{5.17}$$

$$K_b = \frac{K_I}{K_P} \tag{5.18}$$

Figure 5.12 shows a block diagram of the current-loop PI controller and the PMSM electrical model.

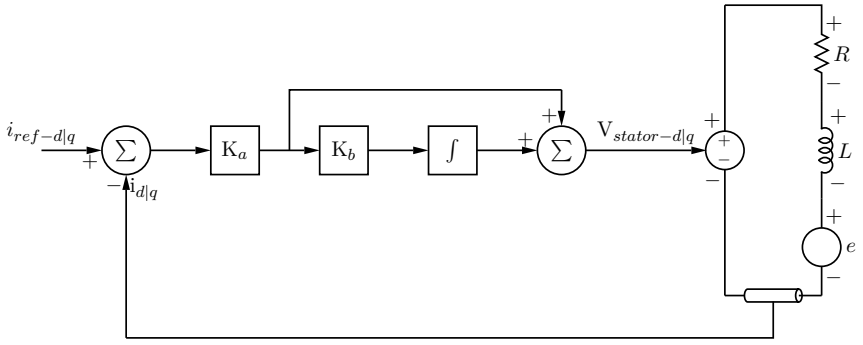

Figure 5.12: PI controller series topology and PMSM electrical model

The open-loop PI controller transfer function is described by:

$$PI(s) = \frac{K_I}{s} + K_P = \frac{K_a(K_b + s)}{s} \tag{5.19}$$

The electrical machine model voltage-to-current transfer function is described by:

$$\frac{I(s)}{V(s)} = \frac{\frac{1}{R}}{1 + \frac{L}{R}s} \tag{5.20}$$

The open-loop gain is described by:

$$G_{\text{open-loop}}(s) = PI(s) \cdot \frac{I(s)}{V(s)} = \frac{K_a(K_b + s)}{s} \cdot \frac{\frac{1}{R}}{1 + \frac{L}{R}s} \tag{5.21}$$

The closed-loop gain is calculated with (assuming unity feedback gain) [37]:

$$G_{\text{closed-loop}}(s) = \frac{G_{\text{open-loop}}(s)}{G_{\text{open-loop}}(s) + 1} = \frac{1 + \frac{s}{K_b}}{\frac{L}{K_a K_b}s^2 + \left(\frac{R}{K_a K_b} + \frac{1}{K_b}\right)s + 1} \tag{5.22}$$

The current-loop should have an over-damped response, the implication is that the closed-loop system should therefore have only real poles [37]. The denominator in equation (5.22) is factored out with real numbers A and B in:

$$\frac{L}{K_a K_b}s^2 + \left(\frac{R}{K_a K_b} + \frac{1}{K_b}\right)s + 1 = (As + 1)(Bs + 1) = ABs^2 + (A + B)s + 1 \tag{5.23}$$

The same powers of "s" are compared. In order to achieve real poles, the following two conditions should apply [37]:

$$\frac{L}{K_a K_b} = A \times B \tag{5.24}$$

and

$$\frac{R}{K_a K_b} + \frac{1}{K_b} = A + B \tag{5.25}$$

By simply equating the terms in (5.25) on both sides and by substituting A and B into (5.24), the inflection position (position of controller's zero) is calculated by:

$$K_b = \frac{R}{L} \tag{5.26}$$

By placing the zero of the controller on top of the motor pole the effect of the motor electrical pole is suppressed and the current loop will have a single-pole low-pass response. The closed-loop equation is simplified to:

$$G_{\text{closed-loop}}(s) = \frac{\left(1 + \frac{s}{K_b}\right)}{\left(1 + \frac{R}{K_a K_b}s\right)\left(1 + \frac{s}{K_b}\right)} = \frac{1}{\left(1 + \frac{R}{K_a K_b}s\right)} = \frac{1}{1 + \frac{L}{K_a}s} \tag{5.27}$$

Inspection of (5.27) shows that the current-loop bandwidth BW_{CL} can be set by choosing the controller gain K_a as [37]:

$$K_a = L \cdot BW_{CL} \tag{5.28}$$

The closed-loop equation can now be rewritten as:

$$G_{\text{closed-loop}}(s) = \frac{1}{1 + \frac{L}{K_a}s} = \frac{1}{1 + \frac{1}{BW_{CL}}s} = \frac{BW_{CL}}{BW_{CL} + s} \tag{5.29}$$

Speed-loop design

Figure 5.13 shows a diagram of the entire closed-loop system. The speed loop consists of the speed controller, current loop, velocity sensor, motor current-to-torque conversion and motor torque-to-rotor-speed conversion [37].

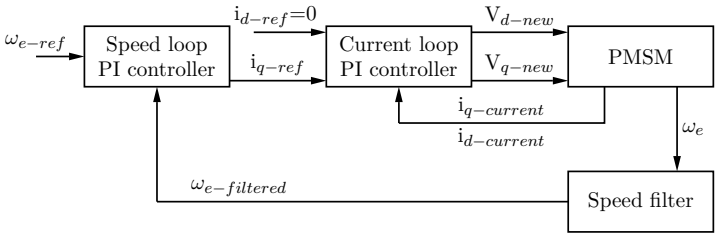

Figure 5.13: Speed-loop diagram

The rotor speed can be obtained from the discrete approximate differential of the rotor position $\omega_e \approx \frac{\delta\theta_e}{\delta t}$.

By increasing the sampling window size the measurement accuracy is increased but the low-pass filter bandwidth is reduced and visa versa. The low-pass filter transfer function with cut-off frequency ω_c is described by [37]:

$$G_{\text{Filter}}(s) = \frac{\omega_c}{s + \omega_c} \tag{5.30}$$

The current-loop transfer function is described by [37]:

$$G_{\text{Current-loop}}(s) = \frac{1}{\frac{L}{K_a}s + 1} \tag{5.31}$$

The transfer function between q-axis current and generated mechanical torque of a non-salient pole PMSM is described by [37]:

$$\frac{T_m(s)}{i_q(s)} = \frac{3}{2}P\lambda_m \tag{5.32}$$

where P is the number of pole pairs and λ_m is the rotor flux magnitude.

The transfer function between the generated mechanical torque and electrical rotor speed is described by [37]:

$$\frac{\omega_e(s)}{T_m(s)} = \frac{P}{Js + B_f} \tag{5.33}$$

where J is the moment-of-inertia and B_f is the friction coefficient of the system (system consisting of both machine and load).

Figure 5.14 shows a diagram of the complete speed loop.

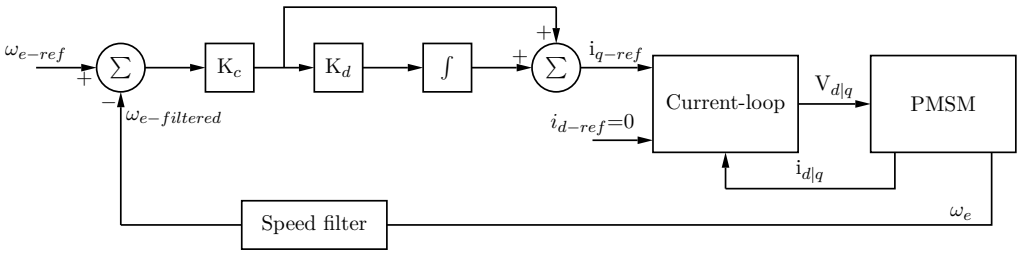

Figure 5.14: Speed-loop PI controller

The total open-loop transfer function of the speed loop consisting of the speed-controller, current-loop, speed-filter, current-to-torque transfer function and torque-to-rotor-speed transfer function is:

$$G_{\text{open-loop}} = \left(\frac{K_c(K_d + s)}{s}\right)\left(\frac{1}{\frac{L}{K_a}s + 1}\right)\left(\frac{3}{2}P\lambda_m\right)\left(\frac{P}{Js + B_f}\right)\left(\frac{\omega_c}{s + \omega_c}\right) \tag{5.34}$$

The derivation is simplified by assuming that the friction coefficient is negligible. The effect of the speed-filter pole will also be considered later in the derivation. The constant

terms are combined into the variable $K_K = \frac{3P^2\lambda_m}{2J}$. The open-loop transfer function is rewritten as:

$$G_{\text{open-loop}} = \frac{K_K K_c K_d \left(1 + \frac{s}{K_d}\right)}{s^2 \left(1 + \frac{L}{K_a} s\right)} \tag{5.35}$$

By inspection of (5.35) it is clear that there are two poles at $s = 0$ causing an attenuation rate of $40\,dB/decade$ at low frequencies. The current-loop pole is positioned at $s = \frac{K_a}{L}$. In order for stable operation the speed controller zero K_d should be placed at a lower frequency than the current-loop pole to establish an acceptable phase margin. Figure 5.15 shows a Bode plot of the open-loop system [37]. Please take note of the speed controller zero and the current-loop pole. The phase shift at the 0 dB frequency crossing determines the stability of the system. In order to achieve the maximum phase margin from the lead network, the 0dB frequency should occur at the geometric mean between the pole of the current loop and zero of the speed controller (halfway between the current-loop pole and the speed-controller zero on the logarithmic scale) [37]. This is arithmetically expressed by:

$$\omega_{0\,dB} = \zeta \times \omega_{\text{speed-loop zero}} \tag{5.36}$$

and

$$\omega_{\text{current-loop pole}} = \zeta \times \omega_{0\,dB} \tag{5.37}$$

where ζ is the damping factor. Equation (5.37) is substituted in (5.36) to deliver:

$$\omega_{\text{current-loop pole}} = \zeta^2 \times \omega_{\text{speed-loop zero}} \tag{5.38}$$

Since the current-loop pole is already defined, the speed-controller zero can be calculated with:

$$K_d = \frac{K_a}{\zeta^2 L} \tag{5.39}$$

If a speed filter is used, the speed filter pole would be much slower than the current-loop pole. The speed-controller would rather be designed with the speed filter pole than with the current-loop pole. Equation 5.39 is rewritten to a generic form in 5.40 where ω_{filter} is the speed filter cut-off frequency.

$$K_d = \frac{\omega_{\text{filter}}}{\zeta^2} \tag{5.40}$$

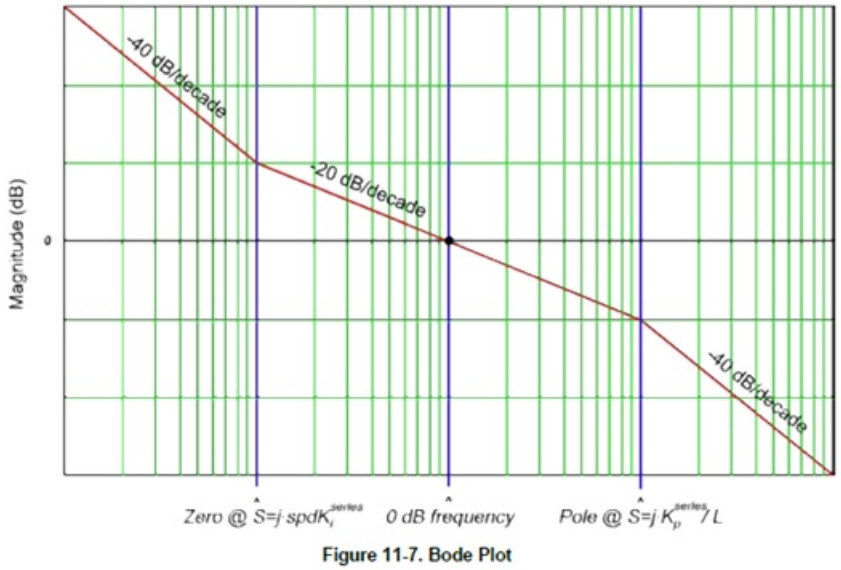

Figure 5.15: Bode plot of open-loop system [37]

The position of the speed controller zero determines both the speed-loop bandwidth and the speed-loop stability. The speed-controller zero is positioned by selecting an appropriate damping factor ζ. The choice of damping factor could either favour the speed-loop bandwidth or the speed-loop stability.

The magnitude at $\omega_{0\,dB}$ should be unity, therefore from (5.35):

$$\left| \frac{K_K K_c K_d \left(1 + \frac{s}{K_d}\right)}{s^2 \left(1 + \frac{L}{K_a} s\right)} \right|_{s=j\zeta K_d} = 1 \tag{5.41}$$

the appropriate substitution is made and (5.41) is rewritten as:

$$\frac{\zeta K_K K_c}{\zeta^2 \left(\frac{K_c}{\zeta^2 L}\right)} = 1 \tag{5.42}$$

Equation (5.42) is rewritten in terms of speed-loop gain term K_c:

$$K_c = \frac{\zeta K_d}{K_K} = \frac{\zeta K_d 2J}{3P^2 \lambda_m} \tag{5.43}$$

5.4.7 Motor current observer

There are many different types of sensorless rotor-position estimation methods used in the industry, as discussed in Chapter 1. The most popular of these are BEMF estimation methods. BEMF estimation methods are simple to implement but can only be used above 10 % of the rated speed of the machine where the generated BEMF voltage signal has a usable magnitude [5]. Forced commutation is regularly used to spin the rotor from standstill up to the minimum speed required by the sensorless position estimation method (generally 10 % of the rated speed)[38]. As the IDRFPMSM is an ironless non-salient pole machine, only BEMF position estimation techniques can be used for sensorless position estimation.

Motor current observers require only a phase-resistance parameter and a phase-inductance parameter to estimate rotor position. A sliding mode observer was implemented to estimate the phase current. The observer estimates first the generated BEMF voltage in the $\alpha\beta$-plane which in turn is then used to calculate the rotor position. The electrical machine equation is now used to calculate the estimated phase current from the estimated BEMF voltage. The estimated phase current is compared with the measured current and the difference is again used to correct the BEMF estimation error [39].

The electrical machine model equation used by the current observer is derived firstly. Figure 5.16 shows the electrical PMSM model where V_s, e_s and i_s are generic terms for the input voltage, BEMF voltage and stator current respectively. Terms R and L represents the phase resistance and phase inductance [39].

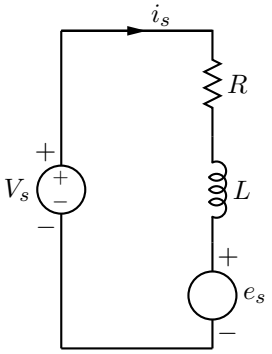

Figure 5.16: PMSM electrical model

The relationship between the input voltage V_s and stator current i_s is described by [39]:

$$V_s = Ri_s + L\frac{di_s}{dt} + e_s \tag{5.44}$$

The machine equation in (5.44) is rewritten as:

$$\frac{di_s}{dt} = -\frac{R}{L}i_s + \frac{1}{L}(V_s - e_s) \tag{5.45}$$

Equation (5.45) is converted to the digital domain into (5.46) with control period T_s [39]:

$$\frac{i_s(n+1) - i_s(n)}{T_s} = -\frac{R}{L}i_s(n) + \frac{1}{L}(V_s(n) - e_s(n)) \tag{5.46}$$

and rewritten in terms of $i_s(n+1)$ as:

$$i_s(n+1) = \left(1 - \frac{RT_s}{L}\right)i_s(n) + \frac{T_s}{L}(V_s(n) - e_s(n)) \tag{5.47}$$

Define gain parameters as $F = \left(1 - \frac{RT_s}{L}\right)$ and $G = \frac{T_s}{L}$. The electrical machine equation in (5.47) is rewritten as [39]:

$$i_s(n+1) = Fi_s(n) + G(V_s(n) - e_s(n)) \tag{5.48}$$

Figure 5.17 shows a block diagram of the current observer process. As explained earlier, the current observer is implemented in the $\alpha\beta$-plane. This process is therefore implemented for both the α-plane and the β-plane so the BEMF is calculated in both planes. The shaded block represents the PMSM. The equation in the machine model block describes the electric behaviour of the machine. The next state of the estimated stator current $i_{\text{s(estimate)}}$ is calculated with (5.48). The estimated stator current is now compared with the measured stator current. The current estimation error i_{error} is in turn used to correct the BEMF estimation error. If the current estimation error is within a predefined range, the correction factor Z operates in its linear range calculated by:

$$Z = \frac{K_{\text{slide}}i_{\text{error}}}{\text{SMC}_{\text{Max error}}} \tag{5.49}$$

where K_{slide} is the SMC gain, i_{error} is the estimated current error and $\text{SMC}_{\text{Max error}}$ is the maximum SMC error. If the current estimator error is outside a predefined range the

correction factor is clamped at $Z = K_{\text{slide}}$ to prevent unstable behaviour. The correction factor Z is in turn used to amend the estimated BEMF value e_{estimate}.

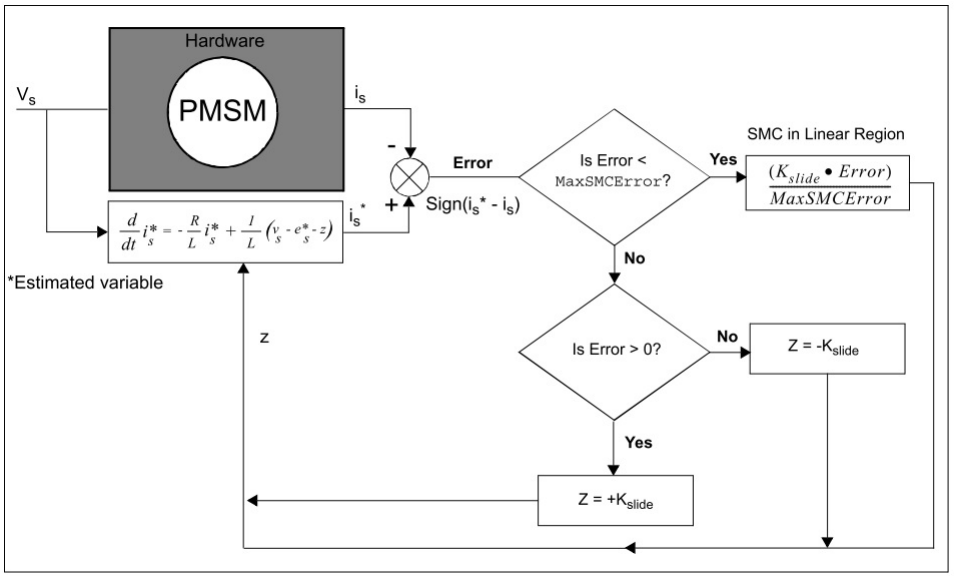

Figure 5.17: Current-observer block diagram [39]

Figure 19 illustrates the process of calculating the estimated BEMF e_s and rotor position θ_e from the correction factor Z. The estimated BEMF e_s is calculated by filtering the correction factor Z. The estimated BEMF in turn is filtered again and the rotor position θ_e is calculated from the α and the β components as described by:

$$\theta_{\text{estimate}} = \arctan \frac{e_{\alpha(\text{estimate})}}{e_{\beta(\text{estimate})}} \tag{5.50}$$

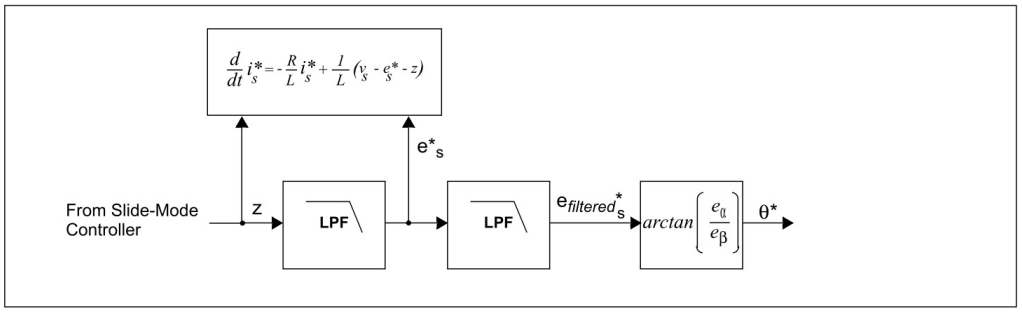

Figure 5.18: Process of calculating estimated BEMF and rotor angle from correction factor [39]

Figure 20 illustrates the relationship between the BEMF α-component e_α, the BEMF β-component e_β and the calculated rotor angle θ_e. As shown in Figure 20, a reliable rotor-angle estimation can be calculated from the BEMF components.

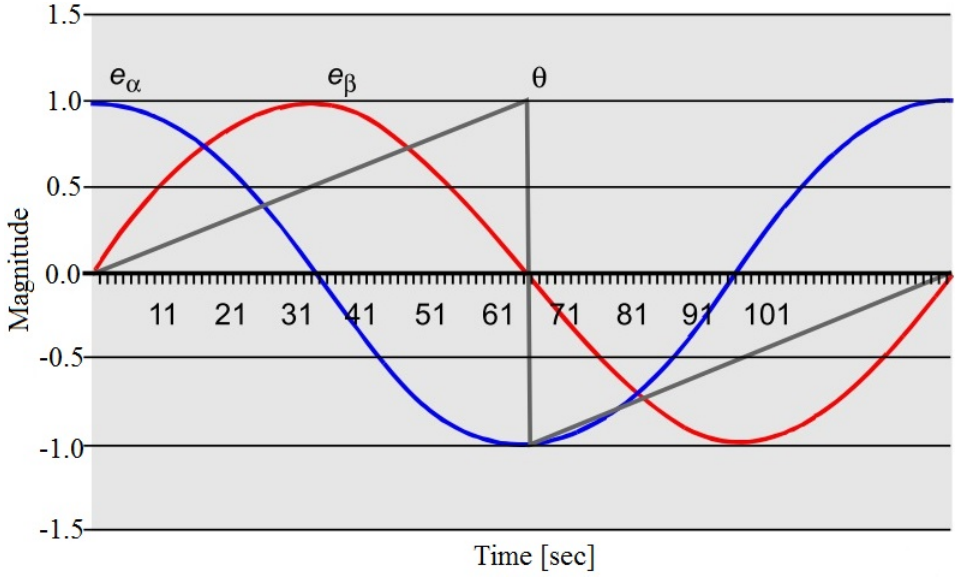

Figure 5.19: Relationship between BEMF components and rotor electrical angle [39]

Each low-pass filter causes a phase shift that is dependent on filter cut-off frequency and the signal frequency. Adaptive low-pass filters are used with the BEMF estimation and angle estimation. The adaptive filter cut-off frequency is changed to be the same as the phase-current frequency. This ensures that each adaptive filter causes a 45° phase shift. Equation (5.51) shows the adaptive filter used to calculate the estimated BEMF values $e_{estimate}(n)$ where f_c is the phase current frequency and f_{pwm} is the PWM switching frequency.

$$e_{\text{estimate}}(n) = \frac{1}{1 + \frac{2\pi f_c}{f_{pwm}}}\left(e_{\text{estimate}}(n-1) + \frac{2\pi f_c}{f_{pwm}} Z(n)\right) \tag{5.51}$$

The two adaptive low-pass filters produce a phase shift of 90°. This 90° phase shift can be compensated for in the rotor-position calculation.

5.4.8 Forced-spinning commutation

Estimators that use generated BEMF to determine rotor position require a BEMF signal of sufficient magnitude. This means that BEMF estimators cannot be used to determine

rotor position below 10 % of the rated speed [5]. Open-loop forced-spinning commutation is generally used to accelerate the rotor to a speed above 10 % of the rated speed. When the rotor speed is above the minimum speed required by the BEMF estimator, the closed-loop system takes over, using the estimated rotor position. Figure 5.20 shows a start-up sequence used with trapezoidal control [38]. Please take note of the purple phase-current graph. During the first two thirds of the current graph, the system uses open-loop forced-spinning commutation to speed-up the rotor. During the forced-commutation stage the rotor position is unknown. As shown in Figure 5.20, a much larger than needed phase current is used during forced commutation to ensure that the angle between the stator field and the rotor never exceeds 90° otherwise the system and the machine would loose synchronism. Once the minimum BEMF estimator speed is reached, the system transition-to-closed-loop control mode and the phase current is significantly reduced, as shown in the last third of the current graph in Figure 5.20 [38].

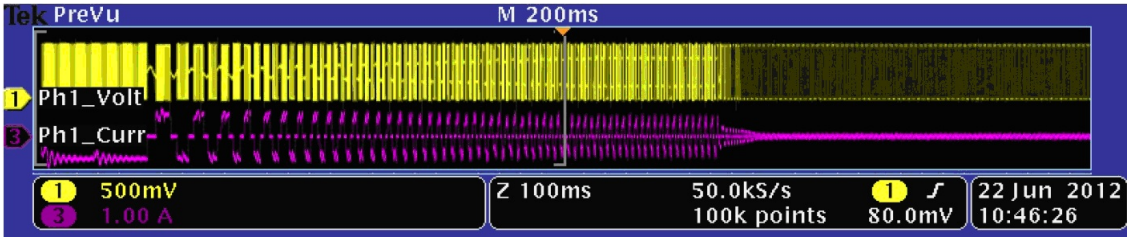

Figure 5.20: Trapezoidal-control start-up sequence with a trapezoidal controlled machine [38]

5.5 Embedded design

5.5.1 Embedded-system overview

Main loop

Figure 5.21 shows the main-loop flow diagram of the embedded system. At initial power-on all relevant system and peripheral registers are configured. The main loop then continues into an infinite loop that constantly poles external sensors for the latest angle information.

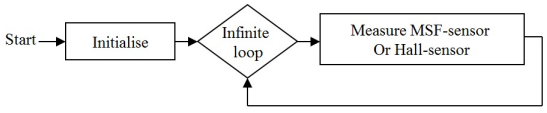

Figure 5.21: Main-loop flow diagram

System initialisation

Figure 22 shows the system initialisation flow diagram. The internal oscillator and phase-lock loop is configured to generate a system clock of 90 MHz. The relevant input and output pins are configured followed by three enhanced pulse-width modulation modules (PWM-module). The PWM-modules are configured to generate a 50 kHz signal giving it a 10-bit resolution. The phase-B and phase-C PWM signals are synchronised with the phase-A PWM signal. The 12-bit analogue-to-digital converter (ADC) is configured to trigger when it is in the centre of the phase-A PWM on-state. Once triggered ADC measurements are taken and the ADC service routine is called. Next the SPI module is configured followed by the enhanced-capture (E-Cap) module.

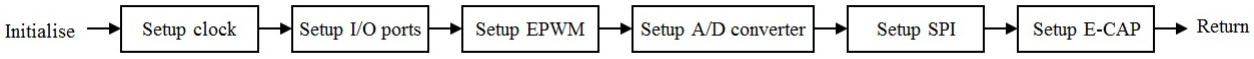

Figure 5.22: System initialisation flow diagram

ADC interrupt service routine

The ADC sampling and conversion process is triggered at the on-state centre of every third phase-A PWM signal. Once the ADC conversion completes, the ADC interrupt service routine is triggered. The entire embedded system functions within this ACD service routine. Figure 5.23 shows the ADC service routine flow diagram. When this service routine is called, the phase current, machine terminal voltage levels, bus voltage level and the speed reference level (user settable potentiometer) is calculated. The results are checked for overvoltage and overcurrent conditions. Should any occur, the system enters a trip state and the rotor freewheels to a standstill.

After microcontroller initialisation at initial power-on, the machine parameters are identified by the open-loop parameter estimation system presented in Chapter 3. The system therefore first enters the open-loop parameter estimation state (red) and once the machine is identified, continues with normal operation (blue).

As explained in Chapter 3: At the beginning of the open-loop parameter estimation state, the rotor is moved to a 0° electrical angle by applying a 0° electrical stator field for a predefined time period. This time period is long enough to allow the rotor to realign with 0° electrical and any oscillation to subside. Once oscillation has subsided a phase-resistance measurement is made. Now that the rotor is positioned at a known angle of 0° electrical, the stator field is quickly moved (jumped) to the 30° electrical angle

and the phase-A current is measured at specific locations during the oscillation. These measurements are used to calculate the BEMF-constant, friction-coefficient and moment-of-inertia of the machine, as explained in Chapter 3. Once the oscillation subsides, the charged (unknown) phase inductance is discharged through the (known) phase resistance and the time taken to discharge the inductor current to 33 % of its original value is used to calculate the inductance value. The system will now continue to normal operation (blue) till a trip condition is encountered.

During normal operation the phase current, terminal voltages, bus voltage and speed reference values are calculated and trip conditions are checked. Then the current observer algorithm is implemented to estimate rotor position. The closed-loop parameter estimation method presented in Chapter 3 is now used to refine and update the machine's parameter model. This ensures optimal control despite changing machine parameters. Next the Clarke transform converts the three-axis stationary reference-frame (abc) current measurements to two-axis stationary reference-frame ($\alpha\beta$) representation. The Park transform converts the two-axis stationary reference-frame ($\alpha\beta$) current measurements to two-axis rotating reference-frame (dq) components where the quadrature-component represents the usable torque generated by the machine. A control system is implemented in the dq-reference frame to set the required quadrature-voltage component and to zero the direct-voltage component thereby minimising driving losses. The output of the control system is converted from a two-axis rotating reference frame (dq) to a two-axis stationary reference frame ($\alpha\beta$) with the inverse-Park transform. The Space Vector PWM (SVPWM) algorithm calculates the duty-cycle values for the three PWM phases. The PWM control registers are then updated and the service routing is exited.

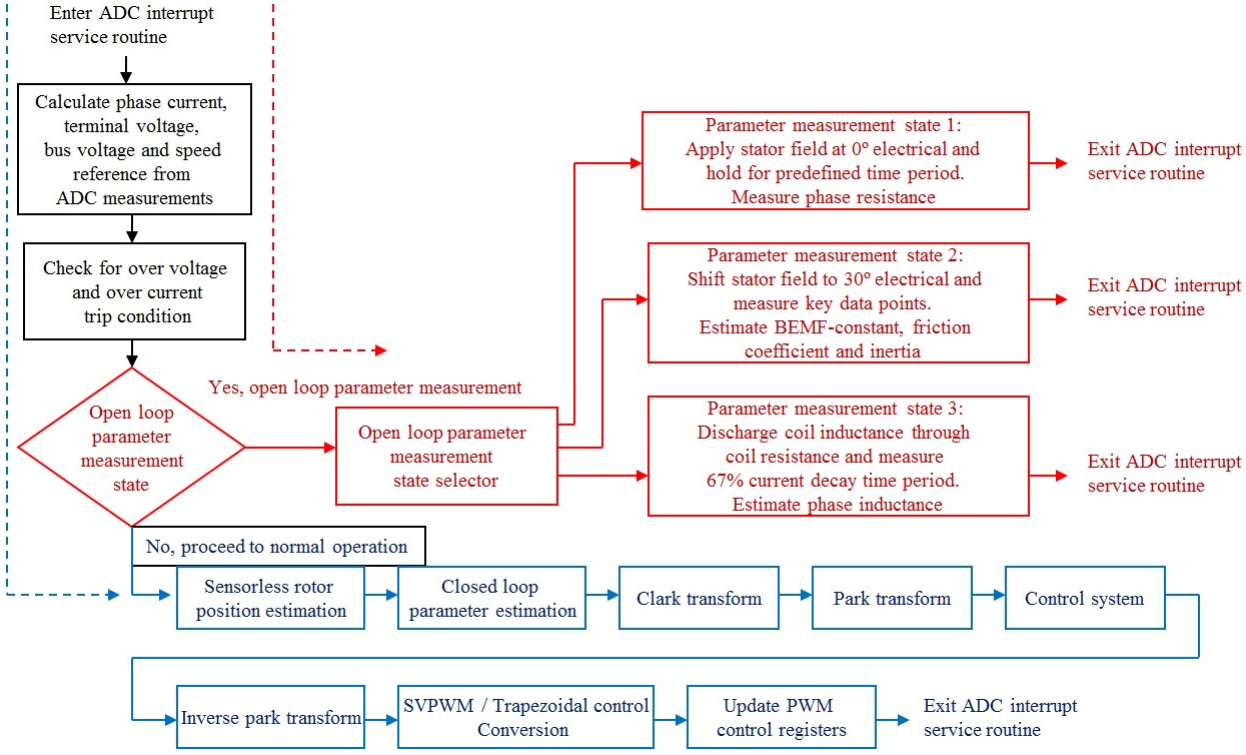

Figure 5.23: ADC service-routine flow diagram

5.5.2 Embedded-system components

As both the open-loop parameter estimation system and the closed-loop parameter estimation system have been discussed in depth in Chapter 3, it will not be covered in this chapter again. The Clarke transform, Park transform, Inverse-Park transform and SVPWM components are implemented exactly as explained in the literature section.

Sensorless rotor-position estimation

The MSF position sensor discussed in Chapter 2 was used as angle reference in the firmware development. This project focuses on sensorless control of permanent-magnet synchronous machines. A current observer is used to estimate the rotor position without a sensor.

Figure 5.24 shows the current-observer block diagram.

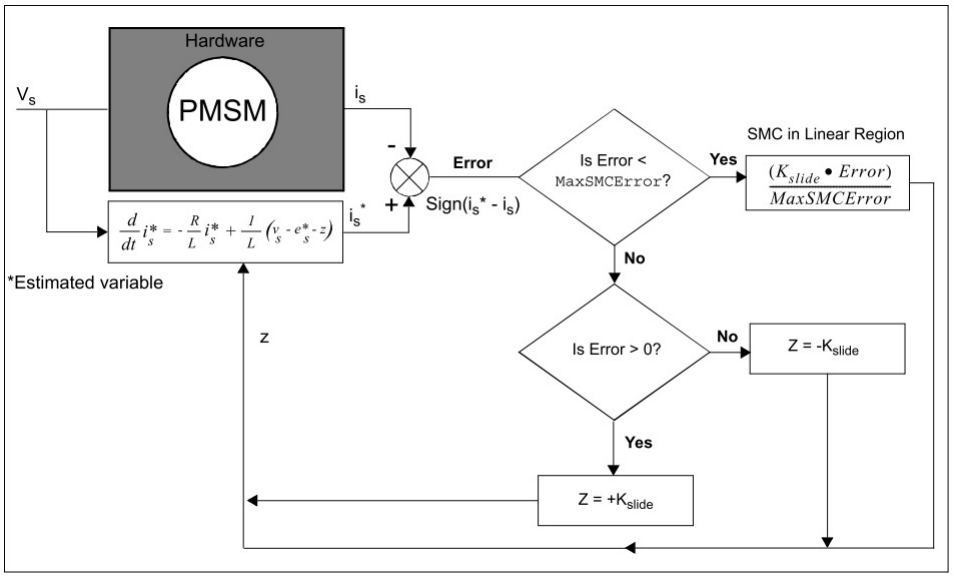

Figure 5.24: Current-observer block diagram [39]

The IDRFPMSM has a phase resistance of $0.2\,\Omega$ and a phase inductance of $147\,\mu$H. The control loop is called on every third cycle of the 50 kHz PWM gate signal, therefore $T_s = 60\,\mu sec$. Estimator-gain parameters F and G were calculated with:

$$F = 1 - \frac{RT_s}{L} = 0.0816 \tag{5.52}$$

$$F = \frac{T_s}{L} = 0.4082 \tag{5.53}$$

The electrical model of the IDRFPMSM was used to describe the machine equation:

$$i_s(n+1) = 0.0816 i_s(n) + 0.4082(V_s(n) - e_s(n)) \tag{5.54}$$

The adaptive filter equation used to calculate the estimated BEMF is described by:

$$e_{\text{estimate}}(n) = \frac{1}{1 + 0.00377 f_c}(e_{\text{estimate}}(n-1) + 0.00377 f_c Z(n)) \tag{5.55}$$

The SMC gain K_{slide} is described by:

$$K_{\text{slide}} = \frac{2\pi f_c}{f_{\text{pwm}}} = 2\pi f_c T_s = 0.00377 \tag{5.56}$$

Control-system design

As a first approach to control-system design, it could be assumed that the drive train consists of only the IDRFPMSM. The drive-train parameters are:

Table 5.2: IDRFPMSM parameters

Parameter	Symbol	Value
Phase resistance	R	$0.2\,\Omega$
Phase inductance	L	$143\,\mu$H
Rotor flux magnitude	λ_m	$0.0452\,\frac{V \cdot sec}{rad}$
Friction coefficient	B_f	$0.0395\,\frac{N \cdot m \cdot sec}{rad}$
Moment of inertia	J	$0.1396\,\frac{N \cdot m \cdot sec^2}{rad}$
Pole pairs	P	14
Rated speed		$300\,rpm$

Figure 5.25 shows a block diagram of the current-loop PI controller.

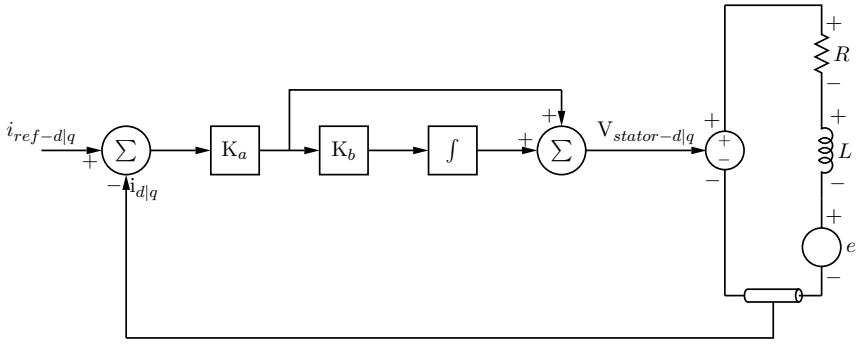

Figure 5.25: PI controller series topology and PMSM electrical model

The current-controller zero is placed on top of the electrical PMSM pole by calculating the inflection point with:

$$K_b = \frac{R}{L} = 1399 \tag{5.57}$$

The 14 pole pair IDRFPMSM has a rated mechanical speed of 300 rpm. The maximum phase-current frequency is calculated at 70 Hz or electric angular velocity of 440 rad/sec. A current-loop bandwidth three times higher than the maximum electrical angular velocity is chosen at 1257 rad/sec. The current-loop gain term is therefore calculated with:

$$K_a = L \cdot BW_C L = 0.1797 \tag{5.58}$$

The series PI controller parameters is converted to the parallel configuration with:

$$K_P = K_a = 0.1797 \tag{5.59}$$

$$K_I = K_P K_b = 251 \tag{5.60}$$

Let us choose a damping factor of $\zeta = 25$ which would favour system stability over bandwidth. The speed-loop zero is placed at:

$$K_d = \frac{\omega_{filter}}{\zeta^2} = 0.3016 \tag{5.61}$$

The speed-loop gain is calculated with:

$$K_c = \frac{\zeta K_d}{K_K} = \frac{2\zeta K_d J}{3P^2 \lambda_m} = 0.0792 \tag{5.62}$$

The series PI controller parameters are converted to the parallel configuration with:

$$K_{P-spd} = K_c = 0.0792 \tag{5.63}$$

and

$$K_{I-spd} = K_P K_d = 0.0239 \tag{5.64}$$

Analyse current-loop sensitivity to resistance mismatch

At a room temperature of 20 °C the IDRFPMSM has a stator-phase resistance of 0.2 Ω. However, the stator resistance changes with a change in coil temperature, as described by [40]:

$$R_{\text{new}} = R_{\text{room}}(1 + \alpha(T_{\text{new}} - T_{\text{room}})) \tag{5.65}$$

where R_{new} is the changed coil resistance, R_{room} is the coil resistance at room temperature, T_{new} is the changed coil temperature, T_{room} is room temperature and α is

the temperature coefficient of the copper coil (the temperature coefficient of copper is 0.004041) [40]. If the coil temperature rises or falls with 100 °C, the stator resistance will change with 81 mΩ. Figure 5.26 shows a step-response simulation with a current-loop designed for a machine with a 0.2 Ω coil resistance and 147 μH coil inductance. The blue curve in Figure 5.26 shows a current-loop step response with the machine at room temperature having a coil resistance of 0.2 Ω. The blue curve shows that the current-loop has a bandwidth of 200 Hz with the machine at room temperature. The red curve shows a current-loop step response with the machine coils 100 °C cooler than it was originally designed for. The lower coil resistance of 0.119 Ω causes the current loop to have an underdamped response with 6 % overshoot. The green curve shows a current-loop step response with the machine coils 100 °C warmer than originally designed for. The higher coil temperature will cause the current loop to have an even heavier damped response than at room temperature. This simulation shows that an extreme stator-coil temperature change of 100 °C will have little influence on the overall system performance. For this reason the online parameter estimator is not used to update the phase-resistance parameter.

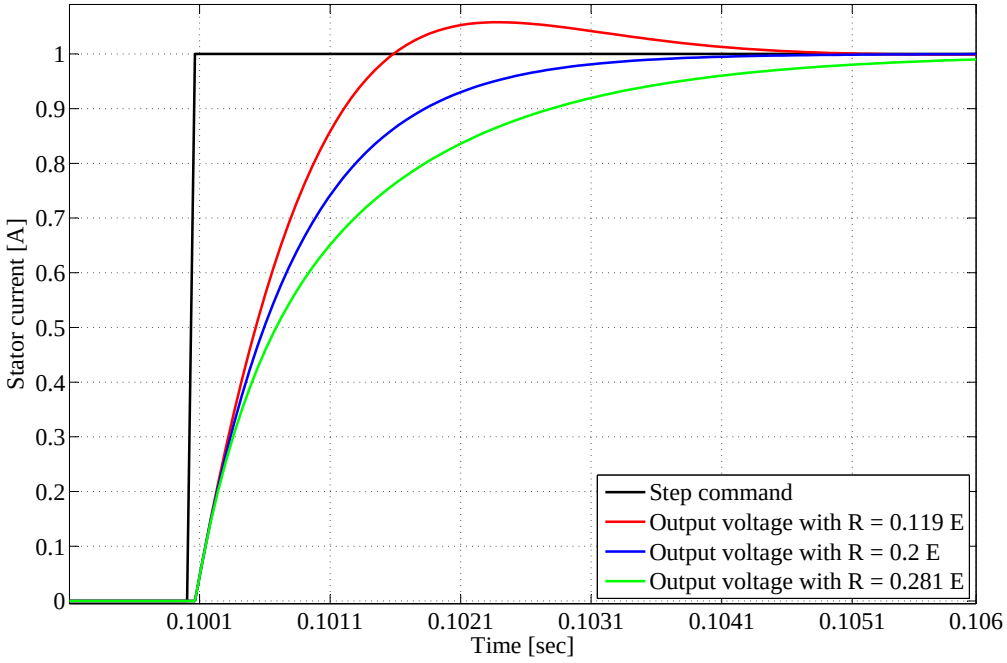

Figure 5.26: Current-loop step response with changing coil temperature (resistance)

Analyse speed-loop sensitivity to parameter mismatch

Figure 5.27 investigates the speed-loop sensitivity to mechanical parameter mismatch. The black curve shows the step response of the speed loop with the correct mechanical load. The blue curve and the magenta curve show that if the moment-of-inertia is doubled or the friction coefficient is halved, the speed-loop will have an under-damped response. The cyan curve and the red curve show that if the moment-of-inertia is halved or the friction coefficient is doubled, the speed-loop will have an over-damped response.

This simulation proves that the 50 % measurement error that can be expected with the open-loop parameter measurement technique will not cause speed-loop instability.

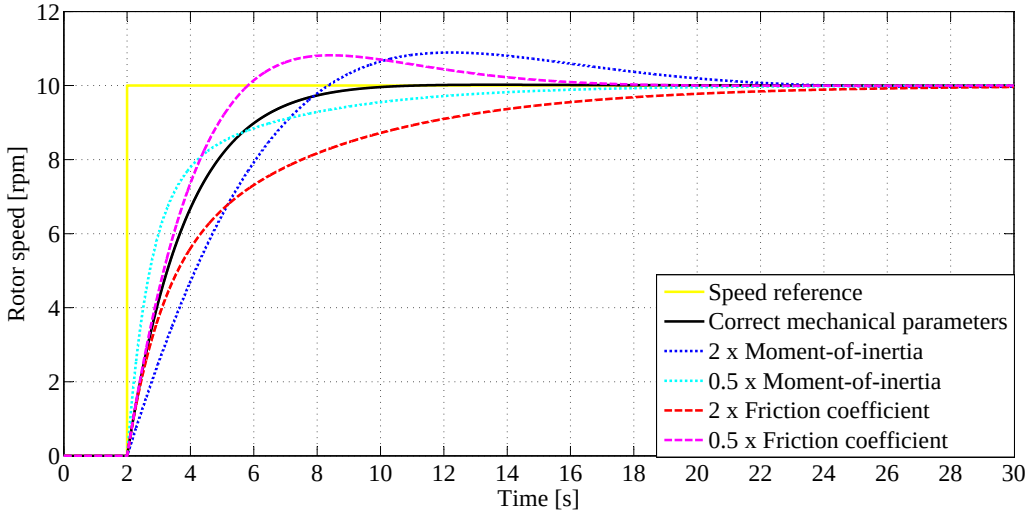

Figure 5.27: Simulation of speed-loop sensitivity to parameter mismatch

Start-up sequence with sensorless system

The minimum speed at which the BEMF estimator can make reliable rotor-position estimates depends on the ability of the system to distinguish between the BEMF signal and the noise. The second inverter developed for this project has exceptionally low noise levels and as a result the current observer implemented in this project delivers reliably rotor-position estimates at speeds below a thirtieth of the machine's rated speeds. Figure 5.28 shows a graphic representation of the regions of operation over the rotational speed range. The system transitions from open-loop operation to closed-loop operation when the rotor speed increases above 15 rpm. The system transitions back in open-loop operation when the rotor speed drops below 10 rpm. A transitioning hysteresis band is situated between 10 rpm and 15 rpm. It is worth mentioning that an inaccurate machine

model (due to coil heating) combined with high torque delivered (high stator current) could raise the minimum speed limit of the BEMF estimator.

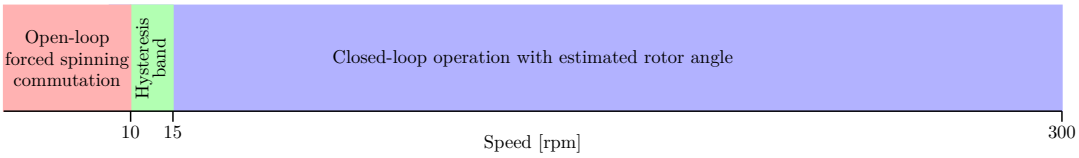

Figure 5.28: Regions of operation over rotational speed range

5.6 Integrated system closed-loop measured results

Figure 5.29 shows a picture of the inverter PCB connected to the IDRFPMSM. The speed reference is set with the speed-reference potentiometer, as shown in Figure 5.29.

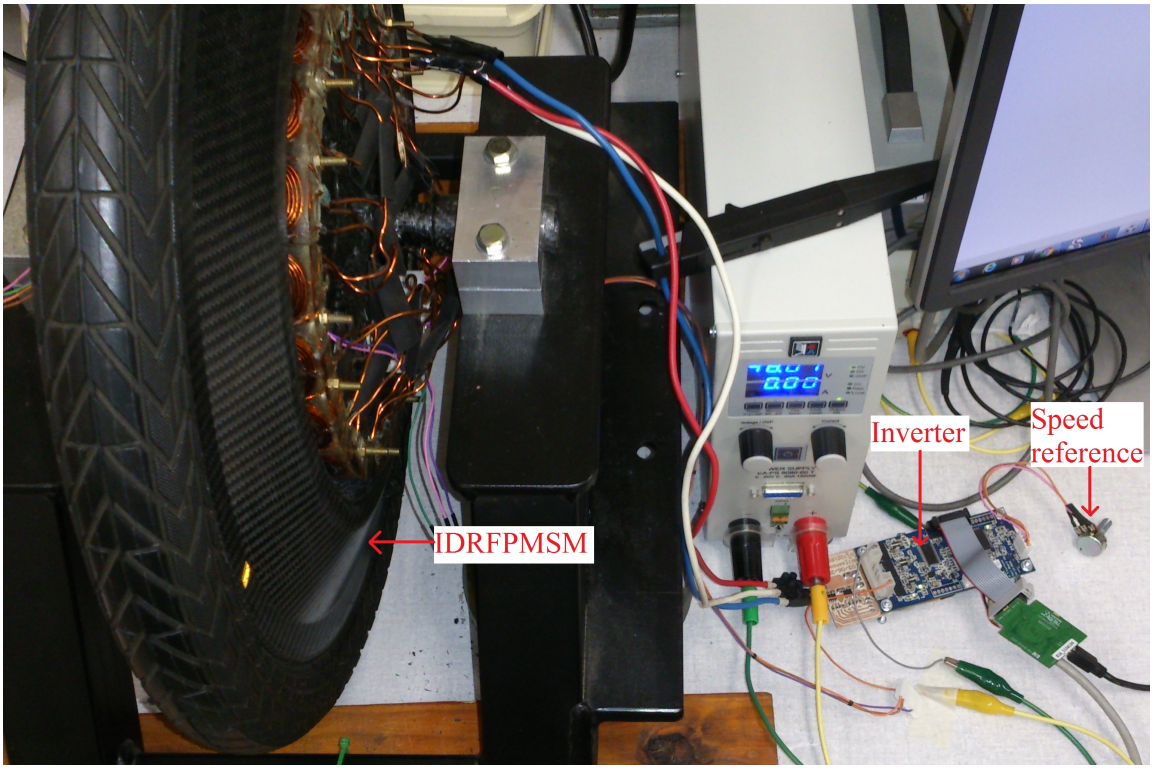

Figure 5.29: Picture showing inverter PCB connected to the IDRFPMSM

Figure 5.30 shows the measured phase-A current during the open-loop parameter identification procedure and the sensorless start-up sequence of the machine. The system is switched off during the first 1.5 seconds, as shown in Figure 5.30. Once the system is switched on, a 0° stator field is applied for 5 seconds, to allow the rotor to align with

the 0 ° stator field and any oscillation to subside. At the 6.5 seconds mark the phase resistance is measured and the stator field is shifted to the 30 ° electrical angle. The rotor now oscillates around the 30 ° electrical angle mark, creating the distinctive current pattern that is analysed to estimate the flux magnitude, friction coefficient and moment-of-inertia, as was introduced in Chapter 3. After the oscillation settled at 11.5 seconds, the phase inductance is measured with the inductor-discharge test and the system continues to operate normally.

At this point the rotor is at standstill and the system operates in open-loop mode. The user-defined speed reference is now increased and the rotor is accelerated with forced-spinning commutation. At 19 seconds in Figure 5.30 the rotor speed is above 15 rpm and the system transitions to closed-loop mode using the estimated rotor angle.

The system stays in closed-loop mode until the speed drops below 10 rpm where the system transitions to open-loop forced-spinning commutation again.

Please note the sizable difference of the current during open-loop forced-spinning commutation and closed-loop operation. The rotor position is unknown during forced-spinning commutation. A current magnitude far greater than what is needed in closed-loop operation is applied to ensure that synchronism is not lost. During closed-loop operation the rotor position is known, therefore the exact amount of quadrature-axis current can be applied to keep the machine spinning at the required speed.

Figure 5.31 shows a speed-loop step response test. During this test the rotor was originally rotating in closed-loop operation at 29.7 rpm. A step-response input was given and the rotor was accelerated to 66.8 rpm in 8 seconds. Then a deceleration test and another acceleration test were performed.

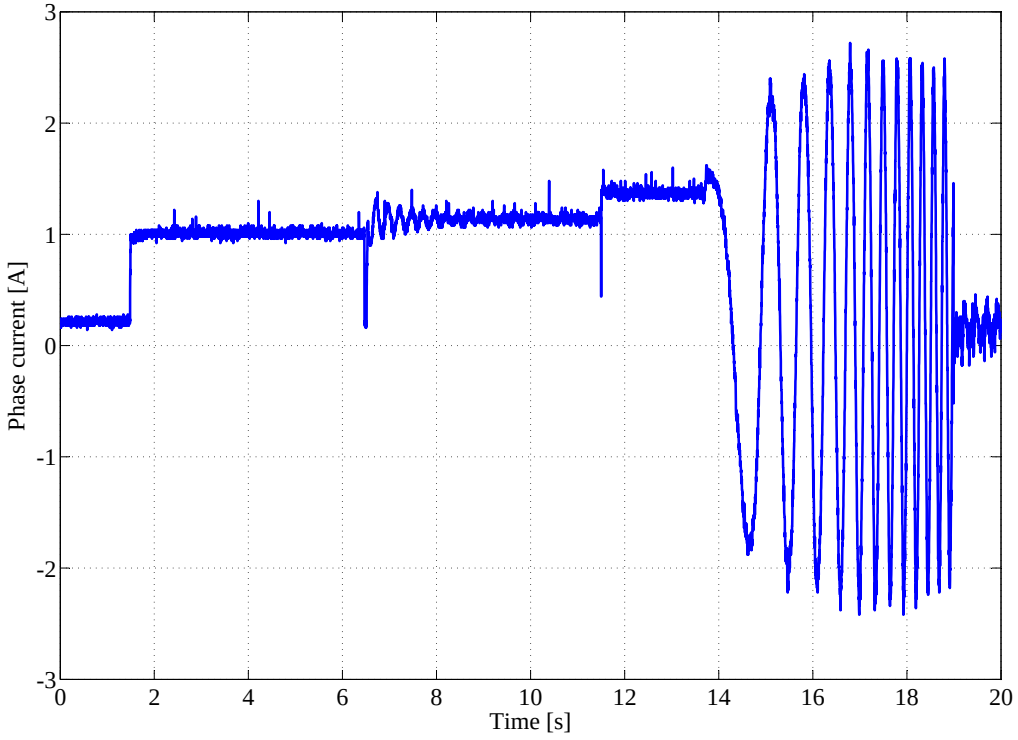

Figure 5.30: Phase-A current measurement during open-loop parameter identification and start-up sequence

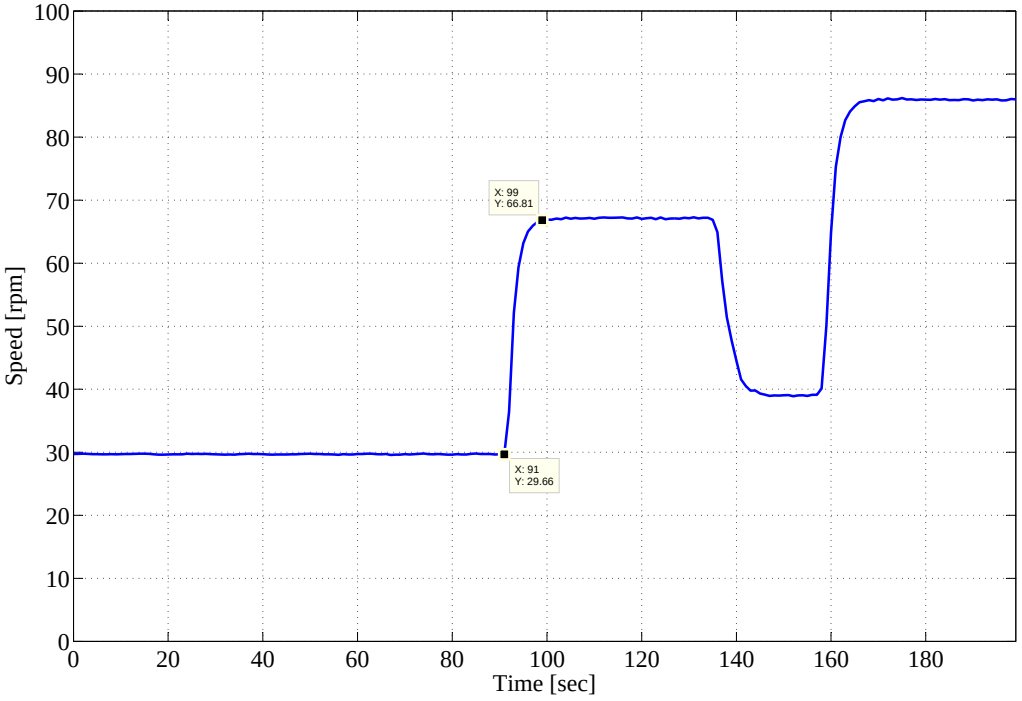

Figure 5.31: Speed-loop step-response test

Figure 5.32a shows the test-bench setup used during the energy-transfer step-response tests. This test-bench setup consists of an electric drill, IDRFPMSM, inverter PCB, PWM voltage clamp PCB, resistor bank and a power supply. The electric drill was used to drive the IDRFPMSM during the generator test. The electric drill was also used as mechanical load during the motor test. The power supply cannot sink any regenerated energy. A PWM voltage clamp was developed to dissipate the regenerated energy in the resistor bank.

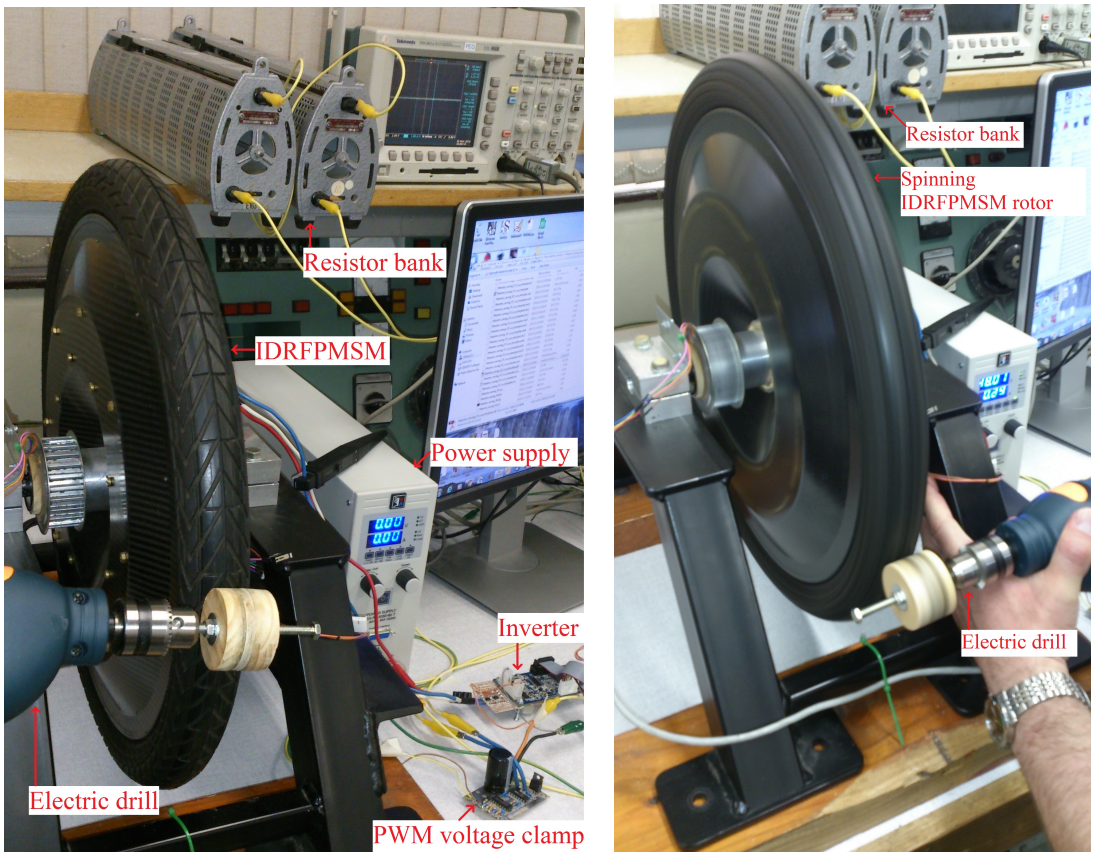

Figure 5.32: Test-bench setup for energy-transfer step-response tests

Figure 5.32b shows the IDRFPMSM-rotor spinning at 50 rpm during the energy-transfer step-response test while the IDRFPMSM is operating as a motor. The electric drill is used as mechanical load in this test.

Figure 5.33 shows the rotor speed, quadrature current and generated torque during the energy-transfer step-response test while the IDRFPMSM is operating as a motor. In this test the IDRFPMSM-rotor is spinning in steady state at 50 rpm. At the 30 second instant a mechanical loading (electric drill) was applied causing the speed to dip at 30 seconds. The control system quickly increases the developed torque causing the rotor

speed to increase and to settle at 50 rpm once again. When the load was removed at the 49 seconds instant there was a momentary rotor-speed overshoot and the control system adjusted the developed torque so that the rotor speed once again settled at 50 rpm.

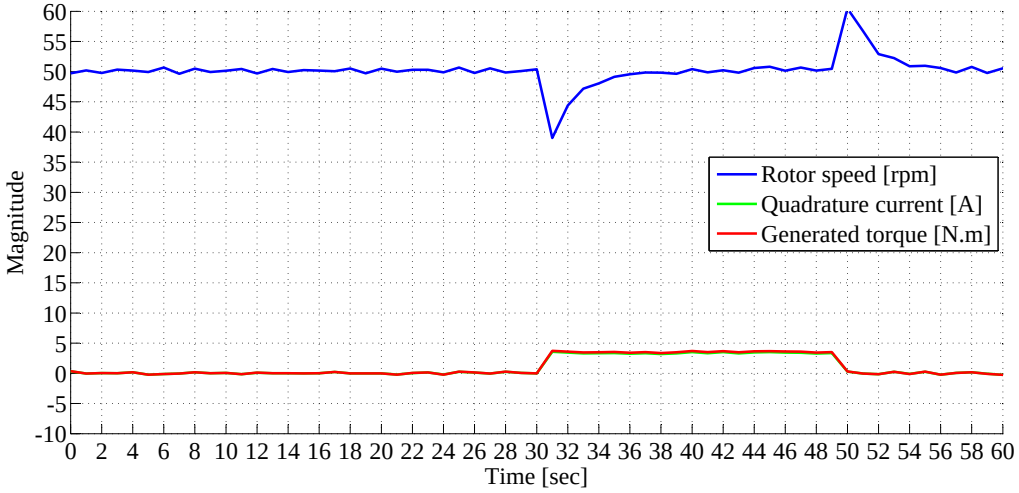

Figure 5.33: Speed-loop impulse-response during motor operation

Figure 5.34 shows the rotor speed, quadrature current and generated torque during the energy-transfer step-response test while the IDRFPMSM is operating as a generator. During the first 20 seconds the IDRFPMSM-rotor is spinning in steady state at 50 rpm. At the 20 second time instant the torque developed by the electric drill is increased causing a speed overshoot. The control system compensates by increasing the regenerative torque and the rotor speed settles at 50 rpm once again. At the 44 second mark the torque developed by the electric drill is reduced causing the speed to dip. The control system compensates by reducing the regenerative torque and the rotor speed settles at 50 rpm once again.

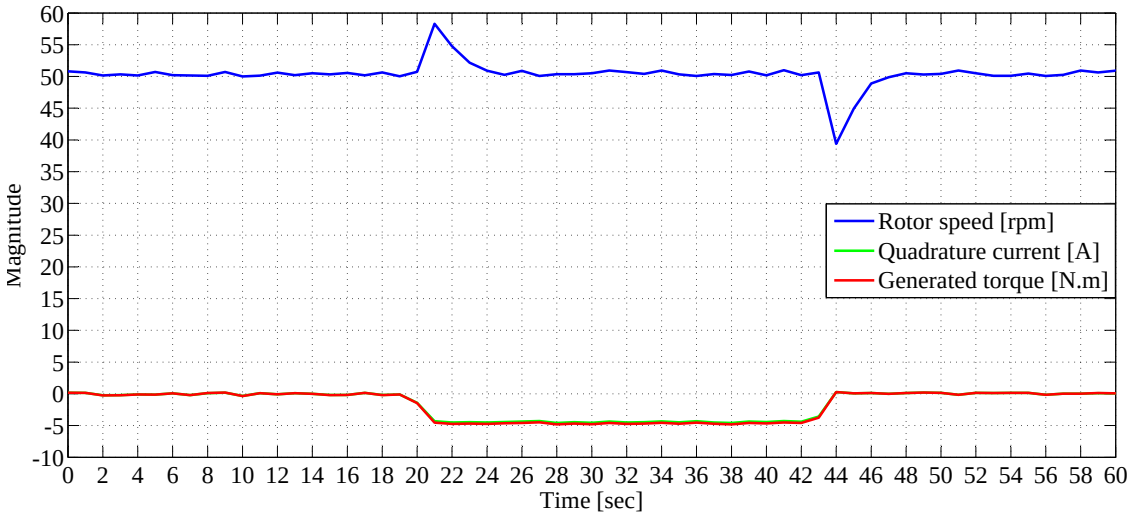

Figure 5.34: Speed-loop impulse-response during generator operation

Chapter 6

Conclusion

This study investigated sensorless control of a new type of ironless non-salient pole permanent-magnet synchronous machine (IDRFPMSM) for electric vehicle and wind-turbine generator applications. Different motor-control topologies and sensorless rotor-position estimation techniques were investigated. Due to the ironless non-salient pole nature of this machine and adding rotor position sensor elements are not an option, only BEMF rotor-position estimation techniques can be used. A current observer was used to implement the sensorless rotor-position estimation technique.

BEMF rotor-position estimation can only be used above a certain minimum speed. The current observer implemented in this project could reliably estimate rotor position at speeds as low as a thirtieth of the rated speed of the machine. This sensorless rotor-position estimation method is therefore ideal for wind-turbine generator applications.

Electric vehicle applications require torque from rotor standstill. As the current observer can only estimate rotor angle above a minimum speed, an alternative method was implemented in the low-speed range. The absence of rotor position sensors were overcome by using forced-spinning commutation to accelerate the rotor from standstill up to the minimum speed required by the current observer. In applications where efficiency at low speed is important but commercial position sensors cannot be used, a magnetic stray field position sensor is implemented.

Chapter 2 introduced a sensor that uses the magnetic stray fields behind the Halbach permanent-magnet array to calculate rotor position. By using a finite element magnetic field simulation technique, two distance regions behind the Halbach permanent-magnet array were identified with simulation. Measured results show the MSF-sensor provide a 10 ° electrical accuracy in the close-field region and a 15 ° electrical accuracy in the

far-field region. The rotor-angle measurement linearity synthesized from magnetic stray fields can be improved with the use of an estimator such as a Kalman filter.

The current observer requires accurate phase-resistance and phase-inductance parameters during rotor position estimation. The control system furthermore requires accurate phase-resistance, phase-inductance and moment-of-inertia parameters. All of these parameters need to be identified before closed-loop operation can be reliably attempted. Chapter 3 presents an open-loop parameter estimation technique that identifies all five machine parameters at system start-up during open-loop operation. Once the system is operating in closed loop, an online-parameter estimator will continue to monitor the mechanical parameters and update the system accordingly.

Two inverter versions were developed during this project. The first version of the inverter was to show proof of concept. With the development of the second version of the inverter the noise and ringing were reduced to such a level that a minimal ringing-overshoot of 6.1 % was measured with fast switching times of 25 nsec. The fast switching times and low MOSFET on-state resistance allowed for a maximum measured inverter efficiency of 98.77 %.

A sequential proportional-integral (PI) controller consisting of an inner current (torque) loop and an outer speed loop was implemented. The system was successfully tested in both motor and generator application. Reliable closed-loop sensorless control was recorded between 10 rpm and 300 rpm.

To demonstrate a strictly sensorless application, open-loop forced-spinning commutation is used to accelerate the rotor from standstill to 15 rpm where the system switches over to sensorless closed-loop operation. Should efficiency be important in the low-speed range, the MSF-sensor is used to measure the rotor angle below 15 rpm to allow for efficient closed-loop operation from standstill.

This study shows that the IDRFPMSM can be used for sensorless generator and motor applications.

List of References

[1] Miyamasu, M. and Akatsu, K.: Efficiency comparison between Brushless dc motor and Brushless AC motor considering driving method and machine design. pp. 1830–1835, nov 2011. ISSN 1553-572X. (Cited on pages 3 and 6.)

[2] Umans, S.D.: *Fitzgerald and Kinksleys Electric Machinery*. 2014. ISBN 9780071326469. (Cited on pages 3, 37, 50, and 54.)

[3] Kral, C., Gragger, J., Pirker, F. and Pascoli, G.: Sensorless rotor position estimation through current signature analysis based on rotor saliency harmonic. pp. 937–942, 2006. (Cited on pages 3 and 5.)

[4] Qiu, A. and Kojori, H.: Sensorless control of permanent magnet synchronous motor using extended Kalman filter. vol. 3, pp. 1557–1562, 2004. ISSN 0840-7789. (Cited on page 4.)

[5] Kim, T.-H. and Ehsani, M.: Sensorless Control of the BLDC Motors From Near-Zero to High Speeds. *IEEE Transactions on Power Electronics*, vol. 19, no. 6, pp. 1635–1645, nov 2004. ISSN 0885-8993. (Cited on pages 4, 104, and 108.)

[6] Darba, A., De Belie, F. and Melkebeek, J.A.: A Back-EMF Threshold Self-Sensing Method to Detect the Commutation Instants in BLDC Drives. *IEEE Transactions on Industrial Electronics*, vol. 62, no. 10, pp. 6064–6075, oct 2015. ISSN 0278-0046. (Cited on page 5.)

[7] Damodharan, P. and Vasudevan, K.: Sensorless Brushless DC Motor Drive Based on the Zero-Crossing Detection of Back Electromotive Force (EMF) From the Line Voltage Difference. *IEEE Transactions on Energy Conversion*, vol. 25, no. 3, pp. 661–668, sep 2010. ISSN 0885-8969. (Cited on page 5.)

[8] Mizutani, R., Takeshita, T. and Matsui, N.: Current model-based sensorless drives of salient-pole PMSM at low speed and standstill. *IEEE Transactions on Industry Applications*, vol. 34, no. 4, pp. 841–846, 1998. ISSN 00939994. (Cited on pages 5 and 6.)

[9] Scaglione, O., Markovic, M. and Perriard, Y.: First-Pulse Technique for Brushless DC Motor Standstill Position Detection Based on Iron B-H Hysteresis. *IEEE Transactions on Industrial Electronics*, vol. 59, no. 5, pp. 2319–2328, may 2012. ISSN 0278-0046. (Cited on page 6.)

[10] Jaganathan, B., Venkatesh, S., Bhardwaj, Y. and Prakash, C.A.: Kohonen's Self Organizing Map method of estimation of optimal parameters of a Permanent Magnet Synchronous Motor drive. In: *India International Conference on Power Electronics 2010 (IICPE2010)*, pp. 1–6. IEEE, jan 2011. ISBN 978-1-4244-7883-5. (Cited on pages 9, 35, and 89.)

[11] Kim, J.-U., Jung, S.-Y. and Nam, K.-H.: PMSM Angle Detection Based on the Edge Field Measurements by Hall Sensors. *Journal of Power Electronics*, vol. 10, no. 3, pp. 300–305, 2010. ISSN 1598-2092. (Cited on pages 9 and 20.)

[12] Sergeant, P., Hofman, I. and Van den Bossche, A.: Magnetic stray field based position detection in BLDC outer rotor permanent magnet synchronous machines. *International Journal of Numerical Modelling*, vol. 27, no. August 2013, pp. 544–554, 2013. ISSN 08943370. (Cited on pages 9 and 20.)

[13] Krishnan, R.: *Permanent Magnet Synchronous and Brushless DC Motor Drives*. 2010. ISBN 9780824753849. (Cited on pages 9, 10, 11, and 12.)

[14] Oosthuizen, G. and Randewijk, P.: Double-rotor ironless radial flux permanent magnet machine. In: *2014 International Conference on Electrical Machines (ICEM)*, pp. 496–501. IEEE, sep 2014. ISBN 978-1-4799-4389-0. (Cited on page 12.)

[15] Oosthuizen, G.I. and Randewijk, P.J.: Design of an Ironless Double-Rotor Radial Flux Permanent Magnet machine. In: *2015 IEEE International Electric Machines & Drives Conference (IEMDC)*, pp. 683–688. IEEE, may 2015. ISBN 978-1-4799-7941-7. (Cited on pages 12 and 13.)

[16] Liu, K. and Zhu, Z.Q.: Position Offset-Based Parameter Estimation for Permanent Magnet Synchronous Machines Under Variable Speed Control. *IEEE Transactions on Power Electronics*, vol. 30, no. 6, pp. 3438–3446, jun 2015. ISSN 0885-8993. (Cited on page 34.)

[17] Khov, M., Regnier, J. and Faucher, J.: On-line parameter estimation of PMSM in open loop and closed loop. In: *2009 IEEE International Conference on Industrial Technology*, pp. 1–6. IEEE, feb 2009. ISBN 978-1-4244-3506-7. (Cited on page 35.)

[18] Lee, S.-B.: Closed-Loop Estimation of Permanent Magnet Synchronous Motor Parameters by PI Controller Gain Tuning. *IEEE Transactions on Energy Conversion*, vol. 21, no. 4, pp. 863–870, dec 2006. ISSN 0885-8969. (Cited on page 35.)

[19] Makela, O., Repo, A.-K. and Arkkio, A.: Parameter estimation for synchronous machines using numerical pulse test within finite element analysis. In: *2008 18th International Conference on Electrical Machines*, pp. 1–5. IEEE, sep 2008. ISBN 978-1-4244-1735-3. (Cited on page 35.)

[20] Rashed, M., MacConnell, P.F.A., Stronach, A.F. and Acarnley, P.: Sensorless Indirect-Rotor-Field-Orientation Speed Control of a Permanent-Magnet Synchronous Motor With Stator-Resistance Estimation. *IEEE Transactions on Industrial Electronics*, vol. 54, no. 3, pp. 1664–1675, jun 2007. ISSN 1932-4529. (Cited on page 36.)

[21] Xi, X., Changming, C. and Meng, Z.: Dynamic Permanent Magnet Flux Estimation of Permanent Magnet Synchronous Machines. *IEEE Transactions on Applied Superconductivity*, vol. 20, no. 3, pp. 1085–1088, jun 2010. ISSN 1051-8223. (Cited on pages 36 and 42.)

[22] STMicroelectronics: MOSFET Device Effects on Phase Node Ringing in VRM Power Converters. *Application Note*, 2005.
Available at: `http://www.stmicroelectronics.com.cn/` (Cited on page 66.)

[23] STMicroelectronics: MOSFET Device Effects on Phase Node Ringing in VRM Power Converters. *Application Note*, 2005.
Available at: `http://www.stmicroelectronics.com.cn/` (Cited on page 67.)

[24] Instruments, T.: Ringing reduction techniques for nexfet. *Application Note*, 2011.
Available at: `http://www.ti.com/lit/an/slpa010/slpa010.pdf` (Cited on pages 68, 69, 70, 71, and 82.)

[25] Taylor, R. and Manack, R.: Controlling switch node ringing in synchronous buck converters. *Application Note*, 2012.
Available at: `http://www.ti.com/lit/an/slyt465/slyt465.pdf` (Cited on page 68.)

[26] Fairchild: Switch node ring control in synchronous buck regulators. *Application Note*, 2015.
Available at: `https://www.fairchildsemi.com/application-notes/AN/AN-4162.pdf` (Cited on pages 69 and 71.)

[27] Instruments, T.: Controlling switch-node ringing in synchronous buck converters. *Application Note*, 2012.
Available at: `http://www.ti.com/lit/an/slyt465/slyt465.pdf` (Cited on pages 70 and 71.)

[28] Williams, T.: *EMC for Product Designers*. 2007. ISBN 0750681705. (Cited on pages 72, 79, and 83.)

[29] Williams, T.: *EMC for Product Designers*. 2007. ISBN 0750681705. (Cited on page 72.)

[30] Kleim, R.: Choosing and Using Ferrite Beads. *Technical article*, 2015.
Available at: `http://www.allaboutcircuits.com/technical-articles/choosing-and-using-ferrite-beads/` (Cited on pages 73, 82, and 83.)

[31] Kleim, R.: Clean Power for Every IC, Part 3: Understanding Ferrite Beads. *Web article*, 2015.
Available at: `http://www.allaboutcircuits.com/technical-articles/clean-power-for-every-ic-part-3-understanding-ferrite-beads/` (Cited on page 73.)

[32] Joss, A. and Randewijk, P.: Design of an Ironless Double-Rotor Radial Flux Permanent Magnet Machine. In: *Southern African Universities Power Engeneering Conference - SAUPEC 2016*, pp. 1–6. SAIEE, Vereeniging, 2016. (Cited on page 79.)

[33] Texas Instruments: Clarke and Park Transforms on the TMS320C2xx on the TMS320C2xx. *Application Note*, 1997.
Available at: `http://www.ti.com/lit/an/bpra048/bpra048.pdf` (Cited on pages 91 and 92.)

[34] Microsemi: Park, Inverse Park and Clarke, Inverse Clarke Transformations MSS Software Implementation. *Application note*, 2013.
Available at: `http://www.microsemi.com/...` (Cited on page 91.)

[35] Freescale Semiconductor: Sensorless PMSM Vector Control with a Sliding Mode Observer for Compressors Using MC56F8013. *Application Note*, 2008.
Available at: `http://cache.freescale.com/files/microcontrollers/doc/ref_manual/DRM099.pdf` (Cited on page 93.)

[36] STMicroelectronics: Space vector modulation using 8-bit ST7MC microcontroller and ST7MC-KIT/BLDC starter kit. *Application Note*, 2007.
Available at: `http://www.st.com/.../en.CD00055518.pdf` (Cited on pages 93 and 94.)

[37] Texas Instruments: InstaSPI-FOC and InstaSPIN-MOTION. *Application Note*, 2014.
Available at: `http://www.ti.com/lit/ug/spruhj1f/spruhj1f.pdf` (Cited on pages 97, 98, 99, 100, 101, 102, and 103.)

[38] Torres D: Sensorless BLDC Control with Back-EMF Filtering Using a Majority Function. *Microchip Technology Inc. Application Note*, 2008.
Available at: `http://ww1.microchip.com/downloads/en/AppNotes/01160A.pdf` (Cited on pages 104 and 108.)

[39] Zambada, J: Sensorless Field Oriented Control (FOC) of a Permanent Magnet Synchronous Motor (PMSM). *Microchip Technology Inc. Application Note*, 2010.
Available at: `http://ww1.microchip.com/downloads/en/AppNotes/01078B.pdf` (Cited on pages 104, 105, 106, 107, and 112.)

[40] Serway R, B.R.: *Physics For Scientists and Engineers*. 2000. ISBN 0030226546. (Cited on pages 114 and 115.)